IChF
Institute of Physical Chemistry PAS

Ph.D. thesis prepared within the Warsaw-4-PhD School in Natural and Biomedical Sciences at the Institute of Physical Chemistry, Polish Academy of Sciences

ul. Kasprzaka 44/52, 01-224, Warsaw, Poland

Raman-integrated Microfluidic Device for Non-invasive Imaging of Leukaemic Cells

Author

Shreyas K. Vasantham

MTech

Supervisor

Prof. dr. hab. Piotr Garstecki

Auxiliary Supervisor

Dr Ladislav Derzsi

Warsaw, February 2024

Declaration

This thesis is composed of my original work and contains no material previously published or written by another person except where due reference has been made in the text. I have clearly stated the contribution by others to jointly authored works included in my thesis. The content within this doctoral thesis is not in violation of any copyright, Polish, or international law to the best of my knowledge.

This thesis is a result of the work I have carried out since the commencement of my higher degree by research candidature and does not include a substantial part of the work that has been submitted to qualify for the award of any other degree or diploma in any university or other tertiary institution.

I acknowledge that an electronic copy of my thesis must be lodged with the Institute of Physical Chemistry, Polish Academy of Sciences, and, subject to the policy and procedures of the Institute of Physical Chemistry, Polish Academy of Sciences, the thesis be made available for research and study in accordance with the copyright laws in Polish law unless a period of embargo has been approved by the Institute.

I acknowledge that the copyright(s) of all the material contained in my thesis reside(s) with the copyright holder(s) of that material. Where appropriate I have obtained copyright permission from the copyright holder(s) to reproduce material in this thesis and have sought the necessary permissions for it.

The copyright of this doctoral thesis rests with the author, and no information can be derived from it and may not be published without the author's prior written consent.

Signature: 

Date: 06/02/2024

Acknowledgement

Completing this thesis has been an extremely fulfilling experience. It sure came with a lot of challenges, triumphs, and bursts of self-discovery here and there. I am indebted to all the individuals who have played a role in my academic odyssey, their unwavering support and encouragement propelled me towards this milestone.

I extend my heartful gratitude to Prof. Piotr Garstecki and Dr Ladislav Derzsi, my supervisors, who believed in me and guided me throughout this endeavour. Piotr has been a beacon of wisdom and inspiration, conversations with him served as the bedrock of my growth as a researcher. Laci, thank you for always being supportive and giving me free rein in the labs to pursue all my ideas. I could not have risen to the challenge without your support and belief in my capabilities. I am grateful for all the time you both have dedicated these past years towards helping me transform ideas and aspirations into tangible reality.

I would like to acknowledge Dr Abhay Kotnala who has helped me see this PhD in a different light. His vision in research and his way of tackling challenges have been a great influence on my research practice. His ever-supportive attitude and expertise in optical tweezer systems have furthered my intrigue in this field. A special thanks to Dr Yurii Promovych for always being open to the ideas I have and helping me realise some of these rather tricky ones. He has been always available for any query I had dealing with electronics, software, and automation. I am thankful to Ms Justyna Gruszka and all the members of the MiCoF group who have helped me in their own way towards my research. I have been fortunate to receive all the support and assistance from them.

My support group in Poland, Sakshi Sareen, Debjita Mukherjee, Dr Abdul Qayyum, and Dr Francesco Nalin, have seen the highs and lows with me and got me going through all the difficult times. Thanks a lot for ensuring time inside and outside the lab was just as fun.

I would like to also thank my consortium partners from the Jagiellonian University in Krakow, whose labs I frequented for Raman measurements (National Science Centre, Poland (NCN) OPUS 15 no. 2018/29/B/ST4/00335). Thank you, Prof. Malgorzata Baranska, Dr Kasia Majzner, Ania, Ola and Krzystof for help with SRS measurements and the

energy they bring to research every time I visited them in Krakow. I hope to keep that energy going.

I must thank members of the Laser Center, Institute of Physical Chemistry, PAS for always welcoming me whenever I had troubles with laser diodes and optical fibers. Kasia, Marcin, and Yura, thank you for always indulging me and being available to answer any questions I had.

Many thanks to Dr Konrad Gizynski for the many discussions and help with COMSOL modelling. Thank you to Prof. Piotr Mrowka and Paulina Laskowska from the Institute of Haematology and Blood Transfusion, Warsaw, for providing me with cell samples to test with the microfluidic device.

My eternal gratitude to my parents, who have always stood by me and been a constant source of inspiration. I am thankful to all my friends for being there and supporting me to see this thesis through.

And finally, I must thank my partner, who has been instrumental in my success. Thank you for always lending an ear to all my worries and woes, and greeting me with the biggest smile after a long day of experiments. Her unwavering love and support have been the cornerstone of my strength throughout this gratifying phase of my life. Thank you for being my headache, Hag. I could not have seen this through without you. Thank you for being my place of sanity when all else failed.

Acknowledgement of Funding

I would like to thank the generous financial support of the Foundation for Polish Science (FNP) FNP TEAM-NET grant POIR.04.04.00-00-16ED/18-00 and the scholarship from the International Doctoral School, Warsaw4PhD. Their funding has enabled me to pursue my research interests, gain access to invaluable resources and collaborate with leading experts in this field. I am grateful for their belief in the potential of this work.

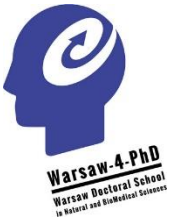

Research Involving Human or Animal Subjects

Parts of the thesis include experiments with human white blood cells. The experiments in chapters 3, 4 and 5 involve experiments as part of the Team-NET project (POIR.04.04.00-00-16ED/ 18-00) funded by the Foundation for Polish Science: "Label-free and rapid imaging, detection and sorting of leukemia cells".

The leukaemic cell lines were procured from the Institute of Haematology and Blood Transfusion, Warsaw, and the Medical University of Lodz in accordance with the consent of the Bioethics Committee at the Medical University of Łódź No. RNN/270/19/KE (extension KE/30/21) from May 2019.

List of Publications

This thesis comprises work from the following publications. The author contributions have been mentioned according to CRediT (Contributor Roles Taxonomy). For information on role descriptions please see credit.niso.org.

Publications and Conference Proceedings Related to the Topic of the Dissertation

1. Opto-hydrodynamic tweezers

   Shreyas Vasantham*, Abhay Kotnala*, Yurii Promovych, Piotr Garstecki, and Ladislav Derzsi

   *Equal contribution

   Lab on a Chip, 2024, 24, 517 – 527

   Conceptualisation: S. V., A. K.; Data Curation: S. V., A. K.; Formal Analysis: S. V., A. K.; Funding Acquisition: P. G.; Investigation: S. V., A. K.; Methodology: S. V., A. K., Y. P.; Project Administration: P. G., L. D.; Resources: P. G., L. D.; Software: S. V., A. K., Y. P.; Supervision: P. G., L. D.; Validation: S. V., A. K., Y. P., P. G., L. D.; Visualisation: S. V., A. K., Y. P., P. G., L. D.; Writing (original draft): S. V., A. K.; Writing (reviewing & editing): S. V., A. K., P. G., and L. D.

2. Spectroscopic flow-cytometry for leukocyte analysis: a proof-of-concept

   Shreyas Vasantham, Yurii Promovych, Krzystof Brzozowski, Aleksandra Borek-Dorosz, Malgorzata Baranska, Katarzyna Majzner, Anna Nowakowska, and Ladislav Derzsi

   Submitted to Lab on a Chip, 2024

   Conceptualisation: S. V., K. M., A. N.; Data Curation: S. V., A. B. D.; Formal Analysis: S. V., A. B. D., K. M., A. N.; Funding Acquisition: M. B., K. M., L. D.; Investigation: S. V., Y. P., A. B. D., K. B., A. N.; Methodology: S. V., Y. P., A. B. D, A. N.; Project Administration: M. B., K. M., L. D.; Resources: M. B., L. D.; Supervision: M. B., K. M., A. N., L. D.; Validation: S. V., Y. P., K. B., A. B. D., M. B., K. M., A. N., L. D.; Visualisation: S. V.,

A. B. D.; Writing (original draft): S. V., A. B. D., A. N.; Writing (reviewing & editing): S. V., Y. P., K. B., A. B. D., M. B., K. M., A. N., and L. D.

3. On-chip Opto-hydrodynamic Tweezers for Single cell manipulation

   Shreyas Vasantham, Piotr Garstecki, Ladislav Derzsi, and Abhay Kotnala

   Optical Manipulation and Its Applications, Ath1D. 5, Optica Publishing Group, 2023

   Conceptualisation: S. V., A. K.; Data Curation: S. V., A. K.; Formal Analysis: S. V., A. K.; Funding Acquisition: P. G.; Investigation: S. V., A. K.; Methodology: S. V., A. K.; Project Administration: P. G., L. D.; Resources: P. G., L. D.; Software: S. V., A. K.; Supervision: P. G., L. D.; Validation: S. V., A. K., P. G., L. D.; Visualisation: S. V., A. K., P. G., L. D.; Writing (original draft): S. V., A. K.; Writing (reviewing & editing): S. V., A. K., P. G., and L. D.

4. Opto-hydrodynamic fiber tweezers for stimulated raman imaging cytometry of leukemic cells

   Shreyas Vasantham, Piotr Garstecki, Ladislav Derzsi, and Abhay Kotnala

   Proceedings Volume 12649, Optical Trapping and Optical Micromanipulation XX; 126490Q, 2023

   Conceptualisation: S. V., A. K.; Data Curation: S. V., A. K.; Formal Analysis: S. V., A. K.; Funding Acquisition: P. G.; Investigation: S. V., A. K.; Methodology: S. V., A. K.; Project Administration: P. G., L. D.; Resources: P. G., L. D.; Software: S. V., A. K.; Supervision: P. G., L. D.; Validation: S. V., A. K., P. G., L. D.; Visualisation: S. V., A. K., P. G., L. D.; Writing (original draft): S. V., A. K.; Writing (reviewing & editing): S. V., A. K., P. G., and L. D.

Other Publications

1. Physicochemical Properties Predict Retention of Antibiotics in Water-in-Oil Droplets

   Artur Ruszczak, Pawel Jankowski, **Shreyas Vasantham**, Ott Scheler and Piotr Garstecki

   Analytical Chemistry, 2023, 95, 2, 1574–1581

2. Influence of bacterial strain type and TEM-1 enzyme allele on heteroresistance in monoclonal populations, independent of TEM-1's catalytic activity

   Shahab Shahryari, Shakeel Ahmad, Ilona Paulina Foik, Paweł Jankowski, Adam Samborski, Marcin Równicki, **Shreyas Kandhadai Vasantham**, and Piotr Garstecki

   Submitted to Scientific Reports, 2024

3. Speckle imaging offers sensitive detection of bacterial growth in microdroplet antibiotic susceptibility testing assays

   Shreyas Vasantham, Shakeel Ahmad, Piotr Garstecki and Abhay Kotnala

   Proc. SPIE 12374, Microfluidics, BioMEMS, and Medical Microsystems XXI, 1237407, 2023

4. Paper based point of care immunosensor for the impedimetric detection of cardiac troponin I biomarker.

   Shreyas Vasantham, Ruby Alhans, Chaitali Singhal, Shalini Nagabooshanam, Sumaya Nissar, Tinku Basu, Sekhar C. Ray, Shikha Wadhwa, Jagriti Narang and Ashish Mathur

   Biomed Microdevices 2020, 22, 6

Patent

1. Układ mikroprzepływowy z zintegrowanym światłowodem jednomodowym, P.445376 [WIPO ST 10/C PL445376]
   Submitted on 28.06.2023
   Creators: Shreyas K. Vasantham, Abhay Kotnala, Yurii Promovych, and Ladislav Derzsi.

Conferences

1. "Speckle imaging offers sensitive detection of bacterial growth in microdroplet antibiotic susceptibility testing assays", **Oral presentation**, SPIE Photonics West 2023, San Francisco, USA.

2. “Opto-hydrodynamic fiber tweezers for stimulated raman imaging cytometry of leukemic cells”, **Poster presentation**, SPIE Optics + Photonics 2023, San Diego, USA.

3. “On-chip Opto-hydrodynamic Tweezers for Single Cell Manipulation”, **Oral presentation**, Optica Biophotonics Congress: Optics in the Life Sciences 2023, Vancouver, Canada. [awarded the Optica Student Paper Award]

4. “Opto-hydrodynamic tweezers for single-cell manipulation and analysis”, **Poster presentation**, MicroTAS 2023, Katowice, Poland.

5. “Fiber-based, on-chip, opto-hydrodynamic tweezers for single-cell manipulation”, **Poster presentation + Flash talk**, NanoBioTech 2022, Montreux, Switzerland.

Table of Contents

List of Symbols, Acronyms, Notations, and Abbreviations

Symbol/Abbreviation	Description
μ	micro
μPAD	micro–paper analytical devices
μTAS	micro total analysis system
BSA	bovine serum albumin
CBC	complete blood count
cP	centipoise (unit of viscosity; 1cP = 1 mPa.s)
CSCs	cancer stem cells
CT	computed tomography
CTCs	circulating tumour cells
DEP	dielectrophoresis
DNA	deoxyribonucleic acid
E_o	energy level in the ground state
FACS	fluorescence-activated cell sorting
FBS	foetal bovine serum
GLMT	Generalized Lorenz-Mie Theory
GP	General practitioner
h	Planck constant (6.626×10^{-34} J.s)
ICs	integrated circuits
k_B	Boltzmann constant (1.38×10^{-23} J/K)
KMCA	k-means cluster analysis
MACS	magnetic cell sorting
MFD	mode field diameter
mM	milli molar
MRI	magnetic resonance imaging
NA	numerical aperture
NIR-LRT	near infrared laser Raman trapping
OA	oleic acid
OHT	opto-hydrodynamic tweezers
p	momentum
PA	palmitic acid
PBMC	peripheral blood mononuclear cells
PBS	phosphate buffer saline
PDMS	polydimethylsiloxane
P_e	Peclet number
PM	polarisation maintaining
PS	polystyrene
RBC	red blood cells

R_e	Reynold's number
R_h	hydraulic resistance
RNA	ribonucleic acid
RPM	Revolutions per minute
ROCS	rotating coherent scattering
RoI	region of interest
RS	Raman spectroscopy
scRNA seq	single-cell RNA sequencing
SMF	single mode fiber
SNR	signal-to-noise ratio
SRS	stimulated Raman scattering
T	absolute temperature
UV	ultraviolet
WBC	white blood cells
λ	wavelength
$\lambda_{\_em}$	emission wavelength
$\lambda_{\_exc}$	excitation wavelength
ρ	density

List of Figures

List Of Tables

Warsaw, February 07, 2024

Title of the doctoral dissertation

Raman-integrated Microfluidic Device for Rapid Non-invasive Imaging of Leukaemic Cells

Author: **Shreyas Kandhadai Vasantham, MTech**

Supervisor: **Prof. hab. Piotr Garstecki**

Auxiliary supervisor: **Dr Ladislav Derzsi**

Microfluidics and Complex Fluids Lab, Institute of Physical Chemistry, Polish Academy of Sciences, Kasprzaka 44/52, Warsaw 01-224, Poland

Abstract

Optical tweezers have been studied for over four decades to trap and manipulate particles using light, advancing research in single-particle technologies. We have developed, studied, and experimentally demonstrated a novel on-chip tweezer platform combining fiberized lasers and microfluidics. The tweezing is actuated by the balance of the optical and hydrodynamic forces acting on the particle. Furthermore, the use of one diverging laser through a single-mode optical fiber reduces stress due to light exposure on the trapped particle compared to other tweezing approaches that either employ a focussed beam or involve multiple lasers to trap particles.

With our opto-hydrodynamic tweezer (OHT), we were able to perform various operations such as translation, rotation, and isolation, on trapped particles and cells. OHT offers control over the flow trajectories owing to the implementation of 3D hydrodynamic focusing. The trapped particle could be translated over a long distance of up to 500 μm along the length of the microchannel. This allows the integration of other optical detection modalities with the chip further improving its functionality. A Stimulated Raman microscope was integrated with the microfluidic device to image trapped leukaemic cells. It offers a label-free approach to investigating and understanding the composition of proteins, nucleic acids, lipids, etc., at different wavenumbers within a few seconds.

The unparalleled synergy between microfluidics, optical tweezers and Raman microscopy is a promising step towards transforming personalised medicine approaches.

The primary obstacle in our manipulation approach lies in the stability of the trap applied to various particles, thus limiting applications. Essentially, this is contingent on the stiffness of the trap which is controlled via the output laser power of the fiber and the fluctuations in the flow field. At high flow rates, this can be considerably improved but a feedback system is still in development to cater to the changing conditions such as the size of the cell, refractive index with respect to its surroundings, the shape (currently only spherical or close to spherical objects can be trapped), temperature variations due to heating of the substrate material, etc.

Warszawa, Luty 07, 2024

Temat rozprawy doktorskiej

Raman-integrated Microfluidic Device for Rapid Non-invasive Imaging of Leukaemic Cells

Autor rozprawy doktorskiej: **Shreyas Kandhadai Vasantham, MTech**

Promotor: **Prof. hab. Piotr Garstecki**

Promotor pomocnicy: **Dr Ladislav Derzsi**

Streszczenie

Od ponad czterech dekad szczypce optyczne są przedmiotem intensywnych badań naukowców na całym świecie mających na celu wykorzystanie światła laserowego do chwytania, zatrzymywania i manipulowania obiektami w mikro i nanoskali, przyczyniając się tym samym do znacznego postępu w rozwoju technologii pojedynczych cząsteczek. Nasze badania pozwoliły na opracowanie, zbadanie i eksperymentalne zademonstrowanie nowatorskiej pułapki optycznej na chipie, która została zbudowana w oparciu o połączenie laserów światłowodowych z technologią mikrofluidyczną. Rozwiązanie to umożliwia chwytanie pojedynczych cząsteczek poprzez wytworzenie równowagi pomiędzy działającymi na nie siłami optycznymi i hydrodynamicznymi. W odróżnieniu od dotychczas stosowanych metod wykorzystujących skupione promieniowanie lub kilka laserów do pułapkowania, nasze innowacyjne rozwiązanie bazuje na użyciu jednej rozbieżnej wiązki laserowej doprowadzonej do mikrokanału za pomocą światłowodu jednomodowego, co pozwala na znaczne zmniejszenie obciążenia cząsteczki.

Nasze opto-hydrodynamiczne szczypce pozwoliły na przeprowadzenie szeregu różnych manipulacji schwytanymi cząsteczkami i komórkami, takich jak, na przykład, ich izolowanie, przesuwanie czy obrót. Dzięki wykorzystaniu trójwymiarowego skupiania hydrodynamicznego narzędzie to umożliwia zatem kontrolę trajektorii przepływu. Schwytana cząsteczka może zostać przesunięta na znaczną, do 500 μm, odległość wzdłuż mikrokanału, co pozwala na użycie różnych metod detekcji optycznej, a zatem na zwiększenie funkcjonalności układu. W naszej pracy, stworzona opto-mikrofluidyczna pułapka została zintegrowana z mikroskopem wymuszonego rozpraszania Ramana w celu obrazowania zatrzymanych komórek białaczki. Zbudowane w

ten sposób innowacyjne urządzenie diagnostyczne oferuje bezznacznikową, nieinwazyjną metodę badania i analizy składu komórek zawierających m.in. białka, kwasy nukleinowe i lipidy, dokonując pomiaru przy różnych długościach fali w kilka sekund.

Wykorzystanie wyjątkowej synergii pomiędzy mikrofluidyką, szczypcami optycznymi oraz mikroskopią Ramanowską stanowi niezwykle obiecujący krok naprzód w kierunku całkowitej zmiany podejścia i otwarcia się na nowe spojrzenie w medycynie spersonalizowanej.

Główną jednak przeszkodą ograniczającą zastosowanie naszego rozwiązania w praktyce, a zarazem głównym jego wyzwaniem jest zapewnienie stabilności i niezawodności chwytania i manipulacji niezależnie od rodzaju cząsteczki. Zależy to przede wszystkim od sztywności pułapki, a zatem wiąże się z kontrolą mocy lasera na wyjściu ze światłowodu oraz wahań pola przepływu. Stabilność tą można znacznie poprawić przy wysokich prędkościach przepływu, co wymaga zastosowania, będącego nadal w fazie rozwoju, systemu sprzężenia zwrotnego pozwalającego na uwzględnienie zmieniających się warunków, w tym, na przykład, rozmiaru cząsteczki, jej współczynnika załamania względem otoczenia, jej kształtu (obecnie tylko sferyczne lub prawie sferyczne obiekty mogą zostać pułapkowane), zmian temperatury spowodowanych podgrzewaniem się materiału podłoża, itp.

Thesis Structure

This dissertation is split into six chapters and includes work from two papers I have co-authored.

Chapter 1 introduces the aims of the thesis and various tools available for single-cell manipulation and analysis.

Chapter 2 provides the necessary prerequisite knowledge to understand the theory and governing equations in microfluidics. Further, it briefly discusses Raman spectroscopy combined with optical tweezers.

Chapter 3 details the development of a novel opto-hydrodynamic tweezer (OHT) system. It discusses the fabrication, characterisation, and working principle in detail. It also analyses various forces in the delivery and trapping of particles.

Chapter 4 describes all possible operations on single cells in the OHT system from trapping and translation to isolation and rotation. The various particles that can be trapped are discussed.

Chapter 5 combines stimulated Raman microscopy with the OHT platform for non-invasive leukaemic cell imaging. The different Raman bands of single cells are studied and critical information required to discern healthy cells from cancerous ones is discussed in this chapter. It also demonstrates a comparative study between different cell types and their spectral images.

Chapter 6 concludes the thesis and sheds light on the shortcomings, improvements, and future directions in this area of research.

This thesis is developed as part of a larger consortium project with leading institutions from across Poland such as Jagiellonian University in Krakow, Institute of Physical Chemistry, Laser Center, Warsaw University, Medical University of Łódź, Institute of Haematology and Blood Transfusion, and the Microfluidics group headed by Prof. Piotr Garstecki at the Institute of Physical Chemistry, Polish Academy of Sciences, Warsaw as part of the Foundation for Polish Science (FNP) FNP TEAM-NET grant POIR.04.04.00-00-16ED/18-00. The objective of the consortium was to develop a microfluidic stimulated Raman scattering based cell sorting device for rapid imaging of live cells in leukaemia diagnostics. At the heart of this project is the microfluidic system

for manipulation and sorting of cells which was developed as a part of this thesis. In summary, the goal was to develop a Raman-compatible microfluidic platform which can be readily utilized by clinicians for leukaemia diagnostics.

Sic parvis magna

“From small things, arise great things.”

– Sir Francis Drake

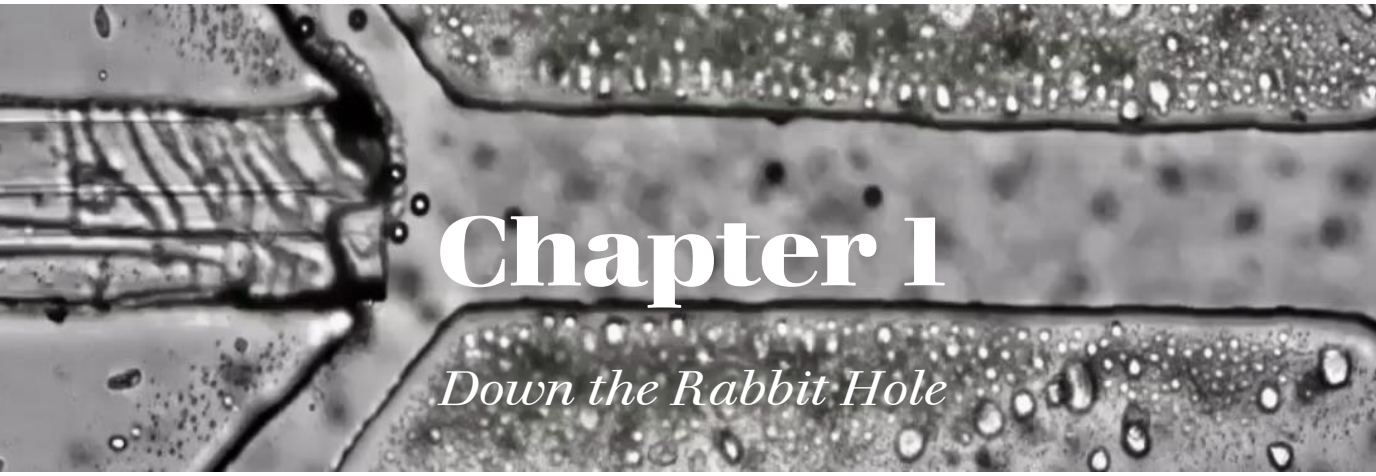

Chapter 1

Down the Rabbit Hole

"Would you tell me, please, which way I ought to go from here?"

— Lewis Carroll in *Alice's Adventures in Wonderland*

1. Introduction

1.1 Problem Statement and Thesis Aims

Leukaemia ranks as the 13th most prevalent cancer in adults and holds the unfortunate distinction of being the most common type of cancer in children. According to a report from the Global Cancer Observatory, an estimated 474,519 new cases were diagnosed in 2020 alone, accounting for 2.6% of all cancers (1). While the precise cause of leukaemia remains elusive, scientists and clinicians continue to study the various triggers contributing to its incidence in addition to investigating the genetic components involved.

Prevailing leukaemia diagnostic techniques involve complex immunohistochemistry and a series of intricate assays that lead to inconclusive results after prolonged consultations with experts and medical representatives (2,3). The existing diagnostic regimen for rapid leukaemia prognosis is characterised by its tedious and technically challenging nature (4–6). The current imperative, therefore, is to swiftly enhance and modernise existing diagnostic tools to address leukaemia effectively.

Spectroscopic techniques, especially Raman spectroscopy, have emerged as a powerful tool for leukaemia diagnostics and research. It exhibits high sensitivity and specificity to the molecular fingerprints of the cells, is non-invasive, and does not require additional sample preparation steps such as fluorescent labelling or markers for identifying cellular components.

This thesis endeavoured to advance leukaemia diagnostics by innovating Raman-compatible microfluidic devices to image single cells and their constituents. The primary focus was on tackling three pivotal challenges in the diagnostic process: precise and continuous cell delivery for the detection of Raman signals; stable immobilisation for Raman imaging; and efficient sorting of desired cells post Raman acquisition for further downstream assays, chemosensitivity studies, and immunohistochemistry.

The stepwise workflow was as follows:

1. Fabrication of a Raman-compatible microfluidic device using state-of-the-art fabrication techniques. The goal was to minimise background Raman signal that could potentially interfere with the signal from the cells. This was achieved by minimising the thickness of the device at the Raman acquisition window. The constraints imposed by the Raman microscope to integrate the device between two large objectives were also taken into consideration during the design and fabrication of the device.

2. Focusing and delivery of the cells to the region of interest (RoI) one by one, with a high spatial precision. This was achieved by employing 3D hydrodynamic focusing within the microfluidic device, which allowed excellent control of the flow trajectories in the X, Y, and Z axes.

3. Trapping cells at precise locations in the microchannel using optical tweezers integrated on-chip. A fiber-based diode laser was integrated with the microchannel to facilitate the trapping of the single cells flowing through the device. This improved the portability of the device compared to large flow cytometers which typically have immobile components. Additionally, various other operations on single cells—such as translation, rotation, and isolation—were demonstrated within the device.

4. Sorting cells of interest for further downstream assays and analyses. Sorting was achieved via two approaches: optical fiber–assisted sorting and sheath flow-assisted sorting. Both these methods have their advantages and disadvantages and have been discussed in detail in later chapters.

The combination of precise control and manipulation of single cells offered by microfluidics, in tandem with the molecular resolution of Raman, within a single lab-on-a-chip device will pave the way for new developments in rapid diagnostics of leukaemia.

This document consolidates my findings and serves to establish an edifice of knowledge for pursuing further research in this domain.

1.2 Tools for Single-cell Manipulation and Analysis

Investigation of particles and cells from the perspective of an individual particle or cell unlocks a comprehensive and holistic understanding of their behaviour, interactions, and impact on biological and engineered systems (7–13). Reports about variability in the Adenosine triphosphate (ATP) levels of cells within the same population have been attributed to the dynamics in the mitochondria, regulation of gene expression, or metabolic pathways. Single-cell approaches to quantify cellular ATP have been proposed to understand the correlation between the genetic pathways and corresponding phenotypic response (14,15). Thus, understanding the response of single cells reveals information which is obscured when studying the population as a whole (16–18). For example, circulating tumour cells (CTCs) have been identified by analysing single cells from human blood, thereby facilitating early detection of cancers (19–21). Similar studies involving the investigation of the biophysical and biochemical composition of single cells have implications that are fundamental to disease diagnosis and drug discovery (22–32). Characterising the phenotypic and genotypic features of single bacteria or viruses provides insights into the heterogeneity of these populations, which is crucial for designing effective antibiotics and vaccines (33–40).

There are several unique challenges to address before manipulating single cells. These challenges arise owing to their size and the high concentration of cellular components. Early methods for single-cell analysis relied heavily on flow cytometry or laser scanning cytometry for rapid screening of fluorescently labelled cells in a flow (41,42). Although flow cytometers are mostly automated and capable of integrating multiple detectors, they are bulky, mechanically complex, and can only be operated by a professional with extensive training and experience.

Miniaturisation of bulky systems has always been attractive and recent advances in the field of microfluidics have opened promising avenues for single-cell manipulation and analysis (43–48). Microfluidic techniques allow the integration of various functionalities into one platform while offering flexibility in design for real-time analysis. Owing to their miniaturisation, microfluidic systems typically work with a few hundred nanolitres or picolitres of sample solution, minimising sample loss and resulting in

sensitive approaches (49,50). Hence, developing tools and techniques to isolate, detect, and analyse individual particles with high spatial and temporal resolution in a lab-on-chip format is indispensable to the progress of single-particle science and technology (51–53).

Diverse particle manipulation strategies (54) relying on mechanical (55,56); optical (57,58); electrical (59–61); acoustic (62,63); hydrodynamic (64,65); or a combination of these forces (66–69); have been applied successfully to single-cell research.

Droplet microfluidics is one such emerging area where single-cell research is thriving (70–72). The cells are compartmentalised and encapsulated into an emulsion whose size scale is similar to that of a cell, and its environment is well-controlled. Droplets are generated by flowing two immiscible liquids through micron-sized channels. The flows are controlled precisely by syringe pumps and the geometries are specifically engraved to achieve monodisperse droplets, such as T-junctions, flow focusing, and co-flow systems. The droplets are stabilised by surfactants and single-cell encapsulation follows a Poisson distribution.

Although droplet microfluidics presents itself as one of the best tools for single-cell research, two-phase systems add to the complexity of deciphering Raman signals and could potentially hinder the signal from the cell. Because the encapsulated cell is freely moving within the droplet, the control over its movement is minimal. This is challenging, especially for imaging applications that require the cell to be static for a few seconds. Therefore, in this thesis, I focus on single-phase systems enabling control over the cell movement and simplifying Raman analysis by reducing interferences around the sample.

Similar to how biologists use multi-well plates for parallel analyses of various combinations of samples, within microfluidics, a usual method to isolate and trap single cells is by fabricating geometrical structures that function as barricades, walls, or wells (73,74). Microwells are a fine example of one such method wherein the diameter, number of wells, and shape can be tuned to suit the needs of the research (75–77). Revzin et al. (78) demonstrate an array of microwells for the retrieval of individual leukocytes. Han et al. (79) report the mapping of a mouse cell atlas by analysing over 400,000 single cells in a microwell array—a high throughput low-cost platform for single-cell RNA (scRNA)-sequencing. Microwells offer an ideal platform for single-cell profiling with very high throughputs that depend on the total number of wells that can

be fabricated on the device. However, they offer limited control in the analysis and run a high risk of contamination during sample seeding due to being exposed to the surroundings.

Microfluidic valves (80) introduced by Stephen Quake in 2000 addressed some of the above-mentioned limitations of microwells. They offer high control as well as the ability to program the valves and automate operation. Lecault et al. (81) developed a microvalve-integrated microfluidic platform consisting of thousands of chambers enabling single hematopoietic stem cell proliferation analysis. Sun et al. (82) presented a novel valve-based microfluidic platform for on-chip cellular assays. The microvalves provided excellent control, facilitating precise exchange of the medium to study individual cells in well-controlled environments. They allowed for control and programmability but were accompanied by certain disadvantages: the fabrication of these valves is still quite complex, employs a multilayer fabrication process, and the operation of the devices requires precision pressure control systems.

Compared to the complexity involved in fabrication, hydrodynamic methods utilise the actuation of fluid flow to control particles. By manipulating the drag forces generated by the surrounding fluid flow precisely, hydrodynamic tweezers can manipulate individual particles within microfluidic devices (65,83–85). However, their intricate design and fabrication requirements to establish well-defined flow vortices and their sensitivity to flow disturbances pose challenges to achieving robust particle trapping and manipulation.

Dielectrophoretic (DEP) (86–89) and acoustic forces (90–92) offer alternative strategies for particle manipulation in microchannels due to their robust trapping capabilities, minimal damage to particles, and wide applicability. However, both these methods necessitate the integration of complex electrode structures that require specialised designs to create the 3D traps and introduce additional instruments, such as AC generators, resulting in complex and bulky lab-on-chip devices.

Thus far, optical tweezers have been the preferred method for particle manipulation, ranging from metallic to biological. However, their widespread use in academic laboratories is hindered by the need for high numerical aperture (NA) objective lenses, complex instrumentation, and high-intensity optical operation. Compact dual-beam optical fiber tweezers (93–98)—which employ two opposing, diverging beams from optical fibers to trap a single

particle—present a promising alternative to conventional objective-based tweezer systems. Their simple design, minimal instrumentation, reduced trapping intensities, and on-chip operation make them an appealing choice for industrial applications as well. However, limitations such as precise fiber alignment, unstable trapping in high flow rate environments, and restricted manipulation over long distances have limited their broader adoption. Single-fiber tweezers (99,100) address some of these limitations but at the expense of fabrication costs involving fiber lensing or tapering of the fibers. Table 1 summarises the commonly used particle manipulation approaches, the primary forces responsible, and their advantages and disadvantages.

Table 1. Comparison of Widely Used Single-cell Manipulation Approaches

Single-cell Manipulation Methods	Primary Forces	Advantages	Disadvantages	References
Geometrical constrictions/ mechanical methods	Drag forces	High throughput, simple fabrication process, label-free, and biocompatible	Lack of selectivity, poor sorting efficiencies, risk of contamination, and low controllability	(101,102)
Dielectrophoretic (DEP)	DEP force, electroosmosis	Ease of control, low cost, and integration of electrodes with microfluidics	Joule heating, issues with medium conductivity, low throughput, and operation requires complex instrumentation	(86,89)
Acoustic	Streaming and radiation forces	Biocompatible and noncontact manipulation	High costs, high operation complexity, and low throughput	(62,91,92,103)
Optical	Scattering and gradient forces	High precision, label-free, and noncontact manipulation	Low throughput, expensive instrumentation, high operation complexity, and cell damage from focused lasers	(104,105)
Opto-hydrodynamic	Drag, scattering, and gradient forces	High precision, easy fabrication process, excellent integration with microscopy and spectroscopy techniques, biocompatible, noncontact manipulation, and minimal damage to cells due to diverging laser source	Low throughput and low sorting efficiency	this work (106–108)

This chapter outlined the major drawbacks of the current diagnostic regime of leukaemia. I briefly introduced the workflow to address these drawbacks.

This chapter also tabulates the importance of single-cell manipulation tools, various approaches, and their advantages and disadvantages. In the next chapter, I will discuss the theoretical background, focusing on the concepts of microfluidics, optical tweezers, and Raman spectroscopy.

Chapter 2

Microfluidics: A Story of Size

2.1 Definition of Microfluidics

Microfluidics involves manipulating and precisely controlling fluid flows at the microscale. The field has evolved significantly in the past few decades owing to interdisciplinary research, and its applications from the point of view of a scientist are constantly evolving. From the perspective of a physicist, microfluidics involves employing devices for the study of fluid behaviour through small channels. From the standpoint of a biologist, it means developing a system to isolate single cells from the culture medium with precision and study the dynamics of living systems when exposed to fluids (usually accompanied by imaging). In a chemist's world, it involves the intermixing of fluids for synthesis in specifically designed channels to engineer or mimic conditions that would otherwise prove challenging to achieve. More synonymously, the field is now expanding to the use of micron-sized channels that drive fluids for various applications, commonly referred to as "lab on a chip". Figure 1 highlights the importance of microfluidic devices and their operations along the length and volume scales.

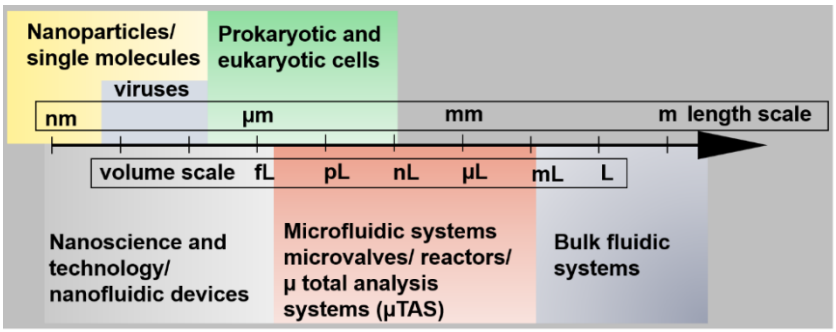

Figure 1: Importance of length and volume scales as size reduces.

2.2 Historical Perspective

The semiconductor industry had an astounding impact on the development of microfluidics as a standalone field of research. The initial development of integrated circuits (ICs) back in the 1950s propelled a revolution in microelectronics. This led to the building of sophisticated systems, electronic devices, and machines with applications in the fields of communication, medicine, and national security. Synonymous with the fabrication of the IC devices, microfluidic devices were soon fabricated on silicon wafers thanks to Lathrop and Nall (1952), who coined the term "photolithography" to pattern transistors made of germanium for military applications (109). Manz et al. pointed out the many advantages of studying flow physics on the micrometre scale and proposed the first micro total analytical system (μTAS) (110). This was the first footprint of total analysis systems as a concept and led to the development of handheld devices capable of performing bulky chemistry within microchannels.

Another strong factor driving the development of microfluidics was national security related. With the Cold War at its end, the use of biochemical weapons caused widespread unrest and led to the development of microelectromechanical systems in the 1990s; the Defense Advanced Research Projects Agency, USA (DARPA), spearheaded research and development to deploy portable devices to detect these threats (111).

In summary, the developments in the semiconductor industry, the introduction of patterning through photolithography, and the need for portable devices for various applications, propelled the development and adoption of microfluidics as we know it now.

2.3 PDMS: The Cornerstone Material for Microfluidics

The choice of material imposes several constraints when considering the requirements for microanalytical systems. Applications involving imaging of biological samples or cell cultures encouraged scientists to look for materials that were easy to fabricate, transparent, cost-effective, and biocompatible. Silicon was opaque, expensive, and offered limited integration of optical modalities. Glass was an excellent alternative to silicon and offered excellent imaging quality but the fabrication and selective etching of geometries and intricate valves was challenging. Plastics overcame many of these limitations

and one material—PDMS—became so popular that it continues to be the go-to material for device fabrication.

A research group, led by George Whitesides at Harvard, pioneered the use of polydimethylsiloxane or PDMS for the rapid prototyping of microfluidic devices (112). Soft lithography, as described by Whitesides, involves the use of elastomeric materials as stamps that are cast from a master mould. The master mould, which has a desired pattern, is fabricated via traditional photolithography techniques, micromachining, or other sophisticated techniques such as laser ablation (113,114). The desired pattern is replicated onto the elastomer and is hence referred to as "replica moulding". The prepolymer and curing agent are mixed in appropriate ratios before being poured onto the mould. The PDMS channels can be bonded covalently to either PDMS or glass after the plasma activation of the surface withstanding fluid pressures for operation.

The replication of valves, pumps, or complex channel architectures onto PDMS obtained via conventional silicon lithography is straightforward and cuts down the requirements of expensive clean rooms. PDMS is optically transparent, has low autofluorescence, and is an excellent choice for research where imaging or optical detection is non-comprising. It is permeable to gases facilitating cell culture (115) within the device and is relatively inexpensive compared to silicon. It is widely employed in the fabrication and mass-production of microfluidic devices. The structure consists of an alkane backbone, silicon, and oxygen as shown in Figure 2.

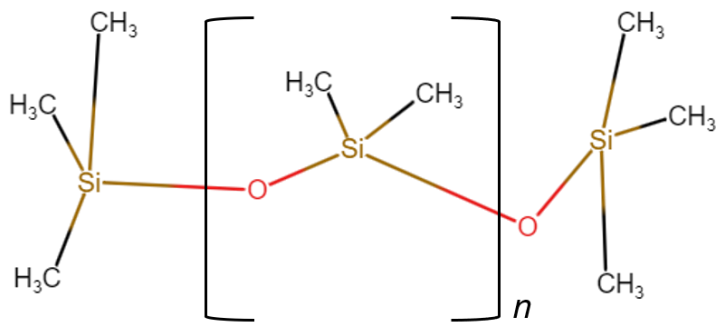

Figure 2: Chemical structure of polydimethylsiloxane (PDMS). '*n*' is the number of monomer chains.

2.4 Theory and Governing Equations

As the name suggests, microfluidic devices all have one thing in common: they are small. This characteristic offers many advantages but the most prominent one is the need for reduced sample volumes and reagents. Typically, the volumes handled by these devices are in the *nL–μL*. The use of reduced amounts of reagents and miniaturisation consequently lower the overall costs for fabrication and operation. The miniaturised devices are quickly replicated using soft lithography to produce a large number of batches. The technique utilises a hard master mould onto which patterns are fabricated and a soft polymer is poured into the mould, which hardens and cures when subjected to chemical treatment and temperature.

A fluid can be defined as either a gas or a liquid, wherein, there is a continuous deformation due to an applied external force or a shear stress. The physics of fluids in the microscale offers considerable advantages as compared to the bulk systems, where the interaction between fluids is primarily convective. In bulk systems, the inertial forces are much larger and, therefore, more dominant than the viscosity of the system. At the micron scale, however, the surface-to-volume ratio is large and these viscous forces are significant relative to the inertial forces and, thus, cannot be disregarded. This inconsistency in the action of the forces at different length scales gives rise to interesting effects. Therefore, it is essential to characterise fluid flow to understand and take advantage of these effects.

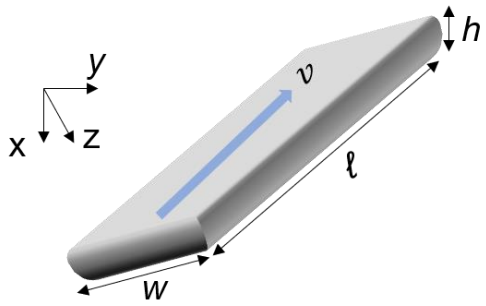

Figure 3: Example of a rectangular microchannel characterised by length *l*, width *w*, and height *h*. The fluid flow within the channel flows with a characteristic velocity *v*.

Dimensionless numbers are used to characterise the various phenomena at the microscale. Consider a fluid flowing with velocity (v) within a rectangular channel with length (l), width (w), and height (h) as shown in Figure 3.

One such parameter is the dimensionless Reynold's number (R_e) (116) given by the ratio of the inertial forces to viscous forces within a fluidic system.

$$R_e = \frac{\rho v l}{\mu} \qquad \ldots(1)$$

where ρ is the density of the fluid, v is its velocity, l is the characteristic length scale of the system, and μ is the dynamic viscosity.

When the dimension of the system is reduced, as is in the case of microfluidic systems, R_e is reduced considerably. When R_e is below 2,000, the flow within such systems enters a laminar regime as compared to R_e above 4,000, where the flow is turbulent. In turbulent systems, fluids are continuously undergoing mixing chaotically, which significantly enhances the presence of gradients within the system due to the vortices and eddies in flow.

To best understand these two flow regimes, one can imagine water flowing from a tap. The moment you begin to turn the tap on—when the volume of water is still small (Figure 4a)—the flow is transparent and smooth, with negligible mixing. Such a flow can be divided into individual lanes, or *laminae*, which are predictable. In contrast, when the tap is fully turned on and a lot of water gushes out of the nozzle unpredictably, there is considerable mixing (Figure 4b). The former is referred to as the laminar regime while the latter is the turbulent regime.

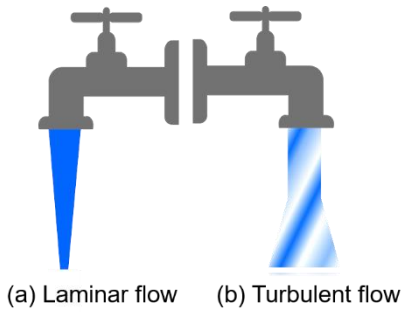

Figure 4: Example of (a) laminar and (b) turbulent flow regimes.

Certain boundary conditions are assumed at the walls of the microchannel. Due to pressure-driven flow, the fluid velocity at the walls is zero. This is referred to as the no-slip boundary condition resulting in the development of a parabolic flow profile within the main channel and the highest velocity is at the centre (Figure 5).

Another crucial dimensionless number is the Péclet number (P_e), which is the ratio of the convection to the diffusion in the system. Depending on the application of the respective research, diffusive mixing may be desired or not. Within microfluidic systems, control over diffusion is of utmost importance to achieve precise control and tailor microfluidic devices for specific end-goal applications.

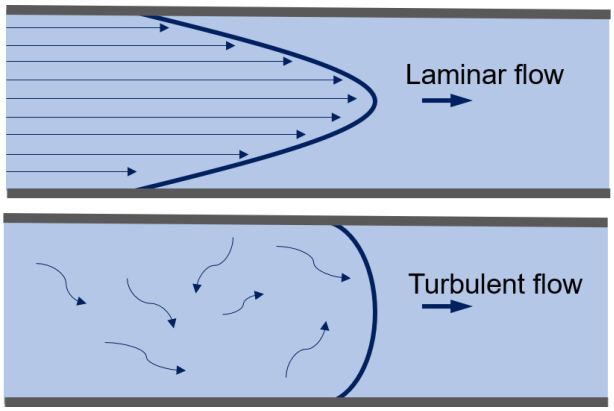

Figure 5: Velocity flow profile in a rectangular microchannel for laminar and turbulent flow regimes.

Due to the miniaturisation, the diffusion time is rather short in microchannels. The diffusion time can be approximated as:

$$t_d \approx \frac{x^2}{2D} \qquad \ldots(2)$$

where x is defined as the distance traversed by a single solute molecule along one axis after a certain time t_d and D is the diffusion coefficient of the solute.

If the velocity of the particle in-flow for a given width of the channel is known, P_e can be estimated using equation 3:

$$P_e = \frac{vL_0}{D} \quad \ldots(3)$$

The Navier-Stokes equation is used to describe the flow of fluids and is essentially a modification of Newton's second law of motion ($F = ma$):

$$\rho\left[\left(\frac{\partial u}{\partial t}\right) + (u \cdot \nabla)u\right] = -\nabla_p + \eta\nabla^2 u + f \quad \ldots(4)$$

where ρ is the fluid density, u is the fluid velocity, p is the pressure, and η is the dynamic viscosity.

The change in fluid momentum is described by the left side of the above equation. The change in velocity over time is given by the term $\rho\left(\frac{\partial u}{\partial t}\right)$, and the relative change in velocity due to fluid movement is given by $\rho(u \cdot \nabla)u$. The pressure gradient is expressed by $-\nabla_p$ on the right. The viscous effects are incorporated in the term $\eta\nabla_u^2$, whereas the third term f denotes forces such as gravity, electrostatic interactions, etc.

Conversation of mass requires that,

$$\frac{\partial \rho}{\partial t} + \nabla \cdot (\rho u) = 0 \quad \ldots(5)$$

At a given time and space, the density is assumed to be constant and is expressed as the continuity equation:

$$\nabla \cdot u = 0 \quad \ldots(6)$$

The flow rate within the microfluidic devices is controlled by applying a pressure difference (Δp). The volumetric flow rate, Q, can be calculated by the Hagen-Poiseuille law:

$$\Delta p = R_h\, Q \quad \ldots(7)$$

where R_h is the hydraulic resistance. The flow rate is higher if the resistance is lower under an applied pressure difference.

Hydraulic resistance for a microchannel with rectangular and square or circular cross-sections attributed by height h, width w, length L, or radius R, respectively, can be expressed as:

$$R_h \approx \frac{12\eta L}{wh^3}\left(\frac{1}{1-0.63h/w}\right) \quad \ldots(8)$$

for a square cross-section,

$$R_h \approx \frac{28.4\eta L}{h^4} \quad \ldots(9)$$

or, for a circular cross section,

$$R_h \approx \frac{8\eta L}{\pi R^4}$$

The flow profile within a microchannel is parabolic with the highest velocity at the centre of the channel. By assuming the no-slip boundary condition and no influence of the inertial forces, the flow velocity along the channel can be described as in Figure 5 (a) and equation 10:

$$u_x(y) = u_{x_{max}}\left[1 - \left(1 - \frac{2y}{w}\right)^2\right] \quad \ldots(10)$$

where w is the width of the channel and $0<y<w$.

Capillary forces also begin to dominate in the microscales. It is the interfacial force that drives flow within narrow constrictions against gravitational forces; examples include, the rise of juice in a thin straw, wicking in plants allowing transport of water against gravity, soaking of sponges, etc. Many analytical

devices—such as micro paper analytical devices (μPAD), blood glucose meters, and pregnancy test devices—utilise capillary forces.

2.5 Raman Spectroscopy (RS)

Sir C. V. Raman first observed inelastic scattering of light back in 1923 when studying sunlight incident on a photographic filter to focus light onto dust-free liquid. He observed that some light passed through this filter, a phenomenon that could only be explained by the change in energy of the incident photons on the sample. When light impinges upon a material, it can give rise to various effects depending on the properties of the material: the light may scatter—that is, be reflected or refracted—or the material may either absorb it or transmit it. Most of the light which is incident on the sample undergoes Rayleigh scattering. This is an elastic effect, meaning that the total momentum is conserved and the intensity is proportional to λ^{-4}. The photon that is incident excites the molecule to a short-lived, virtual excited state (typically 10^{-14} seconds) and eventually returns to the ground state. This process results in the emission of a photon and possesses the same energy as that of the transition. Effectively, the scattered photons have the same wavelength as that of the incident-impinging photon. The ground state level is denoted by E_0. The dotted lines represent the short-lived virtual states. The inherent vibrations of molecules give rise to the virtual energy states above the ground state.

The Raman effect occurs when the photon either loses or gains energy during the process resulting in a change in wavelength. If the wavelength decreases, it is termed “Raman anti-Stokes scattering”, and if it increases then it is termed “Raman Stokes scattering” as described in the energy level diagram in Figure 6. Raman scattering is a rare event as compared to Rayleigh scattering and occurs approximately every 10^7 photons that are incident on the sample.

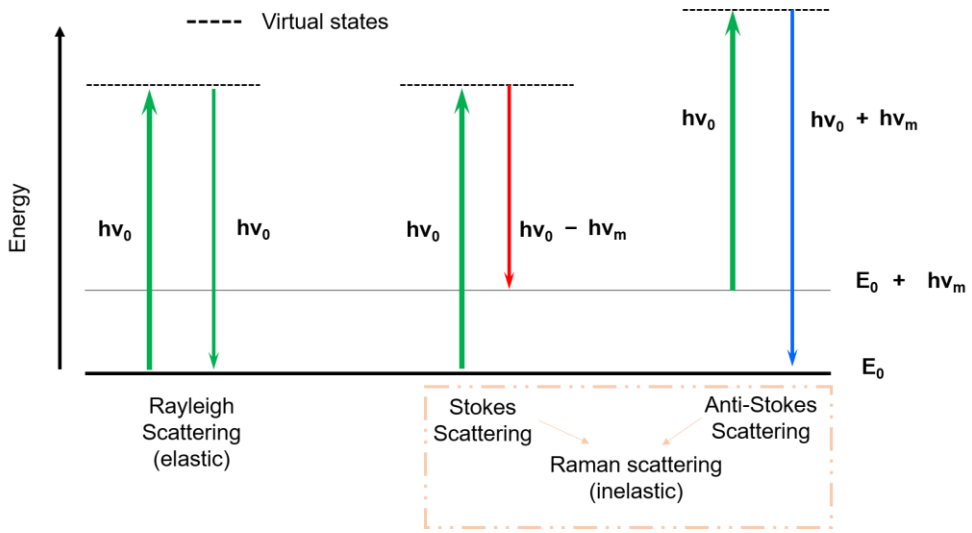

Figure 6: Energy level diagrams for the Rayleigh and Raman scattering processes.

This loss/gain in energy resulting in a change in wavelength is termed "Raman shift". It is represented in wavenumber and is calculated as follows:

$$\Delta w_{shift} = \left(\frac{1}{\lambda_{exc}} - \frac{1}{\lambda_{em}}\right) \quad \ldots(11)$$

where Δw_{shift} is the Raman shift, represented usually in units of inverse centimetres, λ_{exc} is the excitation wavelength, and λ_{em} is the emission wavelength.

This scattered radiation is collected, and the corresponding spectrum obtained is analysed to distinguish between different materials. Different atoms and molecules interact with photons differently providing a unique spectrum. This spectrum is characteristic of the material and is sensitive to the vibrational states (117) within the sample. The typical Raman spectra of PDMS is shown in Figure 7.

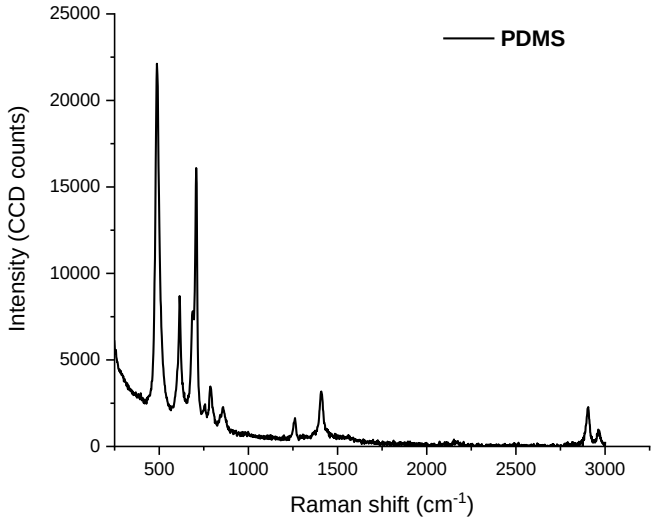

Figure 7: Typical Raman spectra of PDMS.

Raman spectroscopy greatly impacted the fields of biology and medicine, as it is a label-free, non-invasive, highly specific, and selective technique (118,119). The developments in the area of Raman spectroscopy can be attributed primarily to improving the low probability of spontaneous Raman scattering. With the advances in laser sources in the 1960s, scientists began to explore light-matter interactions involving multiple incidents (120) due to non-linear effects.

Stimulated Raman spectroscopy (SRS) is one such coherent non-linear process that provides much stronger signals in comparison to spontaneous Raman spectroscopy. The vibrational motions are time-resolved to study and image biological samples such as cells (121,122), biomolecules, (123) etc. SRS employs two lasers, which are separated in frequency, to initiate stimulated emission if the frequency differences correlate to the Raman vibrational mode being probed. The conditions for excitation are a complete spatiotemporal overlap of the pump and Stokes beam, with a Raman shift that matches the molecular vibration frequency of the sample. The interaction between the sample and the photons from the two laser sources results in an energy loss or energy gain depending on the polarizability of the sample. The energy loss is known as stimulated Raman loss (SRL). The energy gain is termed stimulated Raman gain (SRG). The overall Raman signal is deducted from

SRL or SRG to result in a Raman spectrum devoid of non-resonant background improving the fidelity of the spectrum.

This chapter looked at how forces in the micron scale give rise to fluid phenomena. It drew a roadmap of how microfluidics developed into the field it is today and the factors responsible for its popularisation. It briefly discussed the various materials employed in microfluidics as well as the reasons for PDMS as a widely accepted material for device fabrication within this community. I also reviewed the characteristics of fluid flow within microchannels and the governing equations. And, finally, this chapter also outlined the significance of Raman spectroscopy along with a brief description of stimulated Raman spectroscopy.

The next chapter will introduce “light force” and how its interaction with particles can be exploited to manipulate them. I will introduce the different optical forces, the background and literature behind the development of optical tweezers, and the various governing equations in the literature to estimate optical forces. I will then discuss how microfluidics and optical tweezers can be combined into a single powerful analytical tool for single-cell manipulation. The fabrication and operation principles of the microfluidic device will be detailed and followed by the results of focusing and trapping particles. I will also discuss and estimate the various forces acting on a particle within such a system in addition to the device parameters. A comparison of these parameters vis-à-vis other optical manipulation approaches will also be drawn.

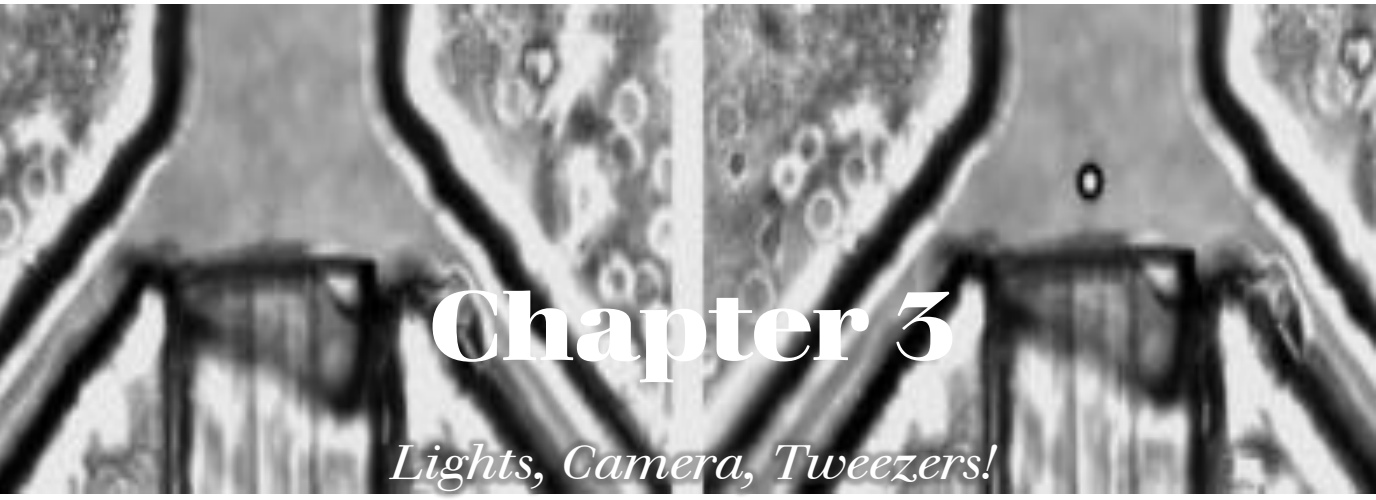

Chapter 3

Lights, Camera, Tweezers!

3.1 Radiation Pressure (light force) and its Origins

The force within light is carried by the quanta of electromagnetic radiation, that is, photons. These tiny packets of light are massless but possess momentum and energy. One macroscopic evidence of light force is a comet tail—a visible feature of the comets observed in space. Comet tails form due to tiny dust particles interacting with the sun's radiation, which causes them to be pushed away. The tail of a comet is always positioned away from the sun because there is a momentum transfer between the photons and the dust particles. This strange behaviour of comet tails always pointing away from the Sun was first observed in the 1600s by Johannes Kepler. Some two centuries later, in 1862, James Clerk Maxwell theorised that light has momentum and thus exerts pressure when incident on an object to explain the behaviour of electromagnetic fields. This pressure is now understood as a consequence of the law of conservation of momentum. The nature of light force can be thought of as a repulsive force, for example, the use of solar sails in the propulsion of spacecrafts (124).

3.2 Light–Particle Interactions

In order to understand how this force can be utilised to manipulate microscopic objects as described in Section 1.2, one needs to understand the interactions between light and matter. Consider an example where a spherical bead interacts with a ray of light. Assuming that the bead is reflective and is exposed to a light source, let us now discuss the momentum in the system. As is shown in Figure 8, if p_{in} is the momentum of the incident ray of light, upon interaction with the reflective spherical bead, the momentum of the light after reflection, p_{out}, will be:

$$p_{out} = -p_{in} \qquad \ldots(12)$$

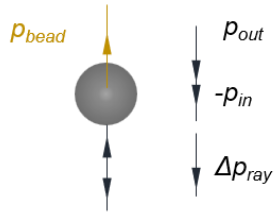

Figure 8: Interaction of a light ray with a spherical bead. The bead completely reflects the incident ray of light. The direction of net momentum pushes the bead towards the direction of the incident light ray.

According to the law of conservation of momentum, the total amount of momentum before and after interaction with the bead must remain the same, that is, the momentum gained by the bead can be expressed as:

$$p_{bead} = -(p_{out} - p_{in}) \quad \ldots(13)$$

From Newton's second law, the definition of force is mass times acceleration of the given object. However, since light never accelerates and is made of photons—which are essentially massless—we can conclude that light exerts a force by exchanging momentum. This phenomenon is known as "radiation pressure". The force scales with frequency,[1] which means that the higher the frequency of light, the larger the momentum it carries, and therefore, the more capable it is of exerting a stronger force on the object. In simple terms, blue light—a smaller wavelength—is capable of exerting a stronger force on an object than red light—a larger wavelength.

In the above example, we discussed a situation where the bead is reflective (equation 13). What if the bead happens to let all the light through instead of reflecting it? Let us now consider the case of a transparent bead. As light propagates through different media, the direction of light changes depending on the refractive indices of the media. Revisiting Snell's law we know that if

[1] Frequency of light relates to the energy of individual photons. Intensity of light is defined as the total number of photons per second.

the refractive index of one medium (n_1) is smaller in comparison to the second medium (n_2), the incident light ray will bend towards the normal to the surface as shown in Figure 9. If the refractive index of medium 1 is higher than medium 2, the light ray will bend away from the normal to the surface as in equation 14.

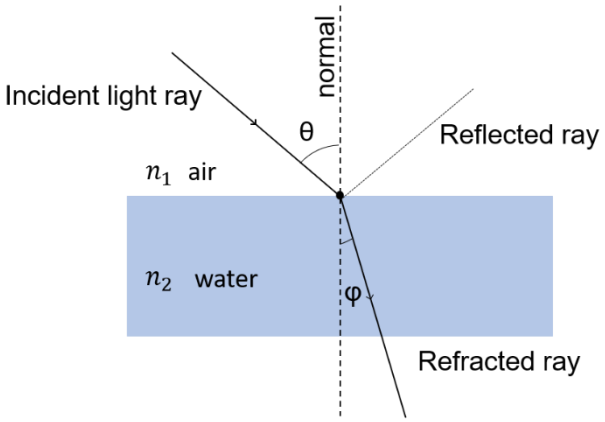

Figure 9: Snell's law and the principle of refraction.

$$\frac{sin\,\Theta}{sin\,\varphi} = \frac{n_2}{n_1} \qquad \ldots(14)$$

Let us return to our spherical bead. The light ray interacting with the bead will be deflected depending on the refractive index of the bead. If the refractive index of the bead is much larger than its surrounding medium (Figure 10), the outgoing light ray will be deflected. If we map out the overall change in the momentum of the system in a vector form, we can conclude that the beam of light will impart momentum to the bead. This exchange of momentum causes the bead to be pulled towards the beam of light. Following this, we can correlate the refractive index and its effect on the imparted momentum or the overall force on the bead. If the refractive index contrast between the bead and light is high, the light will be deflected more and, hence, the momentum gained by the bead will be larger.

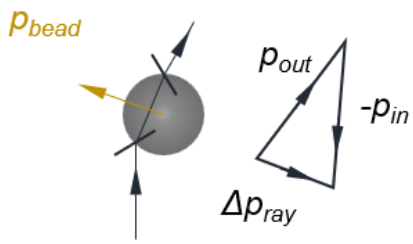

Figure 10: Interaction of a light ray with a spherical bead whose refractive index is larger than the surrounding medium. The incident light ray is deflected, and the bead gains momentum, causing it to be pulled towards the ray's axis.

Reflections reduce the magnitude of momentum, which has an effect on the force exerted on the bead as shown in Figure 11. Though the internal reflection of the bead is ignored here, it influences the direction and magnitude of the overall momentum exchange to the bead.

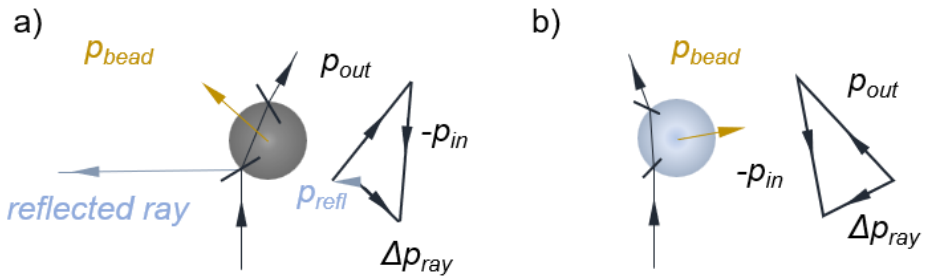

Figure 11: (a) The net momentum is reduced due to reflections. (b) According to Snell's law, if the refractive index of the bead is lower than the surrounding media, then the bead is pushed away from the incident ray.

With this information about the interaction of single rays of light, let us now consider a light beam composed of multiple rays defined by a uniform intensity profile. When this beam is incident on a bead, a pushing force is experienced by the bead, propelling the beam to propagate along the direction of the beam profile (Figure 12a). If the beam profile exhibits a gradient intensity—such as that of a Gaussian beam, which is collimated—the momentum in the middle of this beam is larger compared to the sides. This gradient intensity, when interacting with the bead, will either attract or pull the bead towards regions of maximum intensity. In this case, the centre of the beam is as in Figure 12 (b). The force responsible for pulling the beam

towards the area of maximum intensity is referred to as the “optical gradient force”, and the force that pushes the bead along the direction of the beam is called the “optical scattering force”. *These are the two forces primarily responsible for realising optical tweezers—a tool that utilises light force to trap and manipulate particles.*

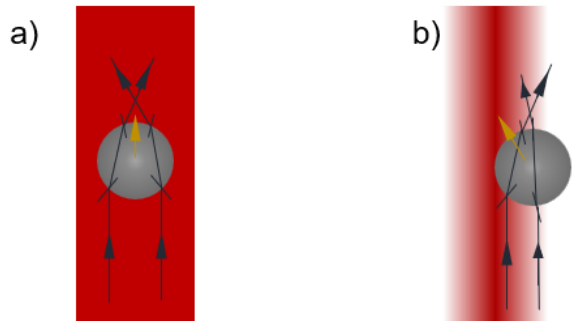

Figure 12: The beam of light interacts with a spherical bead. (a) Interaction of a bead with a beam of light of uniform intensity profile. (b) The bead interacts with a light beam composed of a Gaussian profile.

The optical gradient forces are responsible for stable trapping in 2D. However, since the scattering force still pushes the bead in the third dimension, this results in instability in the third dimension. To effectively stabilise the motion of the bead along the axial axis, the most intuitive approach would be to introduce a second beam propagating in the opposite direction of the initial beam. The scattering forces from the oppositely positioned beams will cancel each other, resulting in a trapped bead, stabilised in 3D. This technique remains effective even when the two opposing beams are positioned at sharp angles (Figure 13).

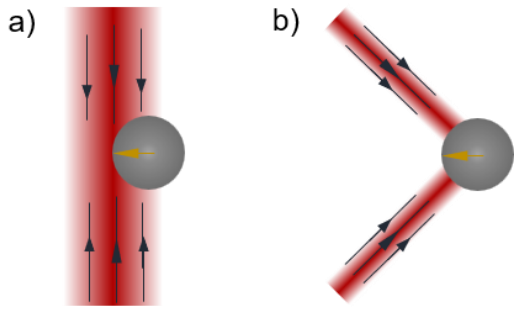

Figure 13*:* Interaction of collimated beams of light from (a) opposite sides and (b) at an angle to trap beads with high stability.

3.2.1 Arthur Ashkin and His Discovery

Arthur Ashkin realised that this effect of two laser sources was superfluous and could be reproduced within a single highly focused Gaussian beam (Figure 14) (104). He introduced this technique—which was initially termed "single-beam gradient force trap" and later recognised as optical tweezers—in his seminal paper (104). The effectiveness of this approach hinges on the utilisation of a lens with an exceptionally high numerical aperture (NA) to achieve a tightly focused beam of light. When this tightly focused beam interacts with a bead, regardless of its position in front of or behind the focus of the beam, the bead will be pulled towards the point where the gradient intensity is the highest or, simply, the focus of the beam.

Ashkin's discovery marked a paradigm shift in particle manipulation strategies, offering the ability to manipulate and study individual particles with unparalleled precision and paving the way for advancements on all fronts, including the fields of biology, chemistry, and physics.

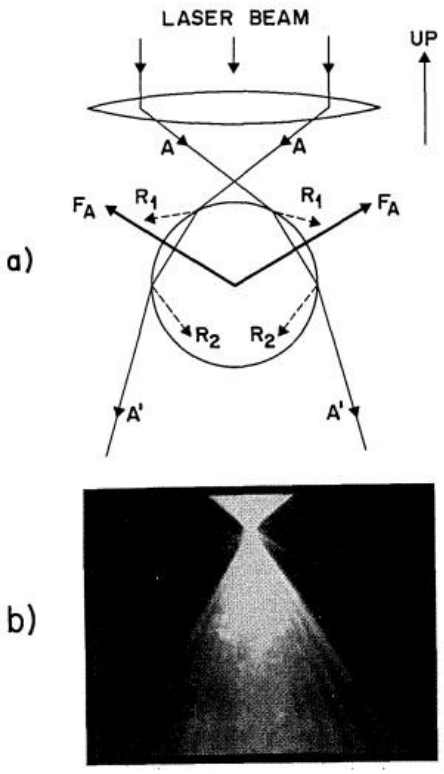

Figure 14: Particle trapped in a focused beam as published by Ashkin et al. (a) Diagram showing the ray optics of a spherical particle trapped in water by a focussed laser. (b) Photograph, taken in fluorescence, of a 10 μm sphere trapped in water, showing the paths of the incident and scattered light rays [Reproduced from Ashkin et al. (104) with permission ©The Optical Society.]

3.3 3D Hydrodynamic focusing

Before delving into the intricacies of the optical trapping employed in this thesis, let us first examine how the principles of microfluidics help harness fluid flow to focus and deliver cells within microchannels to facilitate trapping.

The technique we will discuss in this section was originally developed by Knight et al. (125) as a faster alternative to mixing in laminar regimes by controlling the diffusion at small length scales and was termed "hydrodynamic focusing". A fluorescent stream of dye particles is squeezed—or "hydrodynamically focused"—from both sides and the width of this focused stream is controlled by modulating the relative flow rates of the side and inlet

flows. In current research, hydrodynamic focusing is strongly associated with flow cytometers. A typical flow cytometer measures a population of cells in flow (126). Figure 15 depicts the optics and fluidics elements within a flow cytometer.

Modern flow cytometers combine particle focusing and manipulation methods with optical detection to sort individual cells. In order to measure a large population of cells, the flow velocities in such types of equipment are quite high, which results in inaccuracies due to the optics not being able to keep up with flow speeds. One method to resolve such inaccuracies in flow is by driving all the cells in the solution to a single location within the flow cytometer. This is achieved by employing fluid dynamics. A "sheath flow" is introduced to surround the "sample flow". The sheath fluid confines the sample stream and forces the cells to form a single file when passing through the detection point.

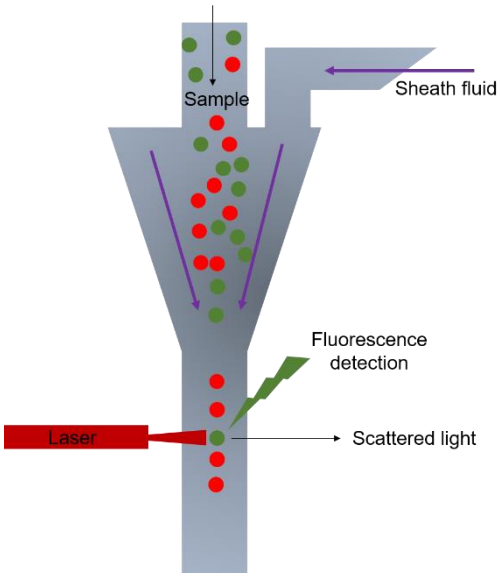

Figure 15: Optical and fluidic elements involved in the construction of a typical flow cytometer.

Although flow cytometers are versatile tools to study cells at extremely high throughputs, analyse single cells, and enable sorting, they are quite bulky and expensive and require a considerable level of expertise to operate. With advancements in microfluidics research, scientists are now aiming to miniaturise flow cytometers (127–129). The integration of various detection

modalities within a microfluidic flow cytometer has propelled research in various areas to expand detection capabilities. Several particle-focusing strategies employing sheath or sheath-less focusing have been demonstrated in the literature previously (130). However, most of them employ complex fabrication processes and impose constraints on applicable flow rates. The use of multilayer designs often makes the chip difficult to integrate with other components necessary to build the cytometer. Zhao et al. (131) have successfully employed a single-layer design of a microfluidic cytometer employing 3D hydrodynamic focusing to count basophils based on scattering. The selection of one method over the other is dependent on the needs of the research and factors such as design constraints, feasibility, throughput, and resolution.

The reader is acquainted with the basics of microfluidics, optical tweezers, and Raman spectroscopy, let us now look at how all this comes together within a microfluidic chip. The following sections delve into the fabrication and operational principles of the developed opto-hydrodynamic tweezer (OHT) chip. The platform combines microfluidics, optical tweezers, and stimulated Raman microscopy to create a unified and potent analytical system. It synergises the molecular precision and sensitivity of SRS with the control and efficiency of microfluidics and holds great potential as a diagnostic tool. The characterisation and calibration of the focusing effect of OHT are conducted out with respect to cells and polystyrene (PS) particles, which is discussed in detail in Section 3.6.

The experiments in this thesis were performed using 15 μm PS particles to validate the system. Thereafter, different cell lines were tested with the chip. Parameters such as the focusing accuracy, trapping stability, trap stiffness, etc., are measured and discussed in sections 3.6, 3.9, and 3.11, respectively. The variety of forces acting on the particle within the tweezer system is estimated and discussed in Section 3.7 and compared to other optical approaches.

3.4 Fabrication of the Microfluidic Chip

The AutoCAD software was used to draw and design the device geometries based on calculations of the hydrodynamic resistances and the overall requirements of the experiments. Standard photolithography was used to fabricate the necessary devices using SU 8 negative photoresist onto a 3-inch silicon (Si) wafer at exposed at 365 nm. Prior to clean room fabrication, the

designs were drawn and sent out for the printing of the photomasks. The resolution of the photomasks influences the quality of fabrication significantly, and therefore, the highest possible resolution is desired. The chip design and the PDMS chip with inlets, sheath flows, and outlet are shown in Figure 16.

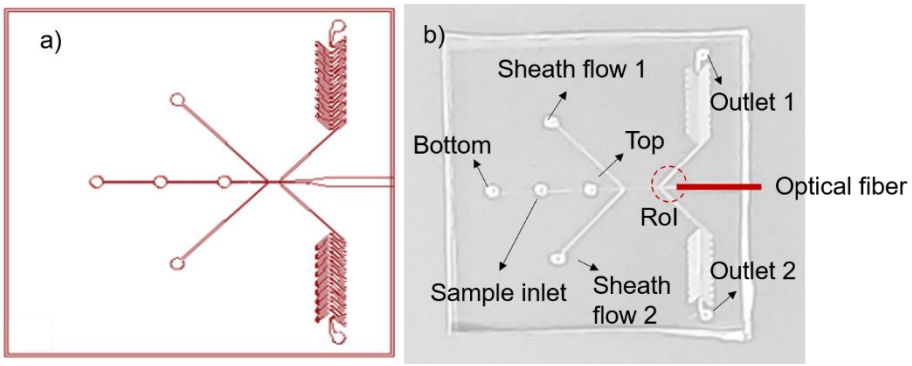

Figure 16: (a) AutoCAD design of the microfluidic chip. (b) The corresponding PDMS chip after fabrication is bonded on glass.

Figure 16 shows the inlets and outlets for the sheath flow and sample as the region of interest (RoI) (red, dotted circle). The RoI is a Raman window where the cells are trapped for Raman acquisition. Technical details of the fabrication process, chip assembly, and operation are discussed in detail in Appendix A1.

The 3-inch Si wafer is cleaned thoroughly and baked at 200°C. Post-baking, the wafer is gradually cooled to room temperature. SU-8 2100 photoresist (micro resist technology GmbH, Germany) is spin-coated as specified by the manufacturer onto the wafer and baked at 65°C and then at 95°C before exposure. The photomask with the desired pattern is aligned with the wafer on a mask aligner system to position the patterns onto the wafer and, consequently, exposed. Post-exposure, the wafer is carefully baked at 95°C as per the manufacturer's instructions. The wafer is developed and cured at 200°C for 15 minutes after which the master mould is ready. This master mould is used to produce PDMS replicates via soft lithography. The final PDMS stamp peeled from the wafer is activated by oxygen plasma and bonded to glass to obtain the final device.

3.5 Principle of OHT

The synergy between hydrodynamic forces and optical forces is exploited to realise equilibrium positions along the length of the channel to trap particles and cells. The unique geometry in the microfluidic device positions the optical fiber opposite to the direction of the fluid flow taking advantage of the forces acting on the particles to trap them at specific locations. Since the optical fiber is in direct contact with the flow, artefacts and losses resulting from material interfaces are minimised. The scheme presented in Figure 17 outlines the working principle of the OHT system.

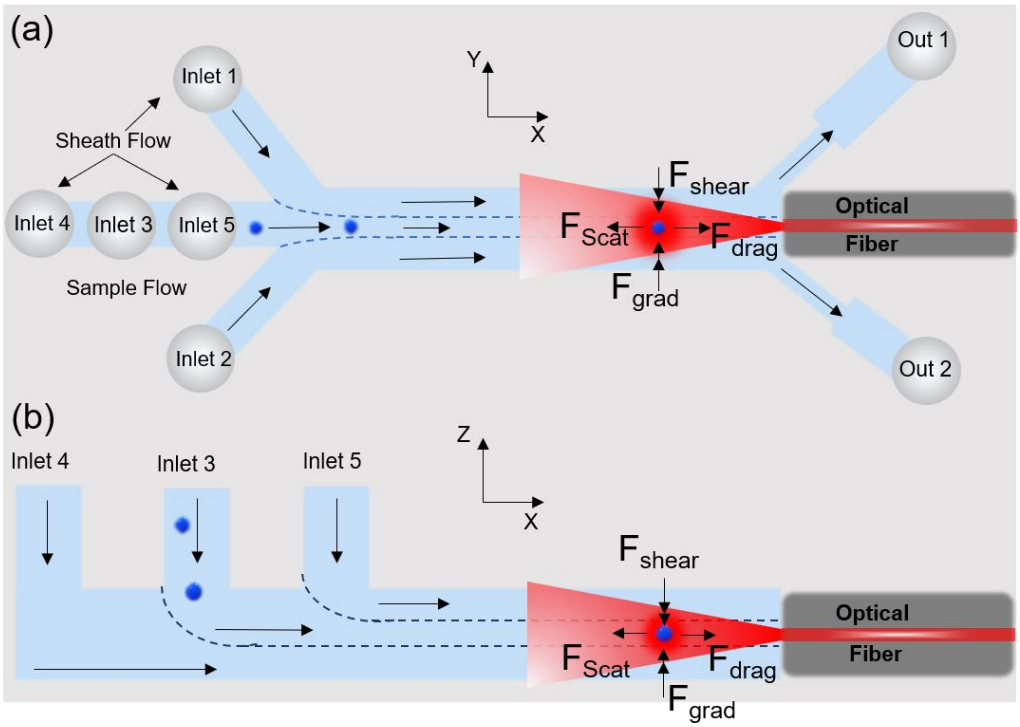

Figure 17: Operating principle of an OHT system. (a) Top view of the microfluidic device depicting the various inlets for sheath flow and the opposing fiber. (b) The cross-sectional view shows the influence of 3D hydrodynamic focusing to deliver particles/cells at designated locations within the channel by modulating the flow rates of the sheath flow. The various forces acting on the particle are depicted: F_{shear} (shear forces) and F_{drag} (drag forces) due to the fluid flow and the optical forces, respectively; F_{scat} and F_{grad} are the scattering and gradient forces, respectively, arising from the optical fiber due to the input laser power.

The optical fiber is a single-mode, polarization-maintaining fiber, with a core diameter of 6 µm, an NA of 0.12, and a mode field diameter of 6.6 µm at 980 nm. A dedicated tapered fiber guide structure on the microfluidic device ensures the easy insertion of the fiber. The fiber is glued in place to eliminate any fluctuations during the operation of the device. A UV epoxy resin of appropriate viscosity is used. The glue flows into the fiber guide structure via capillary action and is cured for 30 seconds with the help of a high-intensity UV gun.

A four-way sheath flow aligns the particles and cells flowing from the sample inlet with the optical axis of the fiber fixed at the opposite end. It is important to state that the four-way sheath flow enables control along the X, Y, and Z axes of the sample inlet. The side flows control the Y-direction of the sample while the top and bottom flows control the Z-direction. By precisely varying the concentration of the sample as well as the overall flow rate ratios of the sheath flows with respect to the sample stream, it is possible to align the flow trajectories of single cells to the optical axis of the fiber.

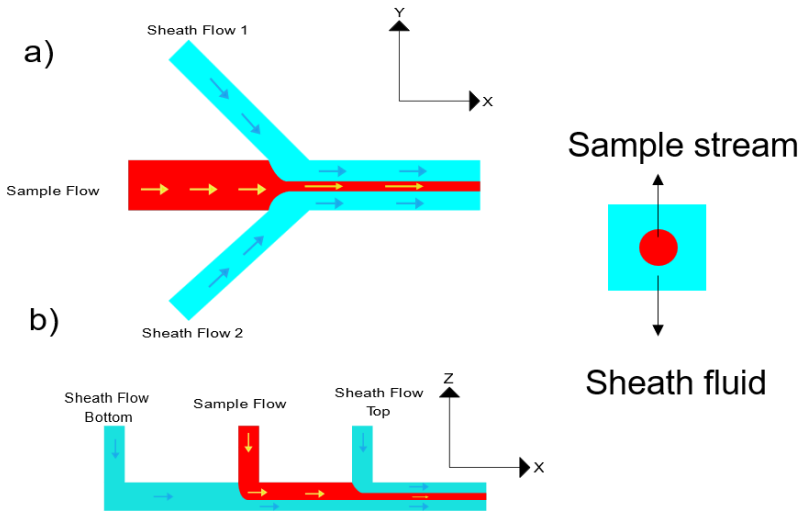

Figure 18: Sheath flow surrounding the sample stream in OHT and driving the cells at specific positions within the microchannel. (a) The top view and (b) cross-sectional view depict how the sheath flows squeeze the sample fluid in the respective axes. Adapted from (131).

The sample from inlet 3 is focused from the side (inlets 1 and 2) and from the bottom and top (inlets 4 and 5, respectively) as shown in Figure 18. As a consequence of laminar flows in the microchannel, the fluids in the channel flow parallelly with no disruption between the layers and negligible lateral mixing. By properly adjusting the flow rate ratios of the four sheath flows with respect to the sample flow, the trajectory of the sample stream can be manipulated hydrodynamically within the cross-section of the microchannel.

3.6 Focusing and Trapping of Microparticles in the OHT

Trapping within the OHT is realised by aligning the flow trajectories of the particles in the microchannel with the optical axis of the fiber. To demonstrate the effect of focusing and estimate trapping efficiencies, a 0.02% weight-to-volume of PS particles, whose diameter was 15 μm, is flown from inlet 3. In the absence of sheath flows, the PS beads flowed randomly within the channel, and the trapping efficiencies were very low as depicted in Figure 19. This is because the number of particles aligned with the core of the optical axis of the fiber was very low and distributed statistically.

When sheath flows 1 and 2 were activated, the particles slowly began to converge in the centre of the channel in a process called “2D focusing”. This forced more of the particles to align with the core of the fiber but only in the Y-direction as evidenced by the low trapping efficiencies. Along the cross-section, that is, in the Z-direction, the beads interacting with the laser of the fiber were low in number. Therefore, to improve trapping efficiency, the bottom and top sheath flows were increased steadily. This confined the flow of particles in the Z-direction, causing most of the particles to align with the optical axis of the fiber.

Consequently, the trapping efficiency increased and was found to be >70% as shown in Figure 19 for a laser power of 450 mW. To achieve higher trapping efficiencies, all the particles flowing in the channel must be aligned along the core of the optical fiber with high precision. This necessitates exceptionally high sheath flow rates leading to strong drag forces that cannot be counteracted by the optical forces in our system. 3D hydrodynamic focusing offers the flexibility to address positional inaccuracies in fiber placement within the channel. This is achieved by adjusting the ratio of the sheath flow rates to aid in the alignment of the particles along the optical axis of the fiber.

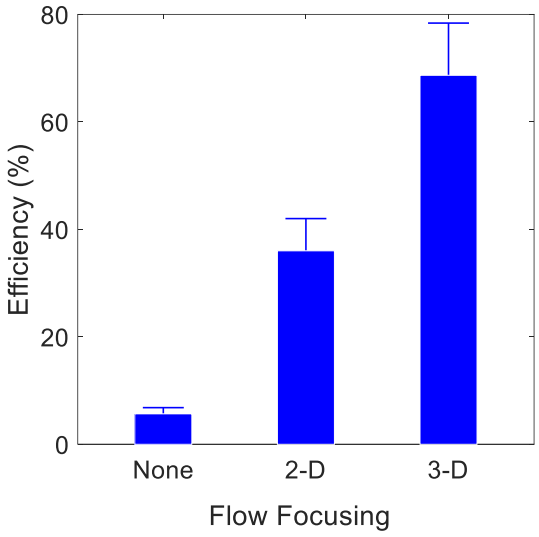

Figure 19: Trapping efficiency versus sheath flow focusing. The particles when focused along both horizontal and vertical axes resulted in high trapping efficiencies as compared to only one-axis focusing or no focusing.

To determine the accuracy of focusing particles within the device, two approaches were adopted. The first one involved the measurement of the centroid position of the PS beads flowing in the microchannel. The relative change in the position of the particles in Y-direction during flow is determined while varying the sheath flow rate between 0 µL/hr–100 µL/hr. The sample flow rate was fixed at 10 µL/hr. A custom MATLAB code was written to extract the centroid positions of beads from each frame of the video for different sheath flow rates. The Y-position of the bead was plotted as a function of the sheath flow rate from the side. A standard deviation of ±2 µm was observed at flow rates of 100 µL/hr as shown in Figure 20.

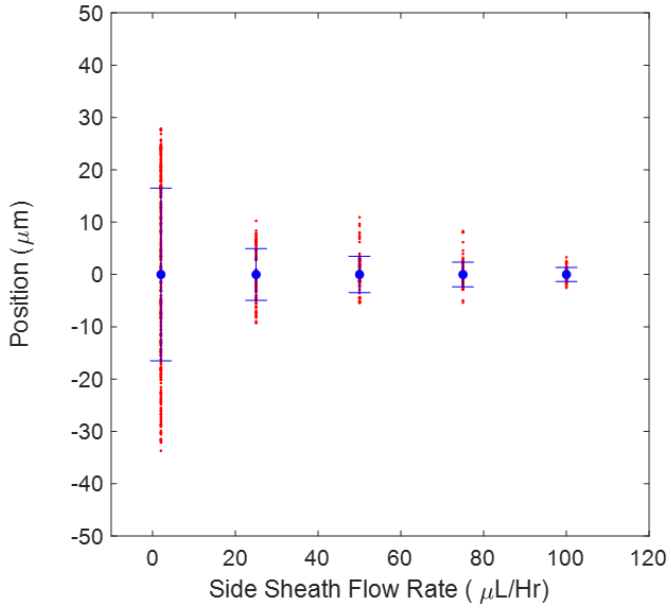

Figure 20: Particle position versus side sheath flow rate. The centroid position of PS particles flowing in the microchannel was extracted from the video sequence for different side sheath flow rates. The sample flow rate remained fixed at 10 μL/hr. Each point represents a single particle, and the error bar represents the mean and standard deviation in the positions.

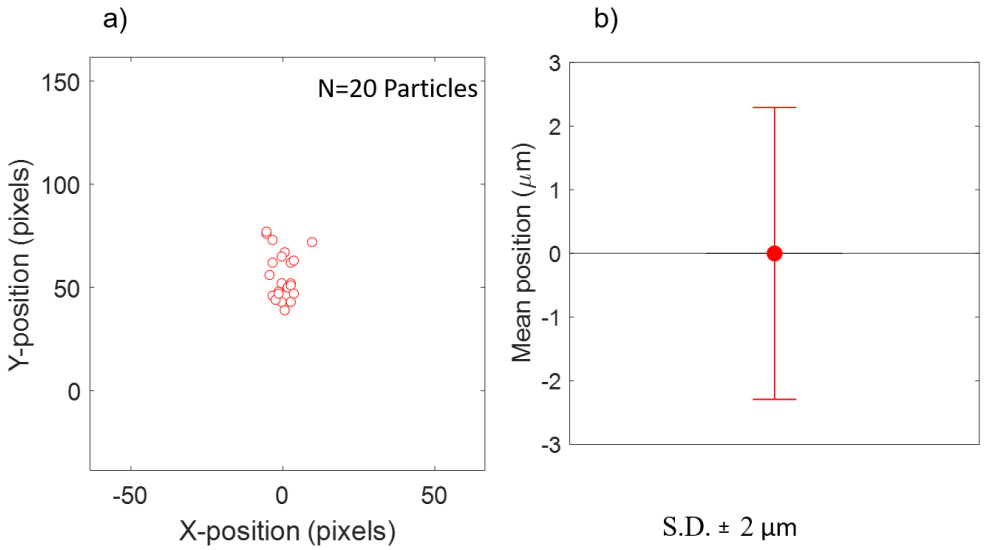

Figure 21: (a) The relative deviation in the X-position is measured for 20 particles after 3D hydrodynamic focusing. (b) The standard deviation was ±2 μm from the mean position.

From Figure 21 we can see that 3D hydrodynamic focusing constrains most of the particles to specific regions within the microchannel—in our case, the centre of the channel. The effect of focusing improves with an increasing sheath flow rate ratio. The standard deviation for 20 particles is calculated and in agreement with the centroid position method.

The other method to determine the quality of focusing utilised the software within the Nikon Ti2 eclipse microscope which was used to obtain video sequences during the experiments. Different RoIs were chosen within the microchannel to determine the accuracy of focusing. In this case, three regions along the X-direction were chosen to calculate the deviation of particles in this direction during flow. Most of the particles passed through the preferred RoI (marked in red). The standard deviation measured after 3D hydrodynamic focusing was ±2 μm. The relative error compared to the centroid measurement arises from the size of the chosen RoI (15 μm) and the relative distance between the RoIs (5 μm) as shown in Figure 22.

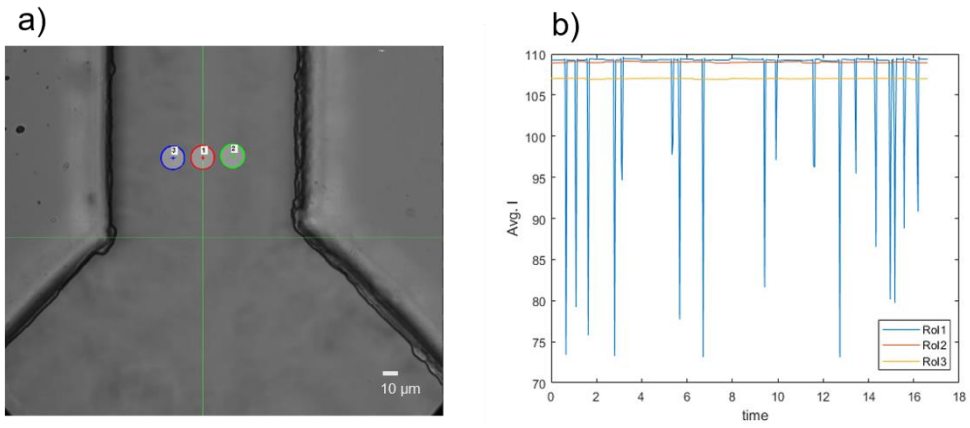

Figure 22: (a) Designated RoIs, marked along the X-direction of the channel, to determine the deviation in particle trajectory. (b) The total number of particles passing through RoI 1 after 3D hydrodynamic focusing. Each peak corresponds to one particle flowing through the region at a given instant.

In summary, 3D hydrodynamic focusing was realised and validated within OHT. PS beads with a diameter of 15 µm were successfully delivered to specific locations in the microchannel after hydrodynamic focusing. The effect of the sheath flow rate on the sample stream was studied to comment on the quality of focusing. The relative error in focusing was measured using two methods to compute the relative position of the bead during flow. The relative error estimated from the above methods after 3D hydrodynamic focusing of the beads was ±2 µm. The efficiency of focusing particles increased with an increase in the sheath flow rate.

3.7 Forces Within OHT

To estimate the forces within the OHT, we need to understand the beam profile of the laser at the output end of the fiber within the microchannel. Figure 24 shows the spatial intensity profile in the X–Y direction of the laser beam from the optical fiber core operating at an output power of 550 mW. The scattering due to the flow of 500 nm PS particles makes it possible to visualise the beam profile. A single-mode fiber with NA 0.12 is integrated into the open end of the microfluidic device from the side and glued in position with the help of a UV-curable epoxy resin.

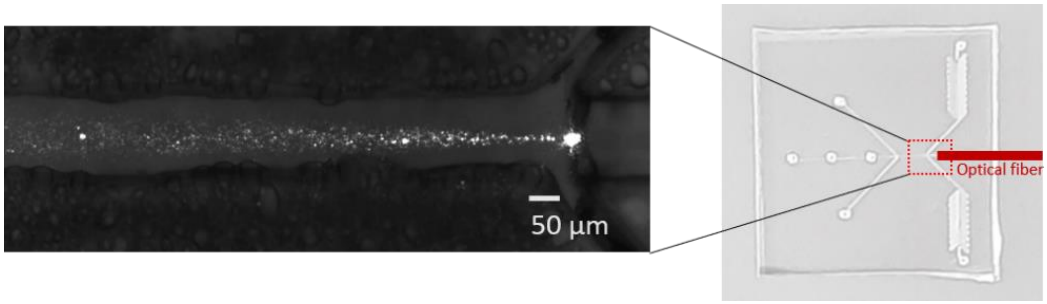

Figure 23: Beam profile visualised within the channel as a result of scattering due to 500 nm PS particles.

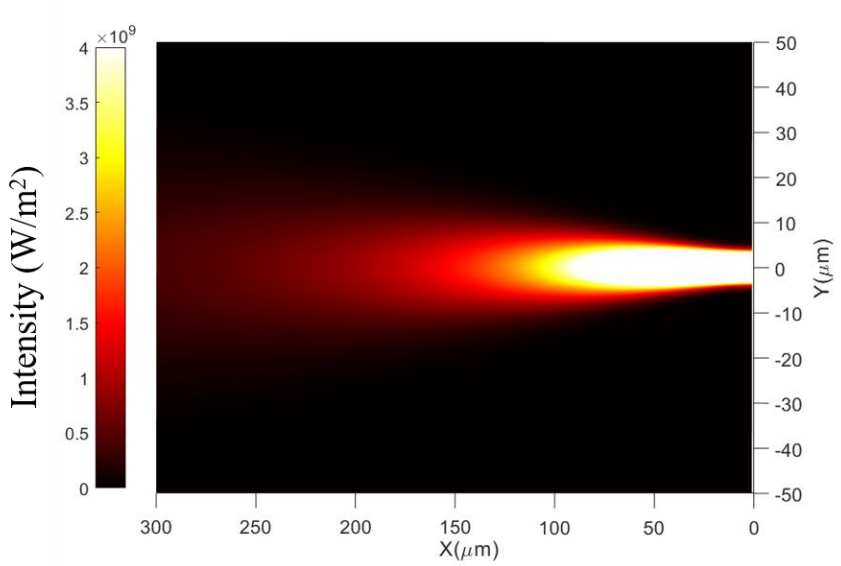

Figure 24: Intensity profile of the laser beam emitted from the single-mode optical fiber. The origin (Y = 0) marks the centre of the fiber core.

3.7.1 Estimation of Optical Forces Within OHT

In Section 3.2, we looked at light-particle interactions and understood the concepts of radiation pressure and momentum transfer. What we did not consider then is the size of the particle with respect to the wavelength of the interacting light beam. Optical trapping regimes can be understood by considering the size of the particle versus the wavelength of the trapping laser under a set of assumptions. Broadly, two such regimes exist, one where the size of the particle is much greater than the wavelength—the Mie regime—

and the other where the particle is much smaller than the trapping wavelength—the Rayleigh regime.

In the Rayleigh regime, the ray optics theory is not valid and, therefore, the particle needs to be considered as a point dipole to explain the forces. Since, my thesis focuses on biological cells, which are much larger than the wavelength of the trapping laser used here (≈980 nm), I will focus on the Mie regime. In the Mie regime, typically, ray optics are used to describe the trapping behaviour. Light from the laser is incident on the particle, which exerts a force owing to momentum change as discussed in sections 3.1 and 3.2. Since we have already discussed the concept of scattering and gradient forces, let us now look at how to estimate these forces within our system.

Ashkin studied and developed the tweezers based on the ray optics regime, which applies to non-spherical objects and different beam intensity profiles (105). He reported radiation force as qualitative values. Gauthier and Wallace (132) further expanded on his work to derive a closure form for the optical forces by describing what they referred to as the behaviour of the photon stream. Essentially, the stream of photons when incident on a spherical particle divides infinitely, continuously undergoing reflection and refraction as it traverses the sphere. From this photon stream interaction, they calculated the radiation force based on the number of photons interacting with the surface and undergoing a change in momentum.

$$p = \frac{n_m h}{\lambda} \qquad \ldots(15)$$

where n_m is the refractive index of the medium, h is Planck's constant, and λ is the wavelength of the light.

The Gaussian intensity profile at the output end of the fiber propagating in a medium of water (n = 1.33), is given by:

$$I(x,y) = I_o \exp\left(\frac{-2y^2}{w(x)^2}\right) = \frac{2P}{\pi {w_o}^2} \exp\left(\frac{-2y^2}{w(x)^2}\right) \qquad \ldots(16)$$

where, P is the total power of the beam, I_o is the peak irradiance at the centre of the beam, y is the radial distance away from the axis, $w(x)$ is the radius of

the laser beam where the irradiance is $\frac{1}{e^2}$ (13.5%) of I_o, and x is the distance propagated from the face-end of the fiber.

$$w_o = \frac{MFD}{2}\ w(x) = \frac{MFD}{2}\sqrt{1+\left(\frac{x}{x_r}\right)^2},\ x_r = \frac{\pi}{\lambda}\left(\frac{MFD}{2}\right)^2 \quad \ldots(17)$$

where *MFD* is the mode field diameter of the optical fiber (Figure 25). The width of the Gaussian intensity profile is described by the mode field diameter, which is constant along the length of the fiber and carries 86% of the beam power.

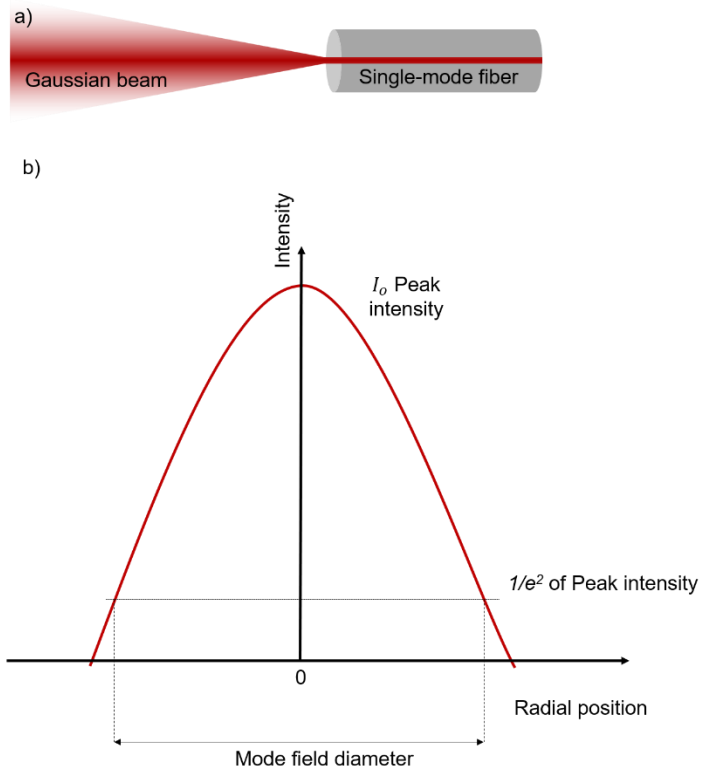

Figure 25: Gaussian profile intensity distribution at (a) the output of the single-mode optical fiber. (b) MFD estimation for the Gaussian beam.

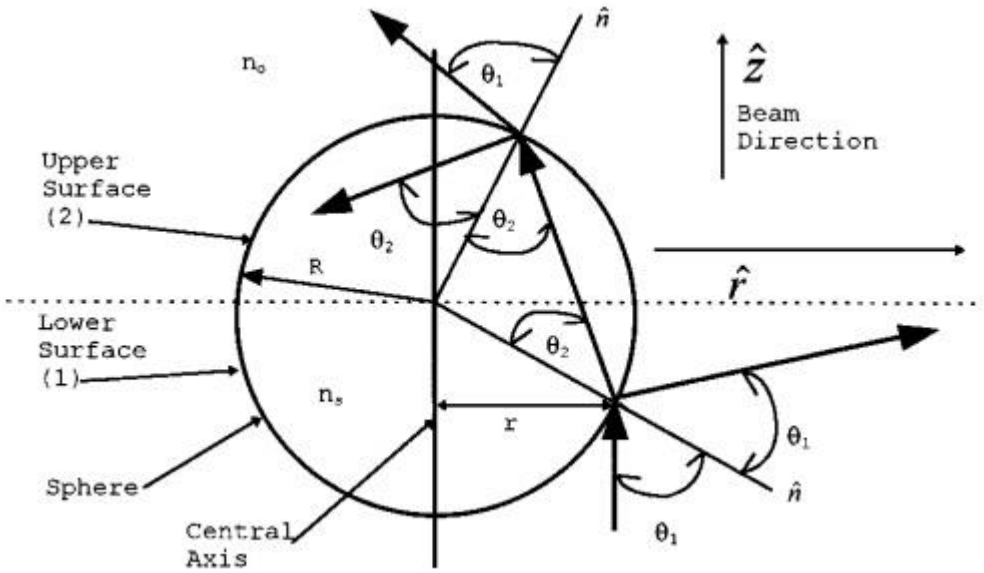

Figure 26: Stream of photons represented by a ray of light incident on the sphere. [Reproduced from Gauthier et al. (132) with permission ©The Optical Society.]

To calculate the mean number of photons within the photon stream as shown in Figure 26, Gauthier et al. considered an infinitesimal area normal to the direction of the beam. The photons are continuously undergoing reflection and refraction when encountering the surface of the bead. Therefore, an expression to determine the total number of photons in the Gaussian beam is given by:

$$N_k = \frac{\lambda}{hC} I(x,y) dA \Delta t \qquad \ldots(18)$$

Considering reflections and refractions, the initial number of photons N_k separate to N_{k1}, N_{k2} … N_{kn} as they interact at the interface. This interaction is expressed as a summation of the mean number of photons over all the interfaces.

$$N_k = \sum_{n=1}^{\infty} N_{k,n} \quad \ldots(19)$$

Using equation 19, the total number of photons N in the Gaussian beam is estimated as:

$$N = \sum_{k=1}^{\infty} N_k = \sum_{k=1}^{\infty} \sum_{n=1}^{\infty} N_{k,n} \quad \ldots(20)$$

The spherical bead experiences a momentum change owing to its interaction with the photon stream. The change in momentum in the axial and radial direction are expressed as:

axial,

$$\Delta p_z = \frac{n_0 h}{\lambda} N_k \left[1 + \frac{N_{k,1}}{N_k} cos\, 2\theta_1 - \sum_{n=2}^{\infty} \frac{N_{k,n}}{N_k} cos(\alpha + n\beta) \right] \quad \ldots(21)$$

radial,

$$\Delta_{P_r} = -\frac{n_0 h}{\lambda} N_k \left[\frac{N_{1,1}}{N_k} sin\, 2\theta_1 - \sum_{n=2}^{\infty} \frac{N_{1,n}}{N_k} sin(\alpha + n\beta) \right] cos\, \psi \quad \ldots(22)$$

where θ_1, with respect to the normal, is the angle of incidence of the stream of photons, θ_2 is the angle of refraction based on Snell's law, and ψ is the polar angle. Then:

$$\alpha = 2(\theta_1 + \theta_2)$$

$$\beta = (\pi - 2\theta_2)$$

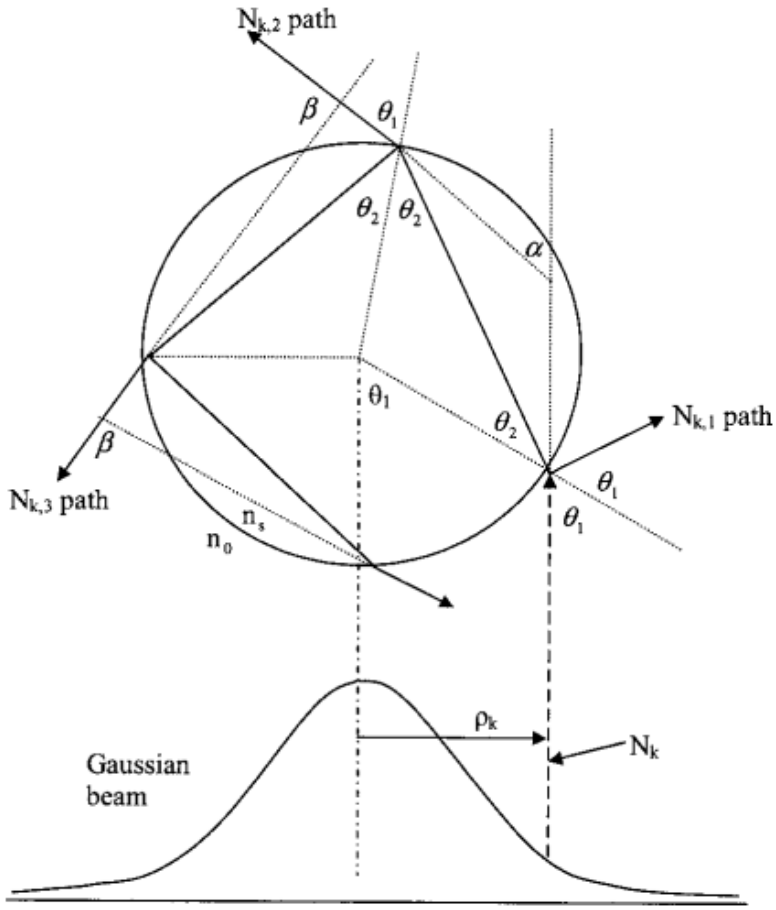

Figure 27*:* Geometry of a photon-stream path interacting with the Gaussian beam. [Reproduced from Kim et al. (133) with permission ©The Optical Society.]

Kim et al. (133) reported a simplified expression for the scattering and gradient forces based on the photon stream approach proposed by Gauthier et al. From Figure 27, by expressing the mean number of photons undergoing a change in momentum as a probability by combining the Fresnel reflectance and transmittance, we get:

$$N_{k_1 I} = N_{k,R} \qquad \ldots(23)$$

$$N_{k,n} = N_k R^{n-2} T^2 \text{ for n} \geq 2 \quad \ldots(24)$$

The Fresnel reflectance is expressed as:

$$R = \frac{1}{2}\left[\frac{sin^2(\theta_1 - \theta_2)}{sin^2(\theta_1 + \theta_2)} + \frac{tan^2(\theta_1 - \theta_2)}{tan^2(\theta_1 + \theta_2)}\right] \quad \ldots(25)$$

Assuming the absorption is zero, the transmission can be expressed as T=1–R.

By expressing the change in momentum as Fresnel reflectance and transmittance, the above equation for change in momentum becomes:

$$\Delta p_z = \frac{n_0 h}{\lambda} N_k \left[1 + R\,cos\,2\theta_1 - T^2 \frac{cos(2\theta_1 - 2\theta_2) + R\,cos\,2\theta_1}{1 + R^2 + 2R\,cos\,2\theta_2}\right] = \frac{n_0 h}{\lambda} N_k Q_z \quad \ldots(26)$$

$$\Delta_{P_r} = \frac{-n_0 h}{\lambda} N_k \left[R\,sin\,2\theta_1 - T^2 \frac{sin(2\theta_1 - 2\theta_2) + R\,sin\,2\theta_1}{1 + R^2 + 2R\,cos\,2\theta_2}\right] cos\,\psi$$

$$= \frac{n_0 h}{\lambda} N_k Q_r \quad \ldots(27)$$

The dimensionless coefficients for the scattering and gradient forces determined by Kim et al. were in agreement with the calculations presented by Ashkin (105).

The force equations can now be obtained by relating the above equations to Newton's second law:

$$F = \frac{\Delta p}{\Delta t} \quad \ldots(28)$$

$$dF_z = \frac{n_0}{c} I(\rho, z)\left[1 + R\,cos\,2\theta_1 - T^2 \frac{cos(2\theta_1 - 2\theta_2) + R\,cos\,2\theta_1}{1 + R^2 + 2R\,cos\,2\theta_2}\right] dA \quad \ldots(29)$$

$$dF_r = -\frac{n_0}{c} I(\rho, z) \left[R \sin 2\theta_1 - T^2 \frac{\sin(2\theta_1 - 2\theta_2) + R \sin 2\theta_1}{1 + R^2 + 2R \cos 2\theta_2} \right] \cos \psi \, dA \quad \ldots(30)$$

The radial distance from the centre of the Gaussian beam of the photon stream is expressed as ρ:

$$\rho^2 = a^2 + r_p^2 \sin^2 \theta_1 - 2ar_p \sin \theta_1 \cos \psi \quad \ldots(31)$$

where r_p is the radius of the spherical bead and a is the offset of the sphere in the radial direction from the axis of the Gaussian beam.

The scattering and gradient forces expressed in double integrals can be written as:

$$F_s = \frac{n_0}{2c} \int_0^{2\pi} \int_0^{\pi/2} I(\rho, z) \left[1 + R \cos 2\theta_1 - T^2 \frac{\cos(2\theta_1 - 2\theta_2) + R \cos 2\theta_1}{1 + R^2 + 2R \cos 2\theta_2} \right] r_p^2 \sin 2\theta_1 d\theta_1 \, d\psi \quad \ldots(32)$$

$$F_g = -\frac{n_0}{2c} \int_0^{2\pi} \int_0^{\pi/2} I(\rho, z) \left[R \sin 2\theta_1 - T^2 \frac{\sin(2\theta_1 - 2\theta_2) + R \sin 2\theta_1}{1 + R^2 + 2R \cos 2\theta_2} \right] r_p^2 \sin 2\theta_1 \cos \psi \, d\theta_1 \, d\psi \quad \ldots(33)$$

Based on the expressions for the optical forces in equations 32 and 33, we can estimate the optical forces for a PS particle trapped in our OHT system For a particle significantly larger than the wavelength of the trapping light source, the scattering and gradient forces on the particle within the channel can be calculated using equations 34 and 35:

$$F_{scat}(x, y) = \frac{n_m a^2}{2c} \int_0^{2\pi} \int_0^{\frac{\pi}{2}} I(x, y) Q_{scat} \sin(2\theta_1) \, d\theta_1 d\varphi \quad \ldots(34)$$

$$F_{grad}(x,y) = \frac{-n_m a^2}{2c} \int_0^{2\pi} \int_0^{\frac{\pi}{2}} I(x,y) Q_{grad} \sin(2\theta_1) cos\varphi \, d\theta_1 d\varphi \quad \ldots(35)$$

where n_m is the refractive index of the medium, a is the radius of the trapped particle, and c is the speed of light. Q_{scat} and Q_{grad} are given as:

$$Q_{scat} = \left[1 + Rcos(2\theta_1) - T^2 \frac{cos(2\theta_1 - 2\theta_2) + Rcos(2\theta_1)}{1 + R^2 + 2Rcos(2\theta_2)}\right] \quad \ldots(36)$$

$$Q_{grad} = \left[Rsin(2\theta_1) - T^2 \frac{sin(2\theta_1 - 2\theta_2) + Rsin(2\theta_1)}{1 + R^2 + 2Rcos(2\theta_2)}\right] \quad \ldots(37)$$

where R and T are the Fresnel reflection and transmission coefficients for optical rays' incident at an angle θ_1 and θ_2 is the angle of refraction calculated using Snell's law.

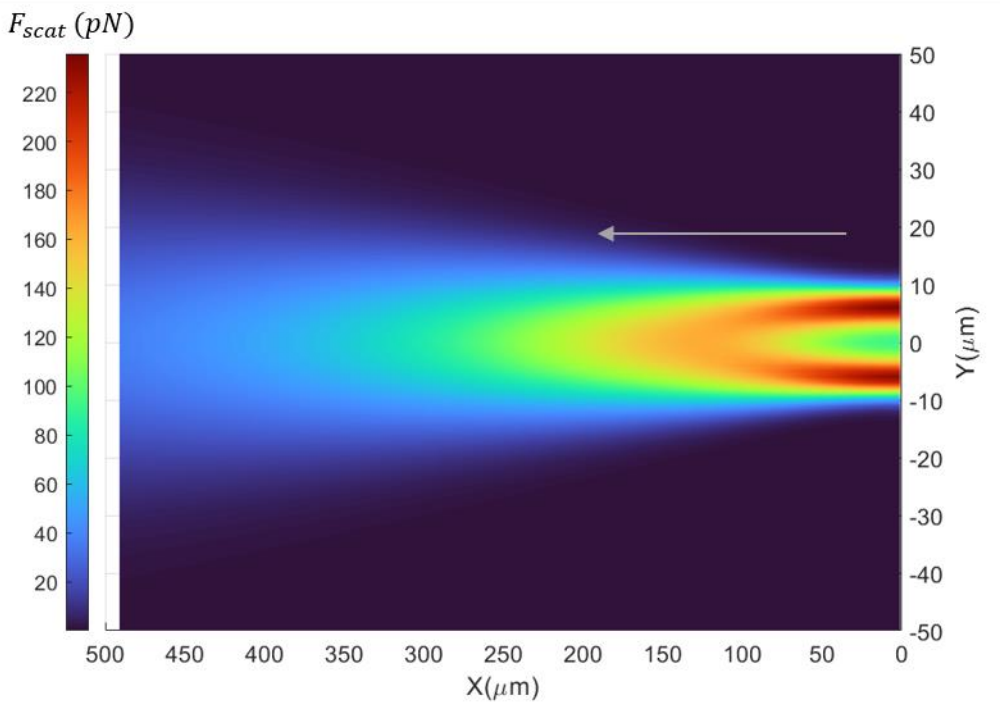

Figure 28: Spatial distribution of the optical scattering force exerted by the laser beam from an optical fiber on a 15 µm PS bead flowing in the microfluidic channel. (Core diameter of the fiber = 6.4 µm, $\lambda_{laser} = 973\ nm$, $Power\ (P) = 550\ mW$, NA = 0.12).

The spatial distribution of the optical scattering force exerted on a 15 µm PS particle flowing in the microfluidic channel for a given laser power, derived using equation 34, is illustrated in Figure 28. The scattering force is maximum along the laser beam axis and reduces with increasing distance from the tip of the optical fiber. This is attributed to the Gaussian intensity distribution of the laser beam within the optical fiber. Since the fiber acts as a diverging laser source, the scattering forces are strongest at the fiber end (X = 0, Y = 0) and decrease as the particle moves away from this position. This results in reduced optical intensities, lowering scattering forces and, consequently, minimising photodamage to the particle.

In the transverse direction, the gradient force on a particle that flows in alignment with the optical axis of the fiber is zero as calculated from equation 35 and depicted in Figure 29. Initially, the gradient forces increase with an increase in the displacement of the particle from the beam axis and then

decrease significantly as the particle is completely displaced from the beam path. The maximum gradient force is observed at a displacement where the beam divergence is equal to the size of the particle, which results in a maximum overlap of the light cone with the particle. A consequence of this trend is the automatic alignment of particles that were not perfectly aligned with the optical beam axis already. These particles are pulled into the beam axis due to gradient forces and are eventually trapped.

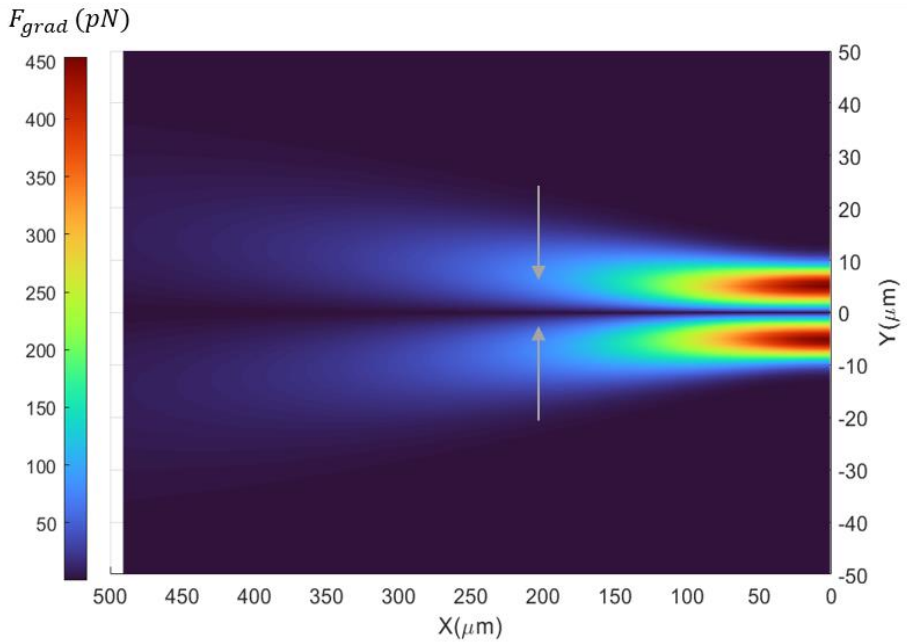

Figure 29: The gradient force exerted by the laser beam from an optical fiber on a 15 μm PS bead flowing in the microfluidic channel.

3.7.2 Estimation of Non-optical Forces Within the OHT

A particle trapped in the OHT system experiences a variety of forces, including optical forces (scattering and gradient), fluidic forces (hydrodynamic drag, shear gradient, and wall lift), and other forces (gravitational and buoyant).

The hydrodynamic drag forces on a particle flowing within the microchannel are calculated using the Stokes law:

$$F_{drag} = 6\pi\eta a v \qquad \ldots(38)$$

where η is the dynamic viscosity of the fluid and v is the flow velocity in the microfluidic channel.

The drag force is dependent on the overall flow velocity in the channel. The trap location can be modulated by varying the input flow rates to translate the trapped particle along the length of the channel.

The buoyant force acting on a rigid spherical particle suspended in a medium is given by:

$$F_b = \frac{4}{3}\pi a^3 \rho_m g \quad \ldots(39)$$

The gravitational force is given by:

$$F_s = \frac{4}{3}\pi a^3 \rho_P g \quad \ldots(40)$$

where ρ_m and ρ_p are the density of the medium and particle, respectively, a is the radius of the particle, and g is the acceleration due to gravity.

The lift forces are given by (134–136):

shear-gradient lift forces,

$$F_{SL} \propto \rho_m v^2 \frac{a^3}{H} \quad \ldots(41)$$

and wall lift forces,

$$F_{WL} \propto \rho_m v^2 \frac{a^6}{H^4} \quad \ldots(42)$$

where ρ_m is the density of the medium, v is the maximum flow velocity, a is the radius of the particle, and H is the characteristic dimension of the channel. Then, for rectangular channel:

$$H = \frac{2wh}{(w+h)}$$

where w and h are the width and height of the channel.

Since 3D hydrodynamic focusing ensures that particles are aligned with the optical axis of the fiber—which is close to the centre of the channel (within ± 10 μm) and further away from the channel walls—the magnitude of the inertial lift forces acting on the particle is almost three orders of magnitude smaller than the optical trapping forces in our geometry and, therefore, the lift forces do not contribute to the trapping forces. The major forces at play are the optical scattering and hydrodynamic drag forces, which are responsible for the stable trapping of the particle within the OHT platform.

The channel geometries employed in this design (125 μm × 125 μm) and the flow constraints that squeeze the sample stream towards the centre of the channel ensure that the net effects due to the wall forces are balanced on either side. The gravitational and buoyant forces estimated based on the relations given in equations 39 and 40 are an order of magnitude lesser compared to the optical and drag forces and, therefore, their influence in the trapping process is minimal and neglected here.

3.8 Comparison of Optical Tweezing Approaches

In comparison to the widely available tweezing approaches, OHT offers several advantages as shown in Table 2. Traditional objective-based tweezers employ high NA objectives that are quite bulky and expensive. The operation is limited to small working distances, requires complex optics to complement the setup, and reduces the portability of the assembly. Fiber-based tweezers were developed to replace the bulky objectives and improve the portability of the setup while still retaining the advantages of tweezing. Dual-beam and single-beam fiber tweezers have gained significant popularity owing to their smaller size and the ability to be integrated with lab-on-chip devices performing challenging biology, especially as an optical stretcher (94) probing single cells.

However, the use of fiber-based tweezers is still limited due to the requirement of precise alignment tools and stages. The integration of the fibers with microfluidic devices involves implementing complex fabrication techniques, which increases costs as well as the complexity of the operation. The manipulation of particles at high flow rates is challenging and the operations on a single particle are limited to trapping, stretching, and sorting. OHT offers a novel optofluidic arrangement to trap, translate, rotate, and sort single particles within the same device. It can operate at high flow rate conditions up to 4,500 μm/s and translate the trapped particle over 500 μm

along the length of the channel. It also offers the ability to trap particles in a linear chain array, further promoting the integration of various spectroscopy and microscopy techniques to probe single particles rapidly.

Table 2. Comparison of the widely available tweezing approaches

	Objective-based optical tweezers	**Dual-beam fiber tweezers**	**Single-beam fiber tweezers**	**Evanescent wave trapping**	**Opto-hydrodynamic tweezers (OHT)**
Trapping force (dominant)	Optical gradient	Optical gradient and scattering	Optical gradient	Optical near-field gradient	Optical scattering and hydrodynamic drag
Direction of flow (vis-à-vis trapping laser direction)	Orthogonal	Orthogonal	Orthogonal	Orthogonal	Parallel
Trapping particle size	0.2 nm–5 μm	50 nm–100 μm	100 nm–15μm	10 nm–5μm	3μm–50 μm
Numerical aperture	1.2–1.4	0.1–0.2	0.1–0.2	0.17–0.19	0.12
Operational flow velocities	Up to 1,400 μm/s	Up to 100 μm/s	Up to 100 μm/s	NA	190–4,500 μm/s
References	(137)	(95,138,139)	(99,140–142)	(143–145)	this work (107)

3.9 Trap Stability

The stability of the trapped particle is evaluated by assessing the fluctuations in position along the X- and Y- directions. The trapped particle exhibited a variance of ±0.195 μm and ±0.02 μm around the mean positions along the X- and Y- directions, respectively, as illustrated in Figure 30. The enhanced trapping stability in the Y- and Z- directions compared to the X-direction can be attributed to the symmetrical laser beam profile and the uniform flow characteristics within the channel cross-section, specifically the Y–Z plane. This symmetry results in equivalent trapping accuracies along the Y- and Z-axes.

In contrast, the trapping stability along the X-direction, which aligns with the flow direction, is comparatively lower. This difference stems from fluctuations induced in flow speed due to the mechanical pumps employed in this system. These flow speed variations exert a fluctuating drag force on the trapped particle, consequently affecting its position along the X-axis.

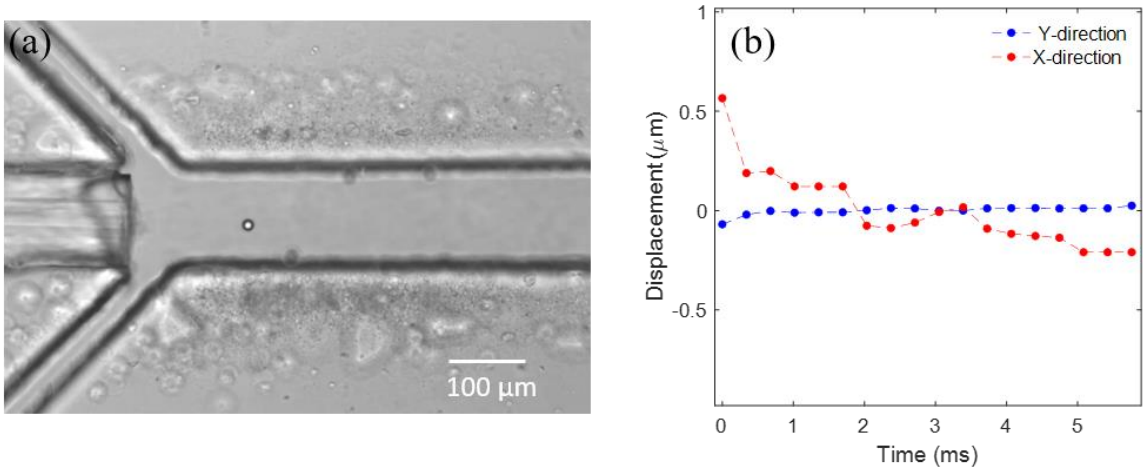

Figure 30: (a) Microscopic image of a 15 µm PS bead trapped in the microchannel using OHT. (b) Fluctuations around the mean position of the trapped bead in the X- and Y- directions. The position corresponds to the centroid coordinates of the particle extracted from individual frames.

Conversely, trapping in the Y- and Z- directions is primarily governed by the gradient force and the net lift forces. These forces are not influenced by flow fluctuations within the channel, which contributes to the enhanced trapping stability in these directions. To improve trapping stability along the X-direction further, the implementation of a glass-based microfluidic device or a pressure-controlled flow system would effectively minimise flow fluctuations within the channel. By mitigating these fluctuations, enhanced trapping stability along the flow direction can be achieved. In summary, OHT demonstrates remarkable robustness and stability for particle trapping.

3.10 Precision of Particle Manipulation in OHT

To evaluate the precision of the system and understand the particle manipulation capabilities of the OHT platform, the trapped PS bead was subjected to varying input laser powers at a constant flow velocity. The trapped particle within OHT can be translated along the length of the channel

in two ways: either by modulating the drag force in the system by altering the input flow rates of the sheath flows or by varying the input laser power of the trapping laser. Both of these methods are robust and can be utilised in combination to influence the quality of the trap. These methods have been discussed in detail in Chapter 4, section 4.6.

The precision in position is validated by varying the optical forces exerted on the trapped particle. This is achieved by switching between two different input laser powers and measuring the position of the trapped particle over time. A custom-written MATLAB code helped extract the exact centroid position of the particle from the different frames of the video sequence. The laser diode was initialised for an input power of 182 mW and 500 mW in consistent intervals. The mean position of the trapped particle was measured for a few iterations to estimate the accuracy of particle manipulation as shown in Figure 31.

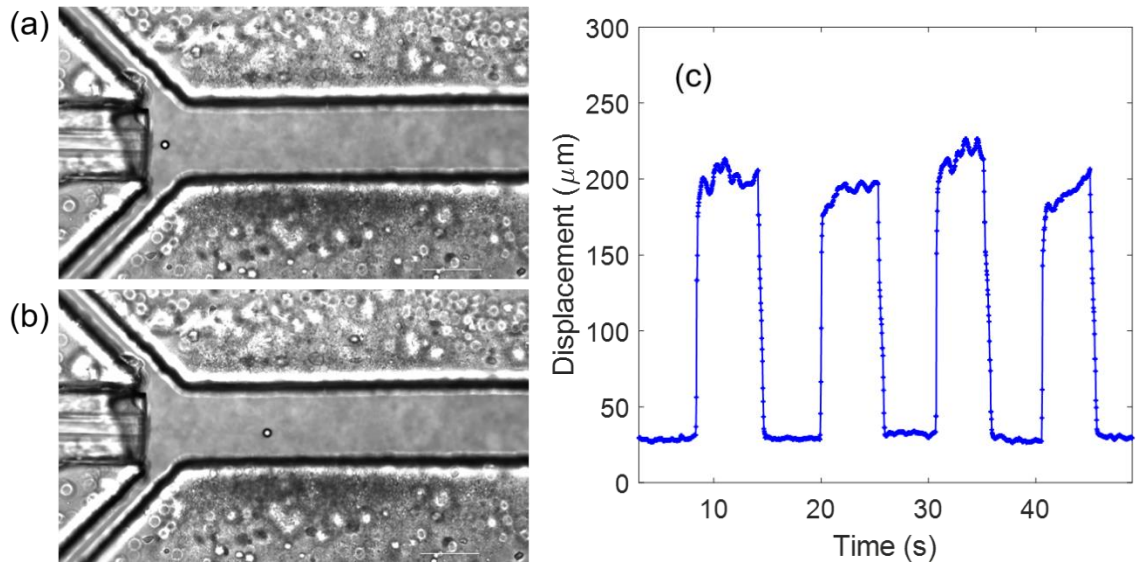

Figure 31: Microscopic image depicting a trapped PS bead of diameter 15 μm at a laser power of (a) 182 mW and (b) 500 mW for a fixed flow velocity. (c) The relative change in the X-position of the particle is measured by manipulating the particle between two positions by modulating the laser powers.

As is evidenced from the graph in Figure 31, the trapped particle oscillated between a distance of 30 μm and 210 μm from the tip of the fiber (Y = 0) for applied input laser powers of 182 mW and 500 mW, respectively, with respect

to time. A particle trapped within OHT can be precisely and accurately translated to different positions along the length of the channel by varying the forces exerted on it. The unique optofluidic synergy minimises laser damage to sensitive cells by translating the particle to farther distances away from the laser at low input laser powers. The long-range translation of the trapped particle provides access to integrate other detection systems along the length of the channel to study single particles.

3.11 Trap Stiffness

Thus far, we have discussed the principles of OHT and understood the capabilities of the system from the perspective of trapping PS particles. Advanced experiments are possible by understanding the relation between the forces and the motion of the trapped particle. To apply optical tweezers in quantitative biology, the stiffness of the trap must be calibrated accurately. By extracting information from the particle time trace, one can quantify the forces acting on the particle, calibrate the system, and even gain information about the surrounding fluids.

The equipartition theorem (146) is one method to evaluate the stiffness or strength of a trap. The theorem states that "a system at thermodynamic equilibrium will have, on an average, ½ k_BT of energy in each degree-of-freedom."

The optical trap stiffness is related to the size of the trapped particle. Depending on the size of the particles and the wavelength of the trapping laser, the maximum optical force exerted on a particle diminishes in inverse proportion to its radius, resulting in a decrease in the maximum force experienced by the particle (Mie regime, particle size greater than λ). On the other hand, when the particle size is much smaller than the wavelength of the trapping laser, the force is proportional to the third power of the particle radius.

For my experiments, I have strictly adhered to the Mie regime, where the particles are much larger compared to the wavelength of the trapping laser. Using the equipartition theorem to evaluate the trap stiffness, for the X- and Y- directions, this can be written mathematically as:

$$k_{x,y} = \frac{k_B T}{< x, y^2 >} \qquad \ldots(43)$$

where, $k_{x,y}$ is the trap stiffness in X- and Y- directions, k_B is the Boltzmann constant, $< x, y^2 >$ is the positional variance of the trapped particle, and T is the absolute temperature.

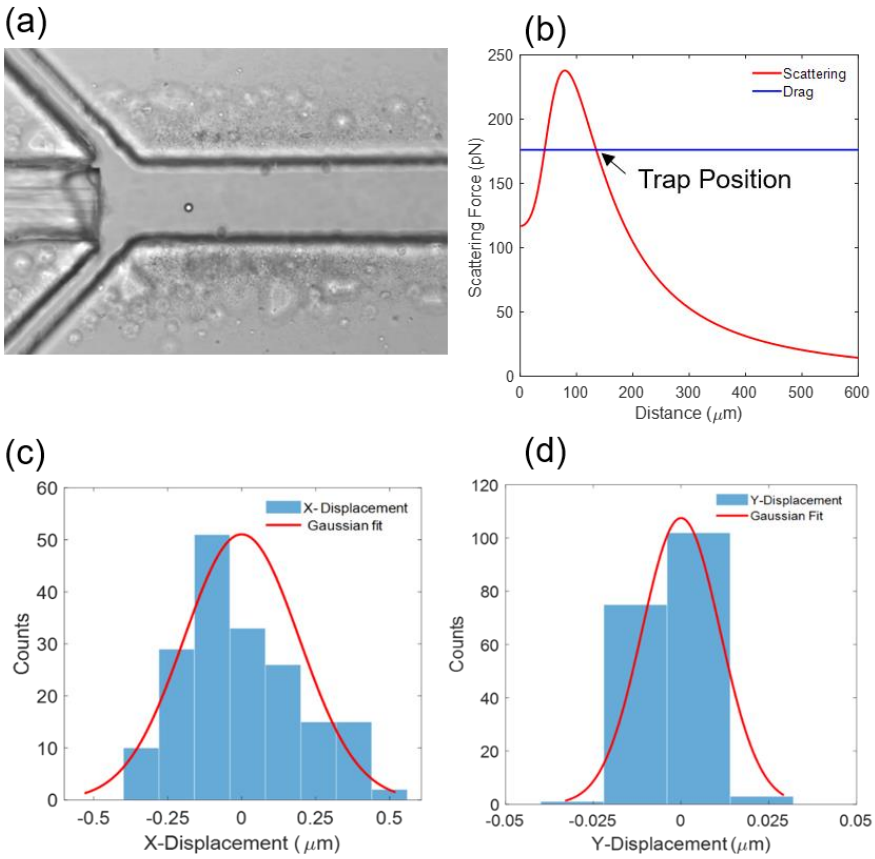

Figure 32: (a) A microscopic image of a single 15 µm PS particle trapped in the microfluidic device using OHT. (b) Theoretically estimated optical scattering and drag forces exerted on a 15 µm PS particle as a function of its position along the length of the microchannel. The tip of the fiber is positioned at X = 0. (c) and (d) represent the positional fluctuations of the particle trapped in OHT in the X- and Y- directions, respectively.

For a particle with a diameter of 15 μm, Figure 32 shows the fluctuations in its mean trapped position. The stiffness in the X- and Y- directions were evaluated to be 0.1 pN/μm and 342 pN/μm, respectively. The trap stiffness in the X-direction—the direction of flow—was found to be three orders of magnitude smaller owing to the fluctuations in the flow profile. This was primarily due to the operation of the mechanical pumps, which were pulsing at regular intervals and adding to the fluctuating drag force on the particle in addition to the thermal fluctuations in the system.

The bead was trapped at a distance of 150 μm from the tip of the fiber. The average flow velocity was estimated at 1,400 μm/s within the channel. Figure 32 (b) shows the maximum scattering force exerted at a distance of 100 μm from the tip of the fiber; it decreases with increasing distance as the laser intensity scales inversely with distance. Assuming a constant flow velocity at a distance of 134 μm, the magnitude of the drag force is equal to the scattering force for an output laser power of 860 mW. This is the expected location of the trap determined from theoretical calculations. This agrees with the distances estimated for the trap location experimentally at 150 μm from the tip of the fiber.

This chapter introduced light–matter interactions and defined the various optical forces responsible. Opto-hydrodynamic tweezer platform and its principle of operation were discussed with details of the fabrication process. The device takes advantage of optical forces and the precision of microfluidics to trap and manipulate single particles. Various experiments to validate and characterise the system were discussed in detail. The quality of the trap and focusing of 15 μm PS particles was assessed. The OHT platform was compared to conventional optical trapping approaches available in the literature. Parameters such as stability, precision, and stiffness of the trap were measured and discussed. The functionality of the OHT device with respect to cells is covered in the next chapters.

Chapter 4

Rollin' in the Deep

4.1 Single-cell Operations Within OHT

The functionalities of a microfluidic chip are limited by the number of components that can be combined with it while still retaining all the advantages of a lab-on-a-chip device. More often than not, the combination of operations on single cells—such as trapping, translation, and sorting—requires bulky components for actuation to achieve functionality. As discussed in Section 1.2, many tools exist for the manipulation of single cells but most of them require the integration of electrodes, high-power amplifiers, or expensive fabrication facilities, making the process challenging and inaccessible especially in a resource-limited setting. In chapter 3, we discussed the fabrication of the OHT device and its various parameters by studying PS particles. Parameters such as precision, trap stability, and trap stiffness were also evaluated. In this chapter, we will discuss the functionality of the OHT device further, with an emphasis on the trapping, translation, and rotation of single cells, along with isolation or sorting of desired cells into designated outlets. Moreover, I will highlight the versatility of the platform with examples of particles of varying sizes and refractive indices trapped within the same device.

4.2 Single-cell Trapping

Trapping within the OHT is initiated by sequentially focusing the sample stream of cells through sheath flows. The sheath flows confine the sample stream to the optical axis of the fiber, at which point the laser is turned on to begin trapping. The concentration of the cell solution and the flow rate ratio of the sheath to sample flow are adjusted to achieve high trapping stability and efficiency, that is, 1 cell/10 seconds. This allows enough time for the investigation of the cell at the trap via microscopy and/or spectroscopy. This may be fine-tuned depending on the aims of the experiment.

In my experiments, THP-1 leukaemic cells were cultured in RPMI 1640, supplemented with 2-mercaptoethanol (0.05 mM) and foetal bovine serum (FBS). The size of these cells ranged between 10 μm–30 μm. The solution was pipetted thoroughly to avoid clumping of cells. Figure 33 demonstrates the trapping of single THP-1 leukaemic cells using OHT.

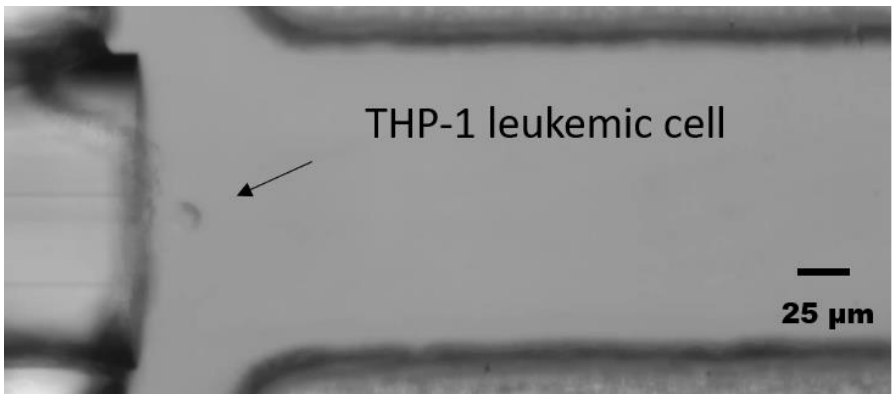

Figure 33: Microscopic image demonstrating the trapping of a single THP-1 leukaemic cell using OHT at an input laser power of 450 mW.

When comparing the trap locations and applied input laser powers, for trapping cells and PS beads, the cells are trapped much closer to the optical fiber. This is attributed to the low refractive index difference of the cell compared to its surrounding fluid. Due to the low contrast in refractive index matching between the cell and the surrounding, the scattering forces required to trap the cell are not enough and, therefore, require more input laser power.

The OHT can function in two modes depending on the end goal of the research application. The first is a continuous "trap-and-release mode", where particles are trapped sequentially, one at a time, to collect information. In this mode, the sample flow can be stopped to acquire information from a single particle or conduct time-lapse studies to understand the dynamics from the perspective of a single cell (147,148). The throughput of the system can be adjusted by changing the initial concentration of the cell solution to maintain a specific frequency of the incoming cells.

The second is the "linear array mode", as shown in Figure 34, wherein the OHT can trap multiple particles forming a chain. This is achieved by applying a high input laser power to sustain the chain of particles. At a laser power of 860 mW, the OHT can trap up to 12 beads in an array. Beyond this number, the optical forces are weak and subsequent particles do not experience the effect of the force after the twelfth particle. This is due to the shielding effect of the particles in the chain. The chain length is dependent on the applied input laser power and flow velocities within the channel. In some cases, these linear arrays of trapped particles are advantageous for studying cell–cell interaction (149) or imaging the sample across an area to acquire information about multiple cells in a single shot.

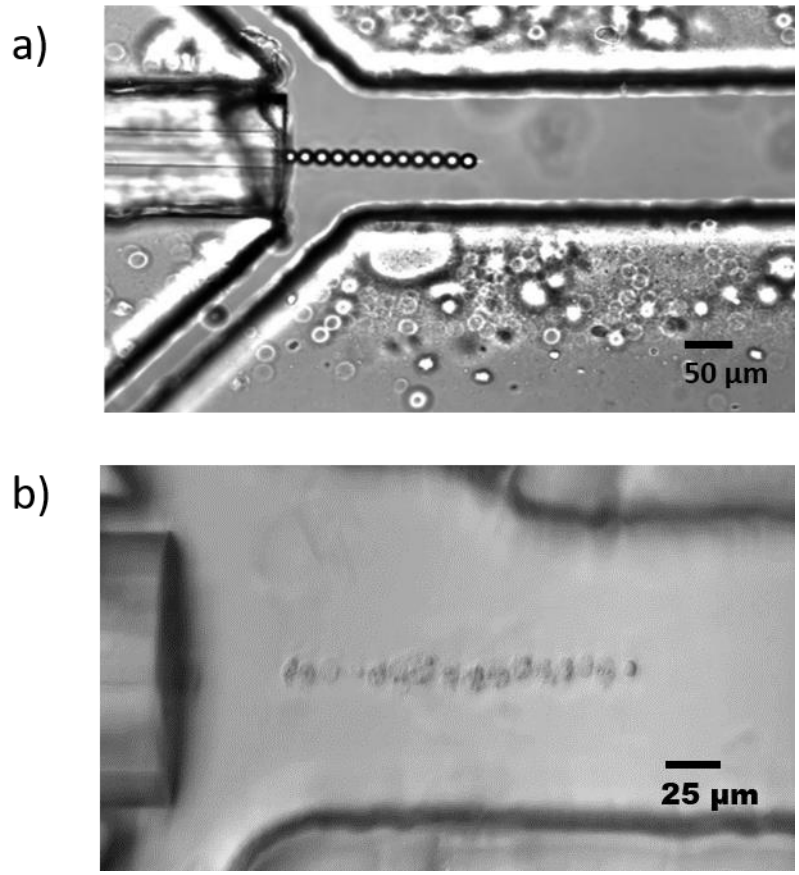

Figure 34: Trapping of (a) PS beads and (b) THP-1 cells in a linear chain array within the OHT.

4.3 Translation of the Trapped Particle in OHT

The trapping of a particle or a cell occurs along the optical axis of the laser. However, the exact position of the trap is dependent on various factors. Within the OHT, the input laser power determines the overall optical forces exerted and the fluid drag within the system is controlled by the applied flow rates via syringe pumps. Apart from the forces, the characteristics of the sample itself—the particle size, refractive index, and the shape of the particle—influence the location of the trap. Consequently, this determines the stiffness of the trap. This control over the trap position and manipulation of the trapped particle over a long range make OHT more appealing compared to traditional fiber tweezers.

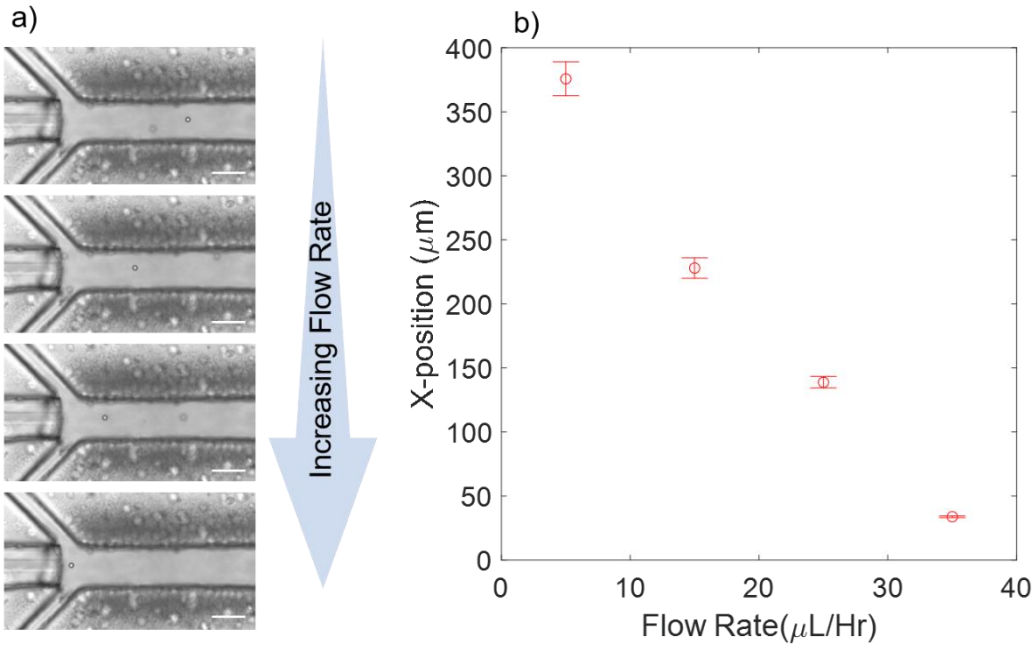

Figure 35: (a) Translation of the trapped particle along the length of the channel while varying the flow rates of the sheath flow. (b) The applied laser power is constant at 860 mW.

To determine the maximum translation range of the trapped particle, the input laser power was fixed, and the subsequent drag force was steadily increased by varying the sheath flow rates. The position of the trapped particle was analysed for varying flow rates as shown in Figure 35. The flow velocity within the microchannel can be controlled via mechanical syringe pumps operated by the user. High-precision, low-pressure syringe pumps by NemeSYS, Cetoni, manufactured in Germany, were used for this study. The sample and sheath fluids were injected from a 1mL–Hamilton glass syringe.

While maintaining the optical output power from the fiber at 860 mW, the trapped particle is subjected to the lowest flow rate that can be achieved by the syringe pump for a given syringe. The pulsation-free flow rate limit for a 1 mL–glass syringe was 2μL/hr. The distance from the fiber end for the given conditions of laser power and applied flow rate was estimated to be 407 μm. The position of the trapped particle was monitored while steadily increasing the flow velocities in the microchannel as shown in Figure 35 (a).

The particle moved closer to the tip of the fiber with an increase in applied flow rate of the sheath flows. This is because a larger scattering force required to compensate for the increasing drag force on the particle. The magnitude of the scattering force scales with distance from the tip of the fiber due to the diverging nature of the laser. With modulation in the flow rates, the maximum distance the trapped particles can translate is 370 μm, with average flow velocities in the microchannel ranging from 270 μm/s–2,100 μm/s.

4.4 Modulating the Laser Power for Particle Manipulation

Alternatively, laser power can also be modulated to manoeuvre the particle trapped within the OHT. To assess the effect of the applied laser power on the trap position, the flow velocity within the microchannel was kept constant and the laser power was varied steadily; the position of the trapped particle was measured simultaneously. The arrangement of the optical fiber opposite to the flow field within OHT allows the manipulation of the trap along the length of the microchannel. To study the effect of optical power modulation, a 15 μm PS particle was initially trapped at a flow velocity of 600 μm/s at a distance of ≈60 μm from the optical fiber. Without changing the flow velocities, the optical power at the output end of the fiber was ramped up from 350 mW to 550 mW in steps of ≈50 mW as shown in Figure 36 (b).

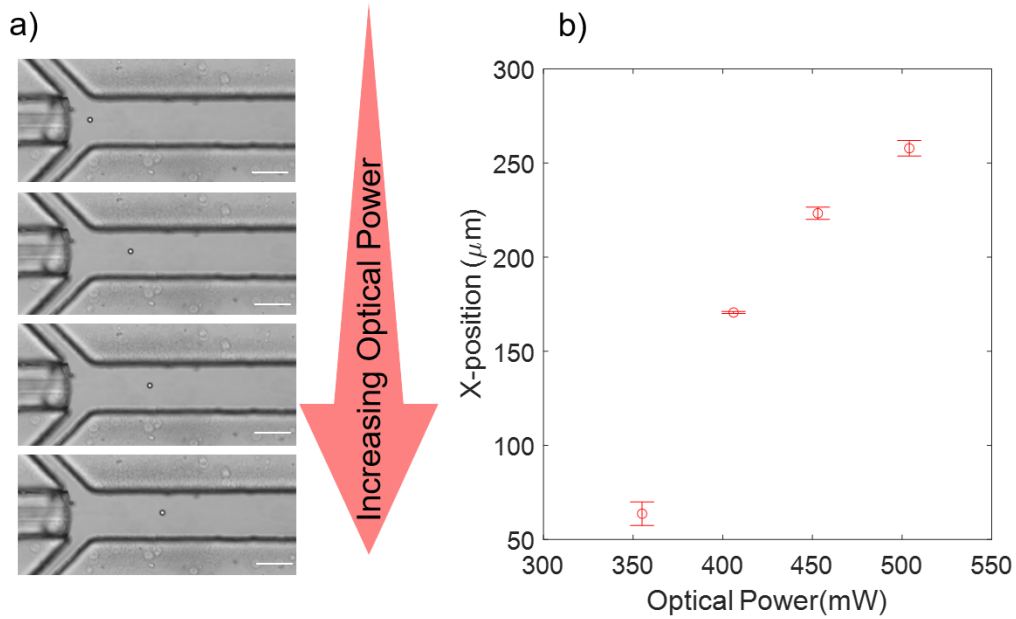

Figure 36: Translation of a trapped 15 µm PS particle while varying the applied laser power at the output end of the fiber and maintaining a constant flow velocity of 600 µm/s in the microchannel.

The trapped particle was manipulated up to distances of 260 µm from the tip of the fiber while varying the laser power from 350 mW to 550 mW. The increase in applied laser power results in an increase in the magnitude of the scattering forces exerted on the trapped particle. This shifts the balance between the optical and fluidic forces, causing the trapped particle to readjust its position and, hence, move away from the tip of the fiber.

The laser diode can be operated at much higher powers to increase the translation range further. The maximal powers are limited to values where the localised heating of the surrounding media and fluids is avoided. Furthermore, the use of very high powers with biological samples for long durations can be damaging and should be avoided.

A heat map based on all possible power and flow combinations was generated for a 15 µm PS particle based on theoretical considerations, and the resulting information is compared to the experimentally obtained values (Figure 37). The trap locations obtained as a measure of the distance of the trapped particle from the tip of the fiber were in agreement with the theory.

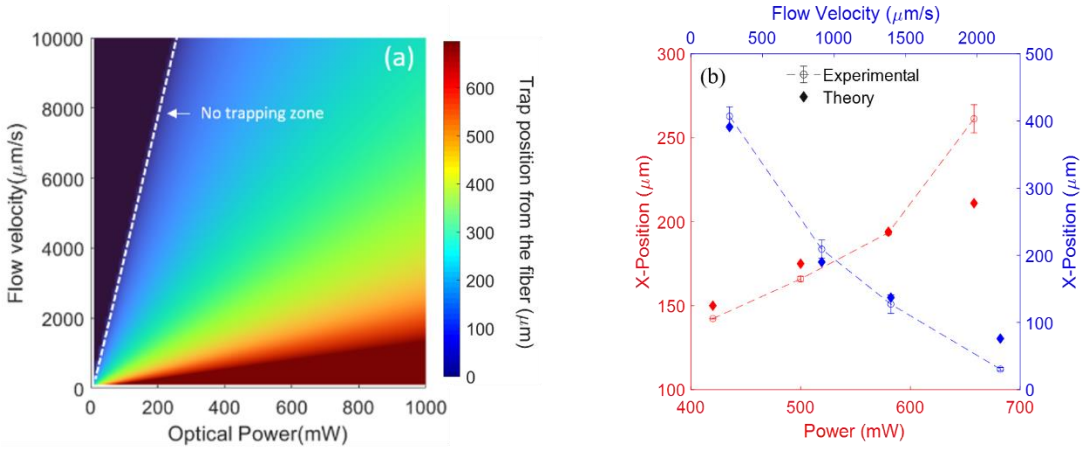

Figure 37: (a) Heat map of the possible trap positions of a 15 µm PS bead trapped in the OHT for a range of optical powers and flow velocities gathered from theoretical calculations and applied in the microchannel. The region to the left of the dashed line corresponds to the no-trapping zone. (b) Graph depicting a comparison of the theoretical predicted trap positions and the corresponding positions for different flow velocities and optical power combinations validated through experiments.

A 15 µm PS bead can be translated to a maximum distance of 500 µm when the OHT is operating at the maximum laser power of 880 mW and at an average flow velocity of 190 µm/s. Beyond this maximum power, bubbles tend to form within the channel due to absorption. The flow velocity minimum was determined by the operation range of the syringe pump below which fluctuations become significantly higher and lead to unstable trapping.

4.5 Rotating Single Cells

The implementation of sheath flows within the OHT allows precise manipulation of flow trajectories within the microchannel. By taking advantage of laminar flows, a torque—arising from the difference in sheath flow ratios on the two sides—can be applied to a trapped particle. This torque causes a rotation in the particle and can be controlled by varying the sheath flow rate ratios on the side. Figure 38 shows how a trapped leukaemic cell is rotated and arbitrary markers (marked as red circles in Figure 38 (c)) are assumed on the cell to quantify the rotation speed.

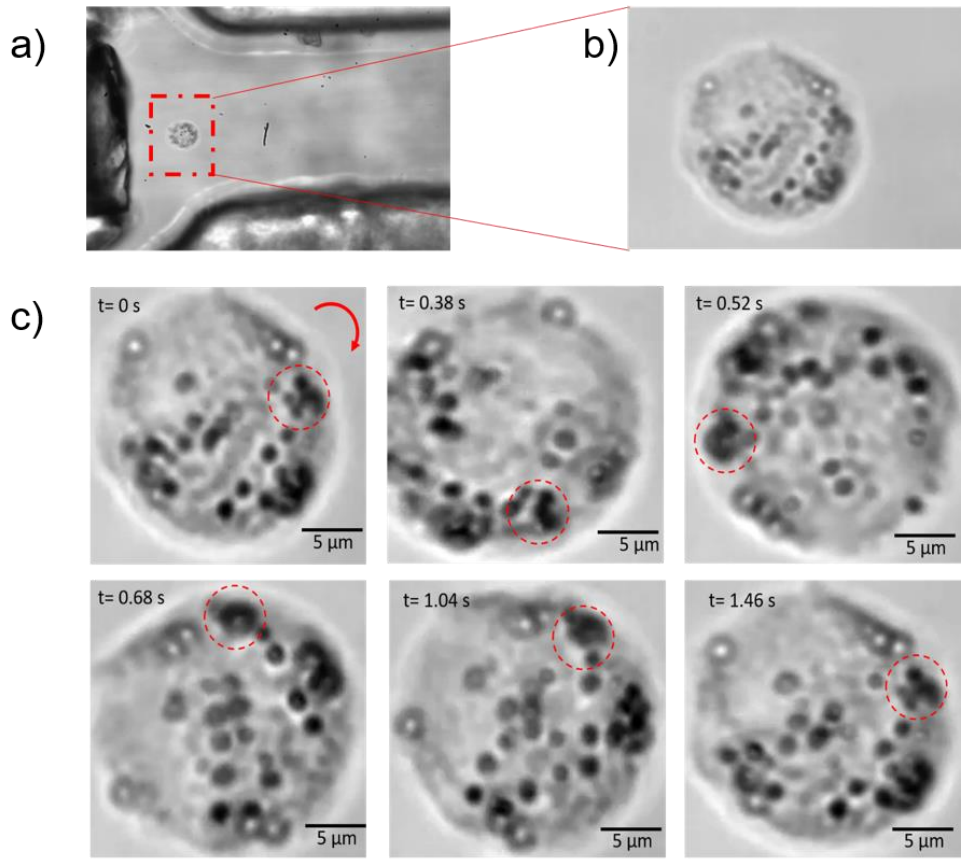

Figure 38: (a) Trapping of a single THP-1 leukaemic cell at the bifurcation region. (b) Magnified image of the cell. (c) Trapped cell rotating due to inhomogeneous flow field distribution in the region.

The trapped cell is rotated at the flow bifurcation junction of the OHT by applying an asymmetric side sheath flow rate. This causes the majority of the flow to be directed to one outlet, as the sheath flow rate of one side is 30 times higher than the other, thereby resulting in the rotation of the cell as shown in Figure 38 (c). The data acquisition parameters were adjusted to obtain high frame rates to quantify the rotation speeds. The trapped cell rotated at about 40 Revolutions per minute (RPM) for an average flow velocity of 250 μm/s in the microchannel.

Evaluating rotation is interesting for research in biological systems, as it enables visualisation of the cell and its constituents in 3D at different angles as compared to confocal microscopy, where the sample is static and the angles of observation are fairly limited (150–152). Imaging has inherent advantages: it retains spatial and temporal information of a single cell. With advances in label-free microscopy techniques far surpassing super-resolution microscopes that usually rely on fluorescent labelling to image structures, it is possible to visualise fast processes in living systems. Junger et al. (153) employed a rotating illumination laser on a sample to obtain super-resolved images based on multiple interferences and image reconstruction. Techniques such as rotating coherent scattering (ROCS) (154,155) can be combined with OHT to study the dynamics within single cells in a flow-cytometric approach while circumventing all the disadvantages of fluorescent labelling. Combining state-of-the-art microscopy techniques with OHT to obtain a 3D image of a rotating cell can bring critical information to light.

4.6 Sorting of Single Cells

Cells are inherently heterogeneous. The response of one cell to applied stress, or external stimulus, differs from that of another. It is, therefore, crucial to develop tools and techniques capable of isolating single cells from the bulk of a population. Once this has been achieved, the single cell can now be subjected to different stimuli to understand its behaviour and response to changing conditions. For example, consider the success of chimeric antigen receptor (CAR) T-cell therapy. In loose terms, the therapy relies on reprogramming the immune cells within a patient to target and attack the cancer. CAR T-cell therapy relies heavily on isolating lymphocytes, which are further sorted to isolate T-cells to engineer them with new receptors. These receptors help T-cells seek out the cancer cells in the patient's body and attack them. Fluorescence-activated cell sorting (FACS)

(156) is the gold standard in biology and is heavily relied on for sorting cells based on fluorescence. Techniques such as magnetic cell sorting (MACS) (157) have also been sought out to further improve the sorting of cells in terms of efficiency, viability, throughput, and purity.

In the OHT device, sorting can be achieved by either integrating another optical fiber perpendicular to the trapping fiber laser or modifying the sheath flow ratios as needed to redirect flow trajectories into the preferred outlet for the collection of desired cells. In the next sections, let us look at how these are realised.

4.6.1 Optical fiber–assisted Sorting

We have already discussed the working principle of the OHT and how it traps particles at desired locations by leveraging the optical forces from the integrated optical fiber and the hydrodynamic drag forces due to laminar flows in the microchannel. The trapped particle can be sorted by integrating another optical fiber, independently operated by a laser diode. This fiber—let us call it a sorting fiber for ease of understanding—is placed perpendicular to the trapping fiber laser and utilises the optical scattering forces to push the particle towards the desired outlet. Once the particle experiences this pushing force from the sorting fiber, it is pushed away and the flows in the main channel direct it into the collection outlet.

Figure 39 shows the device used for the sorting of a single cell trapped in OHT using optical forces. The device is fabricated via conventional photolithography on a 3-inch Si wafer. PDMS, mixed in the ratio of 10:1 prepolymer to curing agent, is poured onto the wafer and the peeled stamp is plasma treated and bonded onto the glass as described in Chapter 3.

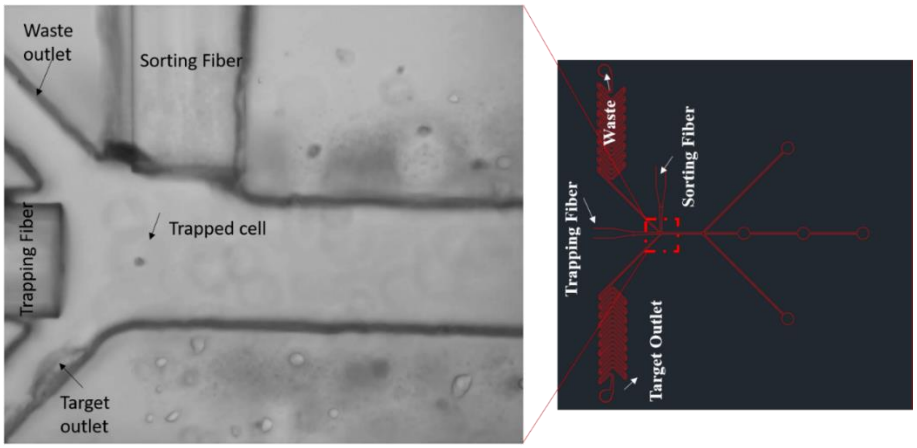

Figure 39: The OHT device integrated with an optical sorting fiber to sort cells.

The sorting process is initiated depending on the information collected when the cell is trapped in OHT. The cell is first trapped by actuating the trapping fiber as shown in Figure 40 (a). Once the necessary information from the cell has been collected, a decision has to be made whether to isolate the cell for further downstream analysis. If the decision is to isolate the cell, then the power of the trapping laser is steadily increased to translate the cell towards the optical axis of the sorting fiber as shown in Figure 40 (b). When the cell reaches the optical axis of the sorting fiber, the sorting fiber is actuated, and the laser is switched on. This exerts a strong scattering force to push the cell in the direction of the preferred outlet for collection.

Note that the sorting fiber is operated at maximum power for a very short duration to minimise photodamage to the cell. At this point, the cell is ejected from the trap and directed by the flow field in the microchannel to the preferred outlet as shown in Figures 40 (c), (d), and (e). In this way, trapped cells can be sorted further and collected downstream within the OHT to conduct other immunohistochemistry or chemosensitivity assays on desired cells individually.

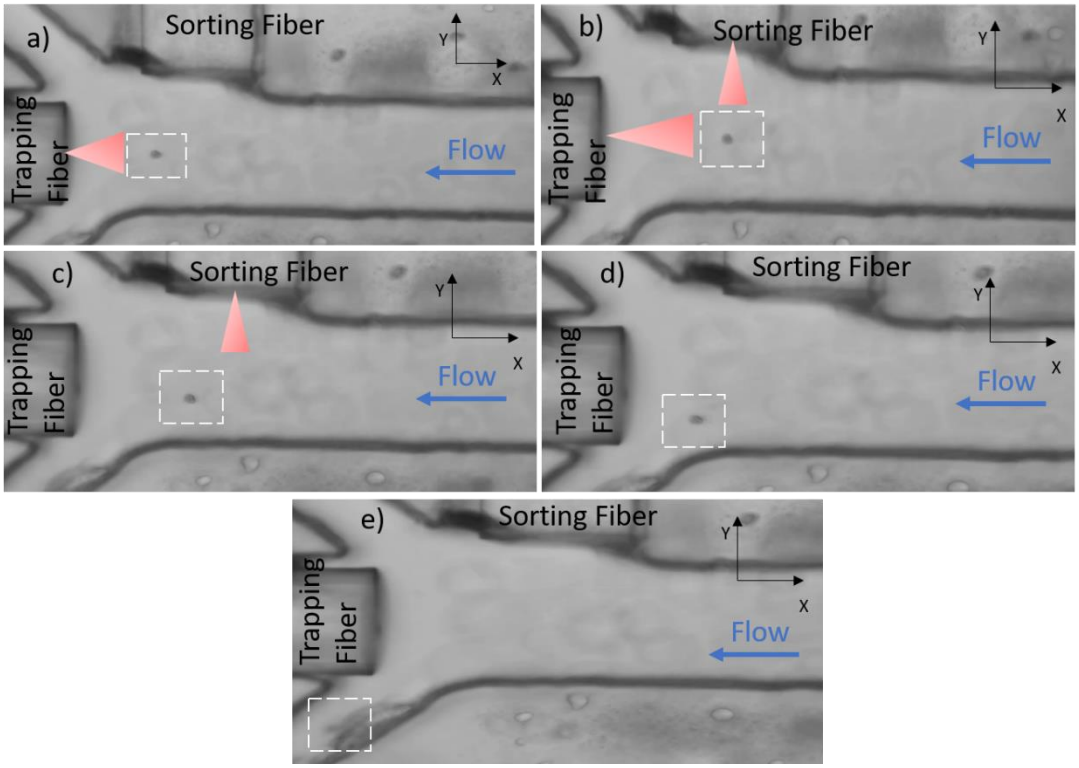

Figure 40: Microscopic images showing the trapping and sorting processes involved in the OHT.

4.6.2 Sheath fluid–assisted Sorting

The OHT device can take advantage of the sheath flows to isolate particles of interest and one does not need to modify device designs or make additions to implement other physical phenomena necessary to assist sorting. This is achieved by increasing the sheath flow rate on one side, for example, either inlet 1 or inlet 2. By only changing the sheath flow rate on one side, most of the fluid flow is directed to one outlet. This increase is typically 60-fold to achieve high purity of isolation, and the trapped particle is released from the trap to be isolated for further investigation. Figure 41 demonstrates the sorting capabilities of the OHT by altering the sheath flow rates on the side.

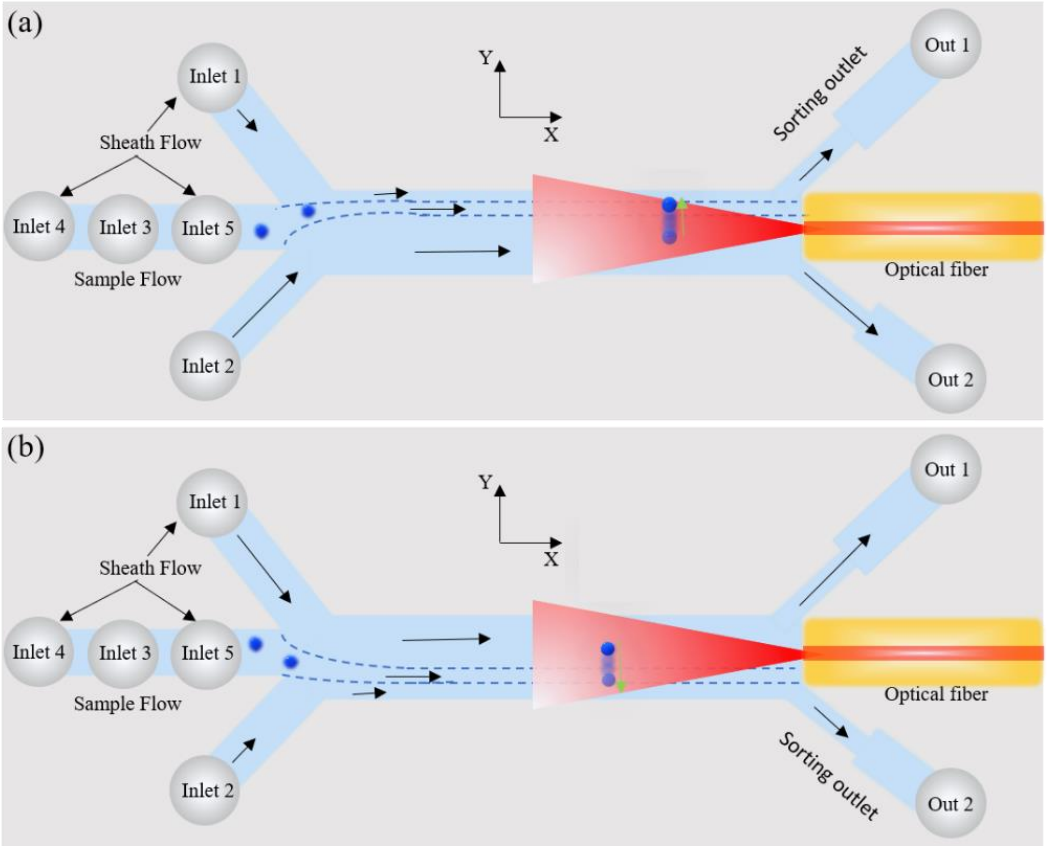

Figure 41: Scheme showing the particle isolation capabilities in the OHT. (a) By increasing the sheath flow inside sheath flow inlet 2, the trapped particle is sorted into outlet 1. (b) An increase in sheath flow from inlet 1 will result in the isolation of the particle towards the outlet 2.

This way, sorting can be achieved on either outlet depending on the needs of the experiment and the overall goal of the study.

4.7 Versatility in Trapping with OHT

The trapping of a particle in the OHT is dependent on its material properties such as its size, shape, and composition (its refractive index contrast compared to the surrounding fluid). It is only possible to trap particles provided the scattering forces exerted on the particle are sufficient to overcome the drag forces in the system. To demonstrate the versatility of the system, particles with different sizes, shapes, and refractive indices were trapped in the OHT. Figure 42 shows the trapping of PS beads of 5 μm and

15 µm (Figures 42 (a) and (b), respectively). Figures 42 (c) and (d) are optical micrographs of THP-1 leukaemic cells trapped in the OHT. The heterogeneity in size can be observed here, where one cell is 10 µm while the other is almost 30 µm. Yeast cells of size 5 µm, as shown in Figures 42 (e) and (f), can also be trapped.

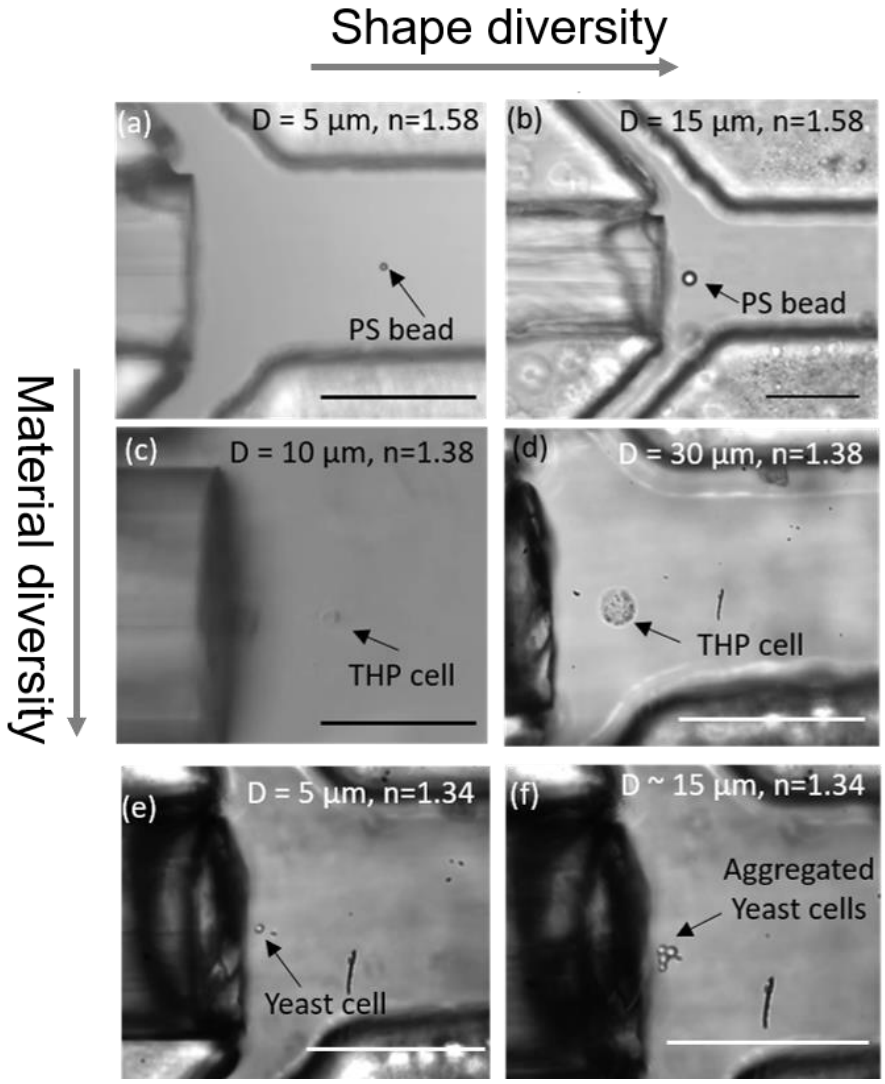

Figure 42: Trapping versatility in the OHT device. Various particles of different sizes, shapes, and compositions can be trapped. Scale corresponds to 100 µm.

Particles with very low contrast in refractive index to that of the surrounding fluid can also be trapped in the OHT as shown in Figures 42 (e) and (f). The refractive index of water is 1.33 and that of yeast cells is 1.34. Within the OHT, particle sizes ranging from 5 μm up to 50 μm can be trapped efficiently. Beyond the size of 50 μm, the output channels tend to clog due to the aggregation of cells. For cell sizes larger than 50 μm, the retrieval of desired cells after interrogation also becomes cumbersome.

On the lower end, the OHT was able to trap PS particles as small as 1 μm, due to the excellent refractive index contrast, for short durations. However, the stability over long time scales proved to be challenging. This can be attributed to the insufficient scattering forces when the size of the particles becomes comparable to the wavelength of the trapping laser. Since the Rayleigh regime applies to particles much smaller than the wavelength and the ray optics regime describes the behaviours of particles much larger than the wavelength of the trapping laser, both these models fail when the size of the particle becomes comparable to the wavelength of the laser.[2]

In this chapter, I detailed the various single-cell operations such as trapping, translation, rotation, and sorting. The OHT platform can conduct trapping in two modes: the continuous trap-and-release mode, where single cells are trapped, subjected to investigation, and sorted based on the needs of the experiment, and the linear array mode, where long chains of single cells can be trapped for a single shot image acquisition thus improving the throughput of the system. The cells can be translated along the length of the channel up to distances of 500 μm from the tip of the fiber by modulating the applied laser power and/or overall flow rates in the system. Moreover, the trapped cells can be rotated, and by combining novel microscopy techniques with the microfluidic platform, 3D spatial information of the cells and its constituents can be acquired. Cells of interest can be sorted within the OHT device owing

[2] There exists another trapping regime apart from these two. Since most of the experiments and studies concerned with the thesis focused on particles much larger than the wavelength of the laser, this regime was not applicable here. For more information, the reader is directed to references describing the generalised Lorenz-Mie theory GLMT (158,159), which bridges the gaps between the Rayleigh and the Mie regimes.

to integration of an additional optical fiber or by manipulating the sheath flow rates. This chapter also highlights the versatility of the OHT device with trapping examples of yeasts, mammalian cells, and inorganic micron particles of various sizes. The next chapter will look at how the microfluidic device is combined with a state-of-the-art microscopy technique to obtain information about trapped single cells and the potential of the device in cancer diagnostics.

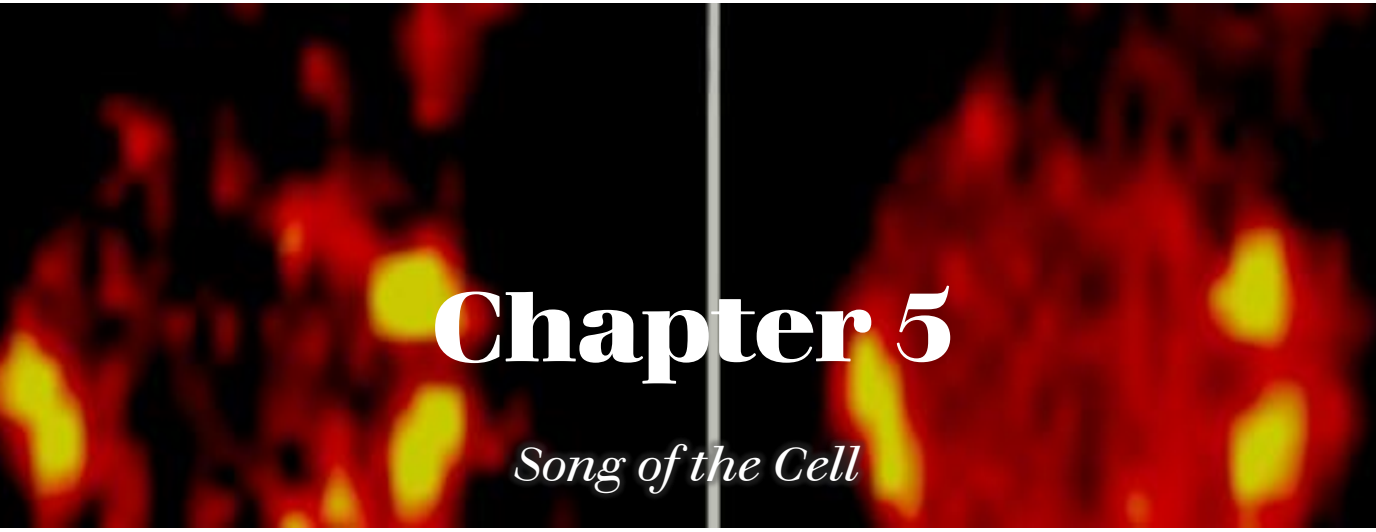

Chapter 5

Song of the Cell

5.1 Human Blood

Human blood constitutes about 7% of the human body weight and is responsible for the exchange of gases and essential nutrients required to sustain life. Blood has several components that can be broadly divided into erythrocytes or red blood cells (RBCs), leukocytes or white blood cells (WBCs), thrombocytes or blood platelets, and plasma (Figure 43). The functions of these different cells are unique: the RBCs are responsible for oxygen delivery and transportation; the WBCs drive the immune system, fighting off infections and protecting the body; and the platelets help with repair and participate in clotting. The typical sizes of blood vessels through which blood flows within the body can range from 5 μm in small capillaries to around 30 mm in diameter for the aorta or the vena cava.

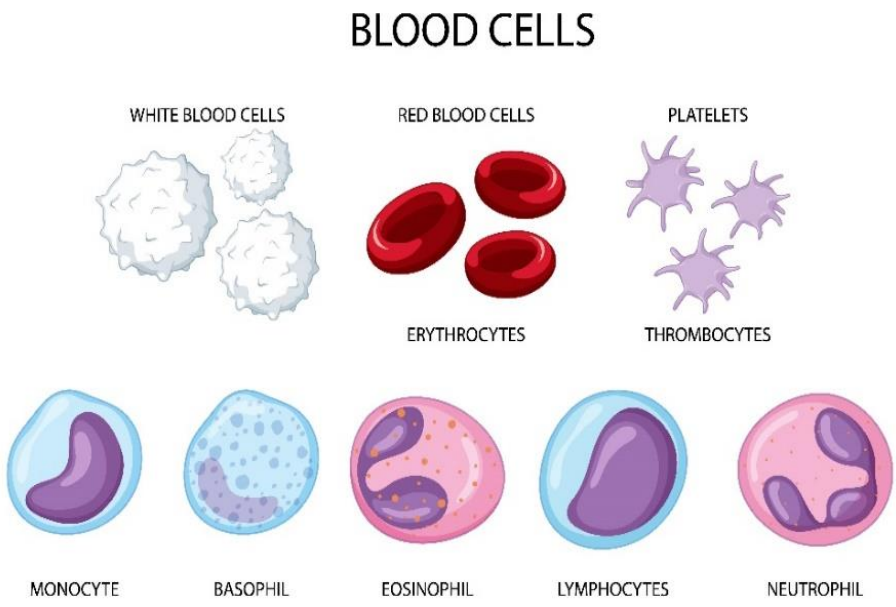

Figure 43: Types of human blood cells.[3]

Leukaemia describes the abundance of white blood cells observed in the bloodstream of an afflicted individual. The word is derived from the Greek words “leukos”, meaning “white”, and “haima”, meaning “blood”. This umbrella term encompasses a diverse spectrum of blood cancers that are classified based on their morphology, immune phenotype, genetic alterations, and clinical characteristics (160). Leukaemia can be broadly categorised into acute and chronic forms, each having distinct clinical presentations. Acute leukaemia manifests when immature WBCs—known as blasts—multiply abnormally; chronic leukaemia arises from these WBCs. Leukocytes can originate from lymphoid lineage (T- and B- cells) or myeloid lineage (neutrophils, basophils, eosinophils, and monocytes). Consequently, the four groups into which medical experts classify leukaemia are: 1) acute lymphoid, 2) chronic lymphoid, 3) acute myeloid, and 4) chronic myeloid leukaemia.

[3] Image by brgfx on Freepik.

5.2 Current Diagnostic Regime for Leukaemia Treatment

Prompt recognition of abnormal blood count patterns is pivotal in initiating timely diagnostic procedures. A hallmark feature of leukaemia is leucocytosis, often accompanied by one or more cytopenias.[4] Notably, the degree of leucocytosis is not a reliable indicator of disease aggressiveness. Some aggressive types of leukaemia may present with a modest increase in white cell count, while certain indolent forms are often characterised by significant leucocytosis. Conversely, the absence of leucocytosis does not rule out a leukaemia diagnosis. These "aleukaemic" leukaemia exhibit a normal or low white cell count but frequently manifest with cytopenias (161).

Let us consider a hypothetical scenario where a person presents with symptoms suggestive of leukaemia. The general practitioner (GP) initiates the diagnostic process by ordering a battery of assessment tests (162–165).

Day 1: Clinical assessment

Typically, on day 1, the doctor begins with a comprehensive medical history and performs some physical examinations, noting down symptoms, if any, of fatigue and weight loss and signs of abnormal bleeding or bruising.

Day 2: Complete blood count (CBC)

On day 2, a CBC is ordered to assess the patient's blood cell counts.

Day 3: Peripheral blood smear

On day 3, depending on the results of the CBC, if the patient presents with an abnormal WBC count, a peripheral blood smear is performed to examine the blood cells under a microscope. This helps to identify any abnormal or immature cells, providing additional clues. The results usually are compiled in a day or two.

[4] Cytopenia refers to a decrease in the number of one or more types of mature blood cells.

Days 5–7: Bone marrow biopsy

If the blood smear reveals abnormalities, the next step is a bone marrow biopsy. This usually involves extracting a small sample of bone marrow from the hip bone. The results take from a few days to a week and provide information on the type and subtype of leukaemia, as well as any genetic abnormalities.

Days 10–14: Cytogenetic analysis

Building on the results from the bone marrow biopsy, a chromosomal analysis of the leukaemic cells is conducted to identify structural abnormalities. This aids in the classification and prognosis. The results typically take around one to two weeks.

Days 12–16: Immunophenotyping (166,167)

Flow cytometry is used to analyse surface markers on leukaemia cells, helping to determine the specific type of leukaemia. This test usually takes a few days and is especially tricky when the sample needs to be extracted from minor patients.

Days 18–21: Imaging studies

If the above tests confirm leukaemia, imaging studies such as CT scans or MRI may be performed to further assess the extent of organ involvement and lymph node enlargement. These results might be available within a week.

After about a month of tests, a definitive diagnosis is made, and the doctor is then able to discuss treatment options with the patient. The treatment varies based on the type, subtype, and stage of the disease. Most common treatment modalities including chemotherapy, targeted therapy, immunotherapy (168), and, in some cases, even stem cell transplantation are not tailored/ personalised to the specific patient's cells. Depending on the urgency of the situation, the time frame is decided. Most acute forms of leukaemia require prompt intervention while chronic forms may allow a more gradual treatment approach.

5.3 Raman Microfluidics

As evidenced by the example in Section 5.2, it takes about one month to arrive at a definitive diagnosis from the moment the individual visits the doctor. The current treatment modalities do not consider chemoresistance, the tests are not selective for the subtypes or coexisting subtypes of leukaemia, and the treatment is more generalised, making relapses and further treatment more challenging.

The work presented in this thesis carries in it the hope of cutting down this diagnosis time to as short as possible by providing critical information, which is chemically sensitive and reliable for the clinician but would normally take a month of tests to come forth. The ability to utilise as little sample as possible while providing fingerprint information of individual cells can be life-altering, especially in the diagnosis and understanding of leukaemia and its subtypes.

In this section, I will discuss some examples available in the literature that employ Raman spectroscopy (RS) in tandem with microfluidics as well as some of the results I obtained using the OHT device integrated with a stimulated Raman microscope to study and image leukaemic cells.

Since the 1970s, RS has been successfully applied to the study of whole blood and its components by analysing its morphological and molecular features using imaging. Granulocyte—a type of leukocyte with granules inside the cytoplasm (neutrophils, eosinophils, and basophils)—can be easily distinguished by analysing the Raman bands of characteristic proteins—myeloperoxidase (MPO) and eosinophil peroxidase (EPO)—as well as their nuclei and lipid distribution (169). Similarly, agranulocytes are identified based on their carotenoid, haemoprotein, and lipid composition through chemometric analysis.

Although RS offers advantages such as the collection of full spectral information and the inherent confocality in microscopes allowing segmentation, it has some disadvantages. The measurements for a single cell are slow, typically requiring a few minutes to integrate, and average over the signal. SRS emerged as a rapid technique to image single cells within a few seconds and provide specific information with high sensitivity, in addition to having the capability to monitor single-cell dynamics (170,171). The combination of SRS with microfluidics opens up the potential to study single cells in well-controlled environments.

The unique ability to manipulate single cells on demand extends the functionality of microfluidics beyond conventional flow cytometers. Certain constraints must be met to integrate the SRS system with microfluidics to successfully acquire Raman maps of leukaemic cells. Any vibration or fluctuations during measurements of the sample affect the signal quality and signal-to-noise (SNR) ratio. Therefore, the system must be stable and free from unnecessary fluctuations. The materials employed in the fabrication of the microfluidic device must not interfere with the signals of the sample during Raman measurements. The acquisition parameters must be standardised to compare measurements of different cell lines. Since leukaemia cells are suspension type, it is ideal to mimic similar flow conditions in the microfluidic device as in the flow of blood cells in veins and arteries. This presents microfluidics with the challenge of delivering single cells accurately to the Raman window for signal acquisition. Moreover, during signal acquisition, the cell must be stable with minimal or no fluctuation.

Suzuki et al. (172) demonstrated the potential for acquiring line scans of individual cells, flowing at a velocity of 2 cm/s, through Raman imaging. Nitta et al. (173) established the capacity to dynamically sort cell subtypes based on their morphological features in real-time. Furthermore, Jackson et al. (174) published findings on a microfluidic assay designed for the real-time detection of minimal residual diseases, specifically in isolating circulating leukaemic cells in patients who have undergone a stem cell transplantation.

SRS is a powerful analytical tool and is usually combined with microscopy to image biological samples. To facilitate stable image acquisition and obtain ample signal (upon averaging and improving signal quality), it is necessary to immobilise the cell at the Raman window. There are various methods to immobilise cells including physical methods such as microarrays, pillars, wells, or chemically fixing them. However, these methods affect the physical or chemical properties of the surface of the cell. In this chapter, we will explore optical tweezers—a non-contact force to immobilise single cells—and study them using Raman microscopy. Optical tweezers have various advantages such as fast, sequential signal acquisition and elimination of the requirement of cell labelling (as in fluorescent microscopy).

Ever since Ashkin's disruptive findings, the interest in combining optical trapping with state-of-the-art microscopy and spectroscopy techniques has grown exponentially. The manipulation of microparticles and precise measurement of the forces acting on them have found several applications in

understanding the dynamics of biological macromolecules, interactions between cells, and in measurement of deformation in cells. Raman spectroscopy has been combined with optical tweezers for over a decade, which has helped advance research in single-cell studies (175). The spectra obtained are a chemical fingerprint unique to the sample and consist of rich information on the proteins, lipids, nucleic acids, DNA content, etc., of the cell (176). The system consists of an optical tweezer system—which facilitates the trapping of single cells—and a Raman imaging system—to acquire the spectra of the trapped cell.

Jess et al. (95) reported a dual beam fiber trap for the analysis of HL-60 human leukaemic cells using Raman spectroscopy in a flow cytometric approach at flow rates of 1.2 nL/s. Although the potential of the technique was demonstrated well, the spectra-acquisition time was almost 60 seconds, and the throughput was fairly limited due to the low operational flow rates. Volpe et al. (176) analysed the spatial distribution of forward-scattered light from a single trapped yeast cell, *Saccharomyces cerevisiae*, in its growth period by combining optical tweezers with a high-resolution force microscope. By analysing the scattered light during the cell cycle of the yeast, they could probe the different physiological states and thus emphasised on comparing spectroscopic data with respect to time only after ensuring the stable trapping of single cells. Ajito et al. (177) studied single-cellular organelles in neurons known as synaptosomes—which are about 500 nm–700 nm in diameter—using a near-infrared laser Raman trapping system (NIR-LRT). They identified strong Raman peaks for lipids and proteins, thereby demonstrating the power of laser trapping with spectroscopy.

Recently, researchers have applied Raman spectroscopy to sort cells within microfluidic platforms (173,178–183). Since Raman spectroscopy requires longer acquisition times owing to the restricted cross-section as compared to fluorescent microscopy, it is necessary to immobilise the cells at the Raman window to acquire ample signal (184,185).

5.4 SRS of Trapped Cells

Cancerous cells exhibit an upregulation in lipid synthesis (186)—a phenomenon attributed to the critical role of lipids in facilitating rapid proliferation, migration, and survival (187). In my experiments, I explored the possibility of employing Raman imaging to distinguish trapped leukaemic cells based on their lipid content. Healthy peripheral blood mononuclear cells (PBMCs) and Philadelphia chromosome (Ph1)-positive cells TOM-1 cells—were chosen to demonstrate the potential of the system as a rapid diagnostic tool for leukaemia. Cell lines exhibiting a distinct molecular subtype—namely, BCR-ABL1 (Ph1)-positive—are of special interest due to their notably unfavourable prognosis when assessed through conventional methods (188,189).

5.4.1 Sample Preparation

PBMCs were collected from healthy donors at the Institute of Hematology and Blood Transfusion in Warsaw and isolated through density gradient centrifugation with Histopaque®-1077 (Sigma). In instances of RBC contamination, erythrocyte lysis was conducted using a 1x BD Pharm Lyse™ lysing solution (BD Biosciences, San Jose, California), followed by two phosphate-buffered saline washes (PBS; 300 x *g*, 5 minutes each). For Raman analysis, cells were fixed with 0.5% glutaraldehyde for 10 minutes at room temperature and washed thrice with PBS (without Ca^{2+} and Mg^{2+}). Subsequently, the cells, PBMCs (including lymphocytes and monocytes), were resuspended in a saline buffer and stored at 4°C until Raman measurements were conducted.

TOM-1 cells were obtained from the Medical University in Lodz and cultured in an RPMI 1640 with 20% FBS. After seeding, the cells were incubated for 24 hours with fatty acids, saturated palmitic acid (PA, Sigma Aldrich), and unsaturated oleic acid (OA, Sigma Aldrich) at a concentration of 100 μM. Before being added to the cells, the fatty acids were saponified (NaOH, Sigma Aldrich) and conjugated with bovine serum albumin (BSA–free fatty acids), Sigma Aldrich) to facilitate their uptake. Control cells were analogously incubated with BSA. After incubation, cells were collected, centrifuged (400g, 5 min), and washed twice with the PBS buffer. The survival rate was determined using trypan blue staining. The cells were then fixed with 0.5% glutaraldehyde for 10 minutes at room temperature and washed thrice with PBS (without Ca^{2+} and Mg^{2+}).

5.4.2 SRS Acquisition Parameters

The experiments were conducted with specific acquisition parameters to ensure accurate and detailed data. The RoI selected for imaging was set at 60 × 30 µm, providing a focused area for analysis as well as minimising imaging time. The pixel dwell time of the laser was maintained at 300 µs. This reduced the overall time of acquisition to 5–7 seconds per image for a single wavenumber. Wavenumbers measured during the experiments included 3,015 cm^{-1}, 2,930 cm^{-1}, and 2,850 cm^{-1}, capturing crucial spectral information about the lipids, proteins, and unsaturation in the cells. The power of the pump beam applied to the sample was maintained at 12 mW, while the Stokes beam power was set at 24 mW. The corresponding Raman loss was measured carefully and has been represented in the colour scale for the respective wavenumbers interpretation in the figures applicable below.

5.4.3 Raman Imaging of Trapped Cells

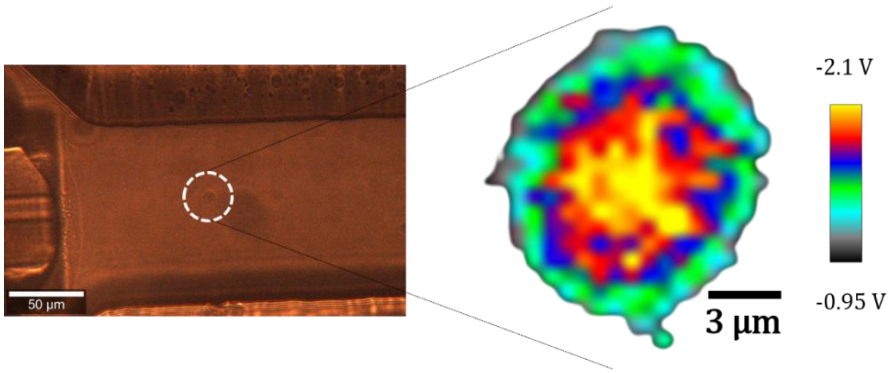

Figure 44: Spatial distribution of the proteins of a trapped cell obtained by stimulated Raman imaging at 2,940 cm^{-1}. The intensity of the SRS signal is depicted on the colour scale (190).

The trapping was initiated by introducing PBMCs into the device via the sample inlet and subsequently focusing them with the help of sheath flows. The cells were sheathed using 3D hydrodynamic focusing and delivered to the optical focus of the fiber within the microchannel. When the alignment was optimum, the cells were trapped by switching the laser on at 300 mW

power. Once trapped, the cell was ready for Raman imaging as seen in Figure 44.

5.4.4 Raman Images of TOM-1 Cells Incubated in BSA, PA, and OA

The lipid content in WBCs can vary considerably in comparison to leukaemic cells. Changes or alterations in the lipid metabolism pathway are directly linked to pathological conditions such as leukaemia (191–194). To track the lipid content in cells, TOM-1 cells were incubated with PA and OA. The Raman maps for these cells were compared with the control sample, which is, TOM-1 cells incubated in BSA. The cells were introduced into the microfluidic device via the sample inlet, focused with the help of 3D hydrodynamic focusing, and trapped within the microchannel. At this step, three different wavenumbers were chosen to obtain Raman images of the composition of lipids, proteins, and unsaturation within the cells at 2,850 cm^{-1}, 2,930 cm^{-1}, and 3,015 cm^{-1}, respectively.

TOM-1 cells incubated in BSA

TOM-1 cells incubated in BSA are imaged in Figure 45. The bright spots on the image show the distribution of lipids and proteins mapped at 2,850 cm^{-1} and 2,930 cm^{-1}, respectively. At 2,850 cm^{-1}, the composition of lipids within the cell has been imaged using stimulated Raman imaging. The distribution of proteins is mapped out at 2,930 cm^{-1} and from these two images, the morphology of the cell can be deduced. To further differentiate the lipid content, a higher wavenumber (3,015 cm^{-1}) was chosen to understand the composition of unsaturated lipids within the cell. By comparing the images of the cells from 2,850 cm^{-1} and 3,015 cm^{-1}, it can be concluded that there is some unsaturation in the cells. This information may be crucial and can act as a marker for determining malignancy in cells.

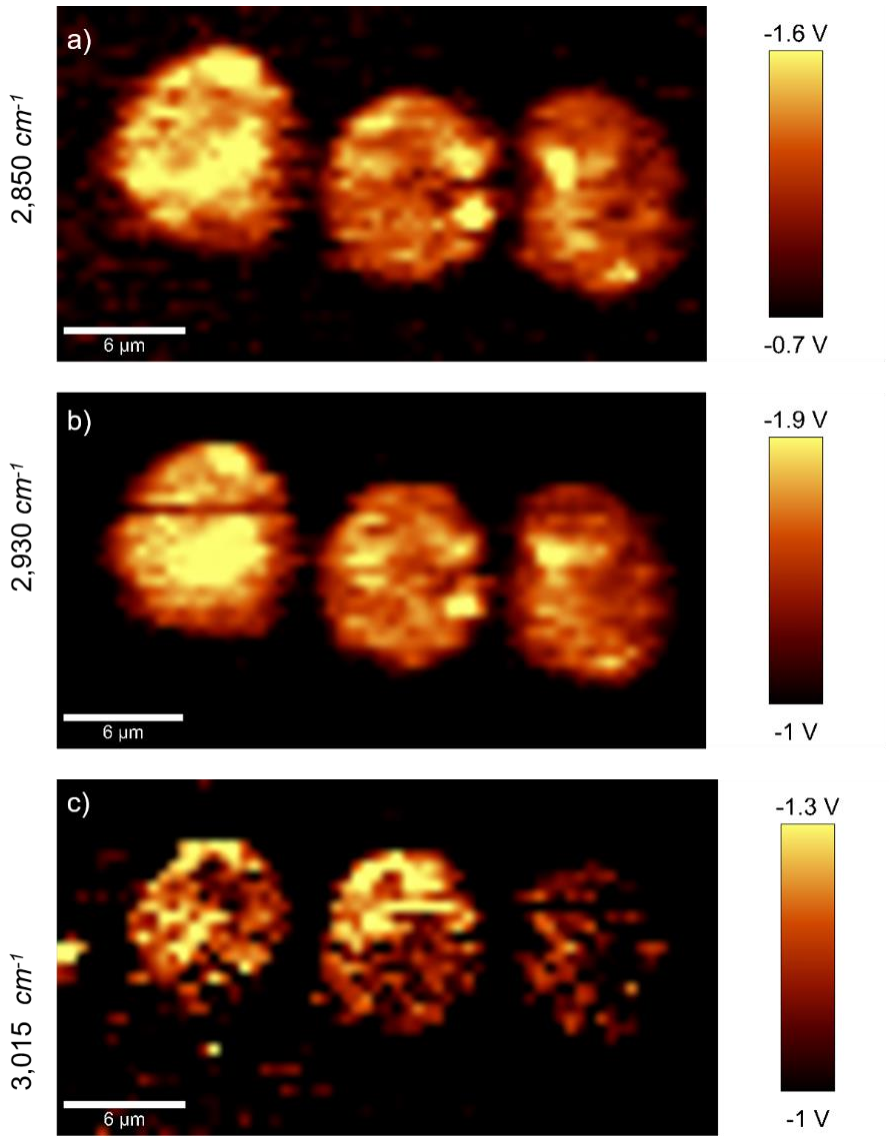

Figure 45: TOM-1 cells incubated in BSA imaged at (a) 2,850 cm^{-1}, (b) 2,930 cm^{-1}, and (c) 3,015 cm^{-1} showing the spatial distribution for lipids, proteins, and unsaturation in lipids, respectively. The colour scale represents the stimulated Raman signal. Scale bars corresponding to 6 µm.

TOM-1 cells incubated in PA

Similar to the previous step, the microfluidic device was thoroughly flushed with PBS and a new suspension of TOM-1 cells incubated in PA was introduced. The goal was to compare the difference in lipid content against TOM-1 cells incubated in BSA based on the uptake of fatty acids due to incubation. From Figure 46, it is evident from the aggregation of bright lipid droplets at 2,850 cm^{-1} that the fatty acid uptake was successful. The aggregation of the lipid droplets is more concentrated as compared to that of images from TOM-1 cells incubated in BSA, wherein the lipid content is more evenly distributed through the volume of the cell. The difference in images for Figures 46 (a) and (b) arises from the rotational effect due to the flows in the system. Owing to the large size of the cell, the cells tend to rotate at lower laser trapping powers of 300 mW.

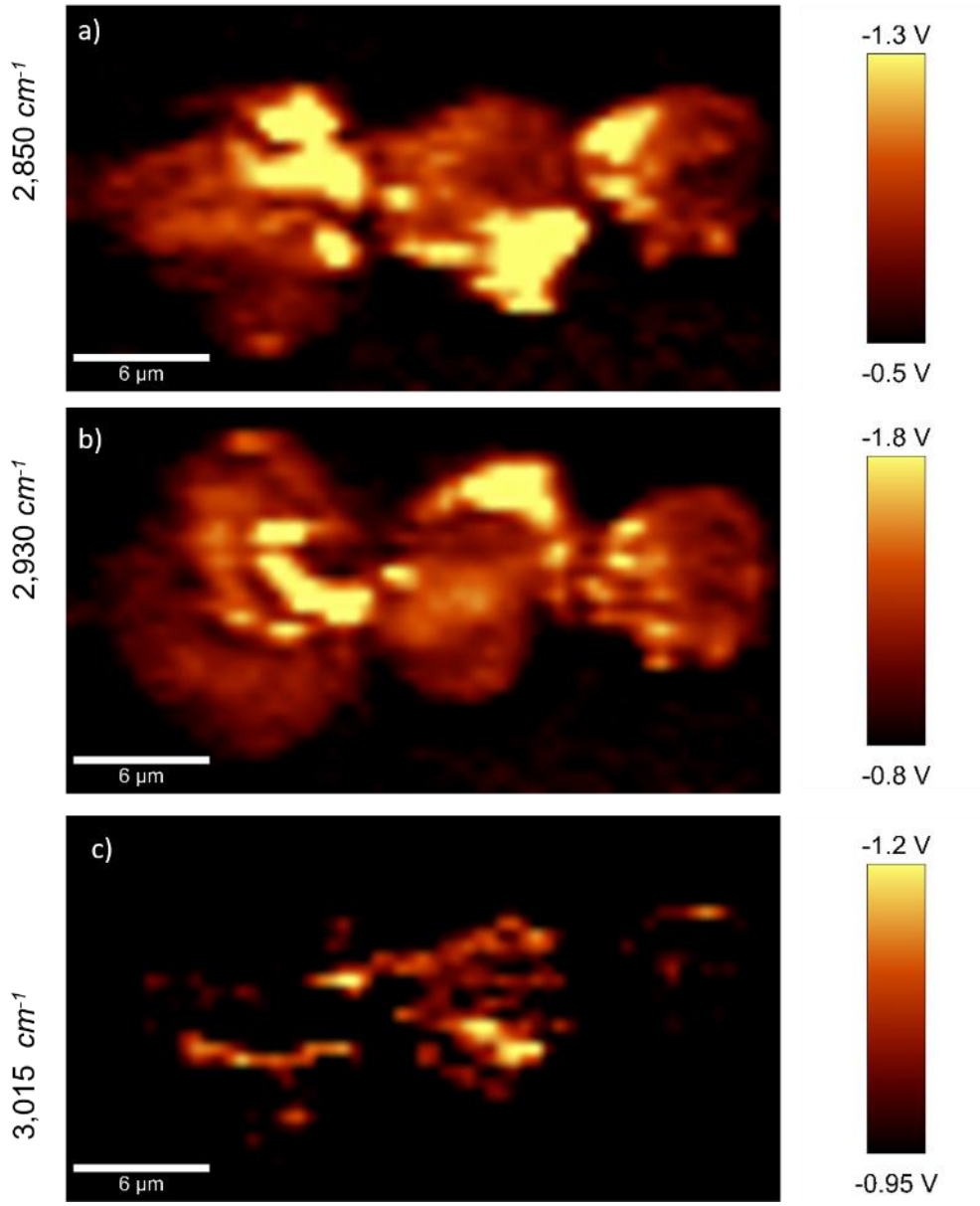

Figure 46: TOM-1 cells incubated in PA at (a) 2,850 cm^{-1}, (b) 2,930 cm^{-1}, and (c) 3,015 cm^{-1}, respectively. Scale bars corresponding to 6 µm.

TOM-1 cells incubated in OA

The bright parts in the cell images for Figures 47 and 48 correspond to the lipid compositions in the single cells at the respective wavenumbers. The lipid droplets could be easily distinguished based on these images confirming the uptake of fatty acids due to the incubation. The protein composition in the cytoplasm of the cell is visible clearly in Figures 47 (b) and 48 (b). The abnormality in morphology is also an important factor to consider when studying cancer cells, and imaging makes it possible to deduce information about the shape of the cell.

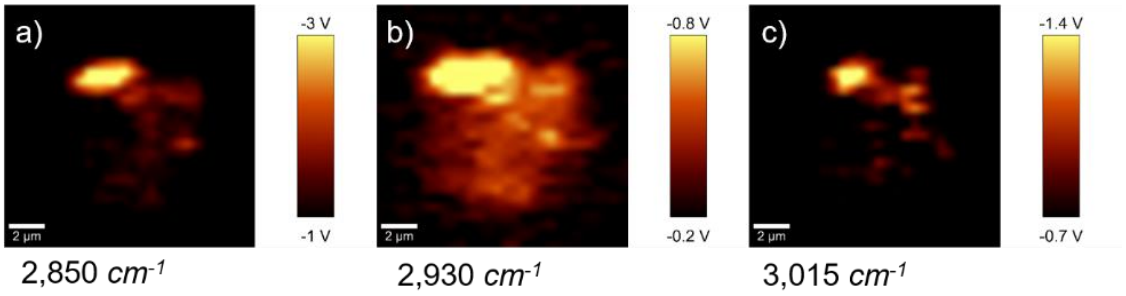

Figure 47: TOM-1 cells incubated in OA at 2,850 cm^{-1}, 2,930 cm^{-1}, and 3,015 cm^{-1}, respectively. Scale bars corresponding to 2 µm.

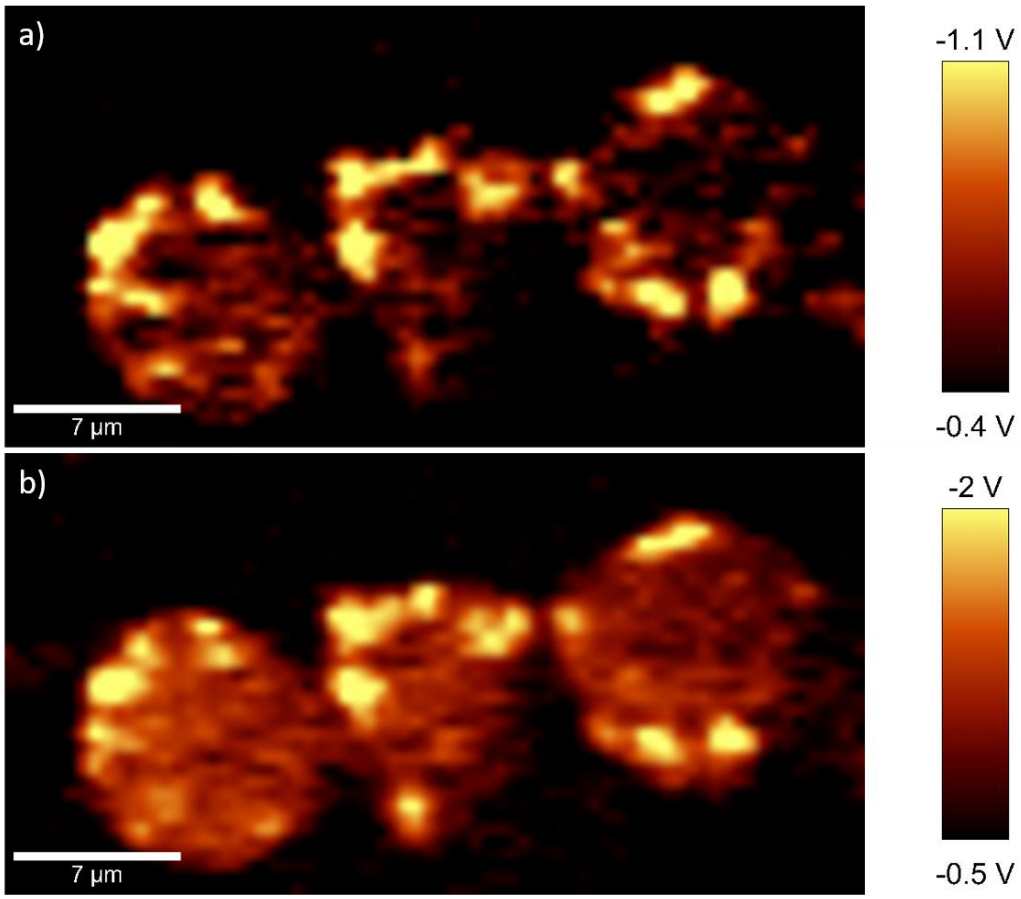

Figure 48: TOM-1 cells incubated in OA imaged at (a) 2,850 cm^{-1} and (b) 2,930 cm^{-1}. Scale bars corresponding to 7 µm.

These results underscore the potential of combining microfluidics with stimulated Raman microscopy and optical tweezers, especially for leukaemia diagnostics. The process is dynamic and fast, only taking a few tens of seconds to scan cells. The advantage of integrating optical tweezer with microscopy allows continuous imaging of a cell for extended periods of time, thus unravelling new information. The technique is label-free, which means it requires no additional staining or markers to modify the cell surface.

Here, we employed the OHT device in combination with SRS microscopy to successfully study the uptake of fatty acids in leukaemic cells via imaging. High levels of unsaturated lipids have been linked with cancer cells, and Li et al. proposed the increase in unsaturated lipids as a potential metabolic

marker for ovarian cancer stem cells (CSCs) using SRS microscopy and mass spectrometry analysis (195). They highlighted the role of the nuclear factor κB (NF-κB) pathway in the regulation of the expression levels of lipid desaturases. The study proposed targeting lipid desaturation as a therapeutic approach in ovarian cancers.

Sarri et al. developed a framework for gastrointestinal cancer detection based on stimulated Raman imaging by studying the ratio between CH_3 and CH_2 with less than 1 μm resolution (196). The presence of collagen in gastrointestinal tissues is a crucial indicator of cancer development and can be correlated by quantifying the ratio between CH_3 and CH_2. On the other hand, in conventional histology, collagen can only be visualised using saffron staining.

Du et al. studied drug-resistive mesenchymal cells and identified upregulation in lipid activity via SRS imaging. They specifically focused on the spectral region of 2,800 cm^{-1}–3,100 cm^{-1} to investigate lipid droplets in cancer cells recognising fatty acid synthesis pathways that are susceptible to drugs (197).

Zhang et al. applied stimulated Raman microscopy to quantify lipid droplets in glucose-starved HeLa cells and outlined the importance of lipogenic activity (198). They acquired 60 images in 2 minutes (512 by 512 pixels) and used particle-tracking plugins to quantify lipid droplet trajectories to deduce the size and their movement.

Using SRS imaging cytometry, Huang et al. revealed protrusions containing lipid droplets as metabolic markers to identify stress resistance in human pancreatic cancer cells when subjected to starvation and chemotherapeutic drugs (199).

Hislop et al. combined SRS microscopy with k-means cluster analysis (KMCA) to study lipid biochemistry for prostate cancer across higher spectral regions (2,800 cm^{-1}–3,100 cm^{-1}). They explored the potential of chemometric analysis—such as KMCA combined with SRS microscopy—to streamline, analyse, and robustly segment multiplex labels within the same sample in depth (200).

All of the above-mentioned studies demonstrate the potential of SRS microscopy to study imbalances in lipid pathways and metabolism as well as

identify characteristic markers for specific types of cancer, thus furthering our understanding of cancer. In this thesis, a portable microfluidic platform combined with SRS is proposed, offering the ability to screen individual cells non-invasively in a systematic manner.

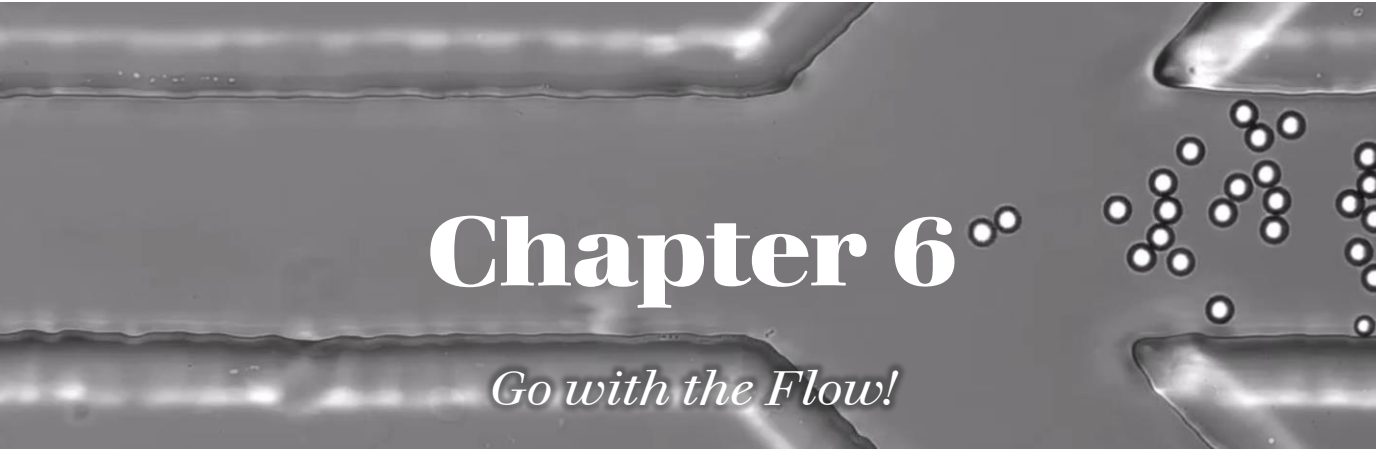

Chapter 6

Go with the Flow!

6.1 Conclusion

Single-cell manipulation tools are popular and widely applicable, especially in biological systems if one is interested in isolating and understanding the behaviour of individual cells in a population. Optical tweezers, chosen for their non-contact application of forces on cells, are widely adopted for studying cells, bacteria, and viruses. Microfluidics, with its precise fluid manipulation at the micron scale, has also emerged as a powerful tool for biological investigations. This thesis extensively explored the principles of opto-hydrodynamic tweezers—a fusion of optical tweezers and microfluidics designed to manipulate single cells.

The OHT device successfully focused and delivered single-cells to desired locations in the channel with a precision of ± 2 μm owing to the incorporation of 3D hydrodynamic focusing. The use of a four-way sheath flow allowed excellent control over the fluid flow, with an extended operational velocity range between 190 μm/s–5,000 μm/s to trap cells. The trapped particle/cell was translated over a long distance—up to 500 μm from the tip of the optical fiber. The trapped cells were successfully rotated to capture 3D spatial information of a single cell. This device also offers the possibility to sort cells of interest. To demonstrate the sorting capability of the device, two approaches—optical fibre–assisted and sheath flow–assisted sorting—were verified. A range of particles with varying refractive indices and sizes (from 3 μm to 50 μm) were successfully trapped within the OHT.

This thesis also highlighted the significance of leukaemia diagnosis and explored potential areas of improvement within the current diagnostic framework. The conventional prognosis for leukaemia, which can take approximately up to a month, can be expedited significantly by utilising a lab-on-a-chip platform for collecting and analysing white blood cells. The microfluidic platform integrated innovative optics and hydrodynamics and stands out for its capability to trap, translate, rotate, and isolate single cells of interest. The integration with Raman microscopy provided molecular

characterisation of single cells and offered crucial insights into the distribution of proteins, lipids, nucleic acids, and DNA content within the trapped cell. This information is pivotal for distinguishing between various leukaemia subtypes.

This thesis expounds on assessing the lipid content in the white blood cells from healthy peripheral blood mononuclear cells and leukaemic TOM-1 cell lines. The tracking and analysis of lipid metabolism pathways—which are often directly linked to malignancy—hold the potential to revolutionise current diagnostic regimes and enhance treatment efficacy through personalised approaches. The outcomes of this study underscore the system's indispensable role within the diagnostic workflow, with its ability to capture images of single cells and isolate cells for chemosensitivity tests. The fusion of optical tweezers and microfluidics not only broadens our understanding of single-cell manipulation but also paves the way for transformative advancements in the diagnosis and treatment of leukaemia and other related conditions.

6.2 Improvements and Future Work

The stability of the trap over extended acquisition periods poses a significant challenge in tweezing methodologies, particularly when investigating dynamic changes within trapped cells under external stimuli. The trap's stability is directly influenced by its stiffness—a parameter that can be enhanced by elevating the applied laser power to secure the cells. Optical forces exerted on the cell increase proportionally and are contingent on the cell's properties such as size, refractive index contrast with its surroundings, and shape. Addressing flow-related aspects involves minimising fluctuations to control drag forces effectively. The presence of air within the system can lead to variations in internal pressure, causing abrupt changes in flow rates due to air compressibility. Mitigating this particular issue involves degassing the PDMS chip in a desiccator and ensuring tubing and syringes are free from air bubbles to achieve system saturation. Additionally, transitioning to glass-based devices could potentially minimise fluctuations, enhance device response time, and improve imaging quality.

Significant enhancements can be implemented to automate the trapping and subsequent release of cells post–Raman acquisition. Currently, many experiments rely on manually operated control switches for trapping and releasing cells after acquisition, severely limiting system throughput and,

occasionally, resulting in cell loss due to human errors. A more effective approach involves establishing feedback between the tweezing laser and syringe pumps and incorporating well-defined parameters for cell manipulation. This automated feedback mechanism ensures that the system dynamically adjusts laser powers and fluid flows to compensate for fluctuations, thereby maintaining the trapped cell at optimal stability. Consequently, this automation has the potential to significantly increase system throughput while minimising the need for manual intervention.

Enhancing the imaging quality and sensitivity of the SRS setup can reduce the acquisition time for Raman signals significantly, thereby improving the speed of registering SRS maps and increasing system throughput. Improved sensitivity is crucial for detecting low-concentration species in microfluidic channels, enabling real-time tracking of components and subtle molecular changes. To achieve better signal detection, noise reduction is essential, and this can be accomplished by minimising background and system noise, which will facilitate clearer Raman signals.

Higher temporal and spatial resolution in SRS systems—a critical area of research—can revolutionise biomedical applications (201). Using high-quality objective lenses or adaptive optics, or optimising the optical path, can also enhance spatial resolution, which is crucial for microfluidic applications requiring detailed observation of cellular morphology.

Meanwhile, improving the temporal resolution of the SRS system is pivotal for tracking rapid molecular interactions in microfluidic channels. Faster acquisition times facilitate real-time monitoring of dynamic reactions and cellular metabolism, supported by the application of real-time data analysis algorithms. Wavelength flexibility in SRS systems, achieved through easily tuneable lasers or broadband SRS techniques, broadens the scope of analyses by capturing a wide range of Raman shifts simultaneously (202,203).

Multi-channel detection systems enable the study of multiple chemical species within a single measurement, offering more comprehensive analysis and the ability to probe different molecular vibrational modes. The flexibility to switch between wavelengths or operate at multiple wavelengths simultaneously has the potential to revolutionise the study of cellular behaviour. Additionally, combining SRS with other imaging modalities such

as fluorescence microscopy provides a comprehensive view of cellular processes and increases effective resolution (204).

In contemporary clinical diagnostics, there is a growing reliance on machine learning and deep learning, with continuous advancements in data analysis methods (205–207). The utilisation of these techniques in the analysis of spectral data, including spectra and images, presents extensive possibilities for integrating spectroscopic methods into clinical diagnostics. Machine learning algorithms and neural networks facilitate the automation of cell counting (208), classification (185,209,210), and image segmentation (208,211). Moreover, these methods improve the quality of acquired data and image reconstruction (212–214) by correcting aberrations and enhancing both temporal and spatial resolution post-acquisition. Advanced software algorithms are employed to optimise wavelength selection based on sample characteristics, which ensures that the most relevant information is captured during analysis. This streamlines data interpretation, enhances accuracy, facilitates the construction of reliable models, and aids in interpreting complex SRS data, particularly in scenarios involving multiple species or reactions in a microfluidic setup.

In the realm of portable diagnostic devices, the miniaturisation of SRS systems emerges as a pivotal aspect. This area of research holds significant promise for the future of cell analysis and broader applications in biomedical science. The ongoing trend toward more compact SRS systems facilitates seamless integration with other technologies, particularly microfluidic devices. A promising avenue for future research lies in the development of chip-based SRS systems. The objective is to create systems that seamlessly integrate into existing lab configurations or even become part of portable devices, offering functionalities similar to their larger counterparts but within a more compact form factor.

As we anticipate the miniaturisation and integration of SRS systems with microfluidics, the automation of the sample handling process becomes a desirable direction. This achievement could markedly expedite the analysis timeframe and reduce the likelihood of human errors. Additionally, incorporating automated cell sorting based on the SRS signal would allow for the continuation of the diagnostic process for individual cell fractions, enabling additional tests such as drug resistance testing.

The ability to study single cells at different wavenumbers using SRS and identify characteristic peaks within the spectral fingerprint that can be linked directly to the disease holds great promise. Collecting such datasets and images from across the world to build a biobank consisting of SRS spectra can ultimately lead to rapid development in the diagnosis process. Furthermore, these characteristic peaks correspond to specific molecules within the cell. Mapping these molecules could accelerate research in the areas of drug development and refine our understanding of cancers.

By concentrating on the outlined directions of development in both SRS and microfluidic systems, along with data analysis, researchers can aim to establish diagnostic platforms that are not only more versatile but also more efficient in capturing relevant data and detecting malignant cells and their subtypes with high sensitivity and specificity. This progress holds the potential to instil greater hope and positive outcomes for individuals facing health challenges.

Bibliography

1. Sung H, Ferlay J, Siegel RL, Laversanne M, Soerjomataram I, Jemal A, et al. Global Cancer Statistics 2020: GLOBOCAN Estimates of Incidence and Mortality Worldwide for 36 Cancers in 185 Countries. CA Cancer J Clin. 2021 May 4;71(3):209–49.

2. Chiaretti S, Zini G, Bassan R. DIAGNOSIS AND SUBCLASSIFICATION OF ACUTE LYMPHOBLASTIC LEUKEMIA. Mediterr J Hematol Infect Dis. 2014 Oct 24;6(1):e2014073.

3. Blackburn LM, Bender S, Brown S. Acute Leukemia: Diagnosis and Treatment. Semin Oncol Nurs. 2019 Dec;35(6):150950.

4. Hochhaus A. State of the Art in CML: Update. Clin Lymphoma Myeloma Leuk. 2021 Sep;21:S151–2.

5. Cerchione C, Martinelli G. Acute leukemias in 2020: state of the art. Minerva Med. 2020 Nov;111(5).

6. Pérez-Carretero C, González-Gascón-y-Marín I, Rodríguez-Vicente AE, Quijada-Álamo M, Hernández-Rivas JÁ, Hernández-Sánchez M, et al. The Evolving Landscape of Chronic Lymphocytic Leukemia on Diagnosis, Prognosis and Treatment. Diagnostics. 2021 May 10;11(5):853.

7. Vistain LF, Tay S. Single-Cell Proteomics. Trends Biochem Sci. 2021 Aug;46(8):661–72.

8. Chappell L, Russell AJC, Voet T. Single-Cell (Multi)omics Technologies. Annu Rev Genomics Hum Genet. 2018 Aug 31;19(1):15–41.

9. Yuan GC, Cai L, Elowitz M, Enver T, Fan G, Guo G, et al. Challenges and emerging directions in single-cell analysis. Genome Biol. 2017 Dec 8;18(1):84.

10. Yofe I, Dahan R, Amit I. Single-cell genomic approaches for developing the next generation of immunotherapies. Nat Med. 2020 Feb 3;26(2):171–7.

11. Shukla VC, Kuang T rong, Senthilvelan A, Higuita-Castro N, Duarte-Sanmiguel S, Ghadiali SN, et al. Lab-on-a-Chip Platforms for Biophysical Studies of Cancer with Single-Cell Resolution. Trends Biotechnol. 2018 May;36(5):549–61.

12. Bustamante C, Bryant Z, Smith SB. Ten years of tension: single-molecule DNA mechanics. Nature. 2003 Jan;421(6921):423–7.

13. Bustamante CJ, Chemla YR, Liu S, Wang MD. Optical tweezers in single-molecule biophysics. Nature Reviews Methods Primers. 2021 Mar 25;1(1):25.

14. Mendelsohn BA, Bennett NK, Darch MA, Yu K, Nguyen MK, Pucciarelli D, et al. A high-throughput screen of real-time ATP levels in individual cells reveals mechanisms of energy failure. PLoS Biol. 2018 Aug 27;16(8):e2004624.

15. Pathak D, Shields LY, Mendelsohn BA, Haddad D, Lin W, Gerencser AA, et al. The Role of Mitochondrially Derived ATP in Synaptic Vesicle Recycling. Journal of Biological Chemistry. 2015 Sep;290(37):22325–36.

16. Zhang J, Han X, Lin Y. Dissecting the regulation and function of ATP at the single-cell level. PLoS Biol. 2018 Dec 14;16(12):e3000095.

17. Wang D, He P, Wang Z, Li G, Majed N, Gu AZ. Advances in single cell Raman spectroscopy technologies for biological and environmental applications. Curr Opin Biotechnol. 2020 Aug;64:218–29.

18. DeSantis MC, Kim JH, Song H, Klasse PJ, Cheng W. Quantitative Correlation between Infectivity and Gp120 Density on HIV-1 Virions Revealed by Optical Trapping Virometry. Journal of Biological Chemistry. 2016 Jun;291(25):13088–97.

19. Hou J, Shen J, Zhao N, Yang CT, Thierry B, Zhou X, et al. Detection of a single circulating tumor cell using a genetically engineered antibody-like phage nanofiber probe. Mater Today Adv. 2021 Dec;12:100168.

20. Li R, Gong Z, Yi K, Li W, Liu Y, Wang F, et al. Efficient Detection and Single-Cell Extraction of Circulating Tumor Cells in Peripheral Blood. ACS Appl Bio Mater. 2020 Sep 21;3(9):6521–8.

21. Feng Z, Feng Y, Wang N. Circulating Tumor Cells in the Early Detection of Human Cancers. In: Handbook of Cancer and Immunology. Cham: Springer International Publishing; 2022. p. 1–20.

22. Comi TJ, Do TD, Rubakhin SS, Sweedler J V. Categorizing Cells on the Basis of their Chemical Profiles: Progress in Single-Cell Mass Spectrometry. J Am Chem Soc. 2017 Mar 22;139(11):3920–9.

23. Zaragosi LE, Deprez M, Barbry P. Using single-cell RNA sequencing to unravel cell lineage relationships in the respiratory tract. Biochem Soc Trans. 2020 Feb 28;48(1):327–36.

24. Gao D, Jin F, Zhou M, Jiang Y. Recent advances in single cell manipulation and biochemical analysis on microfluidics. Analyst. 2019;144(3):766–81.

25. Stylianou A, Lekka M, Stylianopoulos T. AFM assessing of nanomechanical fingerprints for cancer early diagnosis and classification: from single cell to tissue level. Nanoscale. 2018;10(45):20930–45.

26. Toepfner N, Herold C, Otto O, Rosendahl P, Jacobi A, Kräter M, et al. Detection of human disease conditions by single-cell morpho-rheological phenotyping of blood. Elife. 2018 Jan 13;7.

27. Liu PY, Chin LK, Ser W, Chen HF, Hsieh CM, Lee CH, et al. Cell refractive index for cell biology and disease diagnosis: past, present and future. Lab Chip. 2016;16(4):634–44.

28. González-Bermúdez B, Kobayashi H, Navarrete Á, Nyblad C, González-Sánchez M, de la Fuente M, et al. Single-cell biophysical study reveals deformability and internal ordering relationship in T cells. Soft Matter. 2020;16(24):5669–78.

29. Okamoto K, Germond A, Fujita H, Furusawa C, Okada Y, Watanabe TM. Single cell analysis reveals a biophysical aspect of collective cell-state transition in embryonic stem cell differentiation. Sci Rep. 2018 Aug 10;8(1):11965.

30. Bobrowska J, Awsiuk K, Pabijan J, Bobrowski P, Lekki J, Sowa KM, et al. Biophysical and Biochemical Characteristics as Complementary Indicators of Melanoma Progression. Anal Chem. 2019 Aug 6;91(15):9885–92.

31. Huang L, Liang F, Feng Y, Zhao P, Wang W. On-chip integrated optical stretching and electrorotation enabling single-cell biophysical analysis. Microsyst Nanoeng. 2020 Jun 15;6(1):57.

32. Shukla VC, Kuang T rong, Senthilvelan A, Higuita-Castro N, Duarte-Sanmiguel S, Ghadiali SN, et al. Lab-on-a-Chip Platforms for Biophysical Studies of Cancer with Single-Cell Resolution. Trends Biotechnol. 2018 May;36(5):549–61.

33. Russell AB, Trapnell C, Bloom JD. Extreme heterogeneity of influenza virus infection in single cells. Elife. 2018 Feb 16;7.

34. Martinez-Garcia M, Martinez-Hernandez F, Martínez Martínez J. Single-Virus Genomics: Studying Uncultured Viruses, One at a Time. In: Encyclopedia of Virology. Elsevier; 2021. p. 184–90.

35. Suomalainen M, Greber UF. Virus Infection Variability by Single-Cell Profiling. Viruses. 2021 Aug 9;13(8):1568.

36. Zhu Y, Li J, Lin X, Huang X, Hoffmann MR. Single-Cell Phenotypic Analysis and Digital Molecular Detection Linkable by a Hydrogel Bead-Based Platform. ACS Appl Bio Mater. 2021 Mar 15;4(3):2664–74.

37. Imdahl F, Vafadarnejad E, Homberger C, Saliba AE, Vogel J. Single-cell RNA-sequencing reports growth-condition-specific global transcriptomes of individual bacteria. Nat Microbiol. 2020 Aug 17;5(10):1202–6.

38. Soifer I, Robert L, Amir A. Single-Cell Analysis of Growth in Budding Yeast and Bacteria Reveals a Common Size Regulation Strategy. Current Biology. 2016 Feb;26(3):356–61.

39. Ma P, Amemiya HM, He LL, Gandhi SJ, Nicol R, Bhattacharyya RP, et al. Bacterial droplet-based single-cell RNA-seq reveals antibiotic-associated heterogeneous cellular states. Cell. 2023 Feb;186(4):877-891.e14.

40. Li H, Hsieh K, Wong PK, Mach KE, Liao JC, Wang TH. Single-cell pathogen diagnostics for combating antibiotic resistance. Nature Reviews Methods Primers. 2023 Feb 2;3(1):6.

41. Davey HM, Kell DB. Flow cytometry and cell sorting of heterogeneous microbial populations: the importance of single-cell analyses. Microbiol Rev. 1996 Dec;60(4):641–96.

42. Darzynkiewicz Z, Bedner E, Li X, Gorczyca W, Melamed MR. Laser-Scanning Cytometry: A New Instrumentation with Many Applications. Exp Cell Res. 1999 May;249(1):1–12.

43. Vembadi A, Menachery A, Qasaimeh MA. Cell Cytometry: Review and Perspective on Biotechnological Advances. Front Bioeng Biotechnol. 2019 Jun 18;7.

44. Mathur L, Ballinger M, Utharala R, Merten CA. Microfluidics as an Enabling Technology for Personalized Cancer Therapy. Small. 2020 Mar 20;16(9).

45. Kumari S, Saha U, Bose M, Murugan D, Pachauri V, Sai VVR, et al. Microfluidic Platforms for Single Cell Analysis: Applications in Cellular Manipulation and Optical Biosensing. Chemosensors. 2023 Feb 2;11(2):107.

46. Khan M, Bi Y, Zhang G, Yin F, Xie Y, Lin L, et al. Microfluidics add-on technologies for single-cell analysis. TrAC Trends in Analytical Chemistry. 2023 Oct;167:117257.

47. Weiz SM, Medina-Sánchez M, Schmidt OG. Microsystems for Single-Cell Analysis. Adv Biosyst. 2018 Feb 21;2(2).

48. Luo T, Fan L, Zhu R, Sun D. Microfluidic Single-Cell Manipulation and Analysis: Methods and Applications. Micromachines (Basel). 2019 Feb 1;10(2):104.

49. Wyatt Shields IV C, Reyes CD, López GP. Microfluidic cell sorting: a review of the advances in the separation of cells from debulking to rare cell isolation. Lab Chip. 2015;15(5):1230–49.

50. Niculescu AG, Chircov C, Bîrcă AC, Grumezescu AM. Fabrication and Applications of Microfluidic Devices: A Review. Int J Mol Sci. 2021 Feb 18;22(4):2011.

51. Blay V, Tolani B, Ho SP, Arkin MR. High-Throughput Screening: today's biochemical and cell-based approaches. Drug Discov Today. 2020 Oct;25(10):1807–21.

52. Reece A, Xia B, Jiang Z, Noren B, McBride R, Oakey J. Microfluidic techniques for high throughput single cell analysis. Curr Opin Biotechnol. 2016 Aug;40:90–6.

53. Du G, Fang Q, den Toonder JMJ. Microfluidics for cell-based high throughput screening platforms—A review. Anal Chim Acta. 2016 Jan;903:36–50.

54. Zhang S, Wang Y, Onck P, den Toonder J. A concise review of microfluidic particle manipulation methods. Microfluid Nanofluidics. 2020 Apr 19;24(4):24.

55. Yun H, Kim K, Lee WG. Cell manipulation in microfluidics. Biofabrication. 2013 Feb 13;5(2):022001.

56. Manzoor AA, Romita L, Hwang DK. A review on microwell and microfluidic geometric array fabrication techniques and its potential applications in cellular studies. Can J Chem Eng. 2021 Jan 13;99(1):61–96.

57. Liu Y, Yu M. Investigation of inclined dual-fiber optical tweezers for 3D manipulation and force sensing. Opt Express. 2009 Aug 3;17(16):13624.

58. Mitchem L, Reid JP. Optical manipulation and characterisation of aerosol particles using a single-beam gradient force optical trap. Chem Soc Rev. 2008;37(4):756.

59. Noh S, Song Y. Dielectrophoretic Trapping for Nanoparticles, High-Molecule-Weight DNA, and SYBR Gold Using Polyimide-Based Printed Circuit Board. IEEE Sens J. 2021 Sep 1;21(17):18451–8.

60. Bhattacharya S, Chao T, Ros A. Insulator-based dielectrophoretic single particle and single cancer cell trapping. Electrophoresis. 2011 Sep 23;32(18):2550–8.

61. Hölzel R, Calander N, Chiragwandi Z, Willander M, Bier FF. Trapping Single Molecules by Dielectrophoresis. Phys Rev Lett. 2005 Sep 13;95(12):128102.

62. Drinkwater BW. A Perspective on acoustical tweezers—devices, forces, and biomedical applications. Appl Phys Lett. 2020 Nov 2;117(18).

63. Ozcelik A, Rufo J, Guo F, Gu Y, Li P, Lata J, et al. Acoustic tweezers for the life sciences. Nat Methods. 2018 Dec 26;15(12):1021–8.

64. Lutz BR, Chen J, Schwartz DT. Hydrodynamic Tweezers: 1. Noncontact Trapping of Single Cells Using Steady Streaming Microeddies. Anal Chem. 2006 Aug 1;78(15):5429–35.

65. Lieu VH, House TA, Schwartz DT. Hydrodynamic Tweezers: Impact of Design Geometry on Flow and Microparticle Trapping. Anal Chem. 2012 Feb 21;84(4):1963–8.

66. Hong C, Yang S, Ndukaife JC. Stand-off trapping and manipulation of sub-10 nm objects and biomolecules using opto-thermo-electrohydrodynamic tweezers. Nat Nanotechnol. 2020 Nov 31;15(11):908–13.

67. Zhang P, Rufo J, Chen C, Xia J, Tian Z, Zhang L, et al. Acoustoelectronic nanotweezers enable dynamic and large-scale control of nanomaterials. Nat Commun. 2021 Jun 22;12(1):3844.

68. Lin L, Wang M, Peng X, Lissek EN, Mao Z, Scarabelli L, et al. Opto-thermoelectric nanotweezers. Nat Photonics. 2018 Apr 26;12(4):195–201.

69. Zhang S, Scott EY, Singh J, Chen Y, Zhang Y, Elsayed M, et al. The optoelectronic microrobot: A versatile toolbox for micromanipulation. Proceedings of the National Academy of Sciences. 2019 Jul 23;116(30):14823–8.

70. Li M, Liu H, Zhuang S, Goda K. Droplet flow cytometry for single-cell analysis. RSC Adv. 2021;11(34):20944–60.

71. Jiang Z, Shi H, Tang X, Qin J. Recent advances in droplet microfluidics for single-cell analysis. TrAC Trends in Analytical Chemistry. 2023 Feb;159:116932.

72. Matuła K, Rivello F, Huck WTS. Single-Cell Analysis Using Droplet Microfluidics. Adv Biosyst. 2020 Jan 26;4(1).

73. Lin CH, Hsiao YH, Chang HC, Yeh CF, He CK, Salm EM, et al. A microfluidic dual-well device for high-throughput single-cell capture and culture. Lab Chip. 2015;15(14):2928–38.

74. Luo T, Hou J, Chen S, Chow YT, Wang R, Ma D, et al. Microfluidic single-cell array platform enabling week-scale clonal expansion under chemical/electrical stimuli. Biomicrofluidics. 2017 Sep 1;11(5).

75. Wlodkowic D, Faley S, Zagnoni M, Wikswo JP, Cooper JM. Microfluidic Single-Cell Array Cytometry for the Analysis of Tumor Apoptosis. Anal Chem. 2009 Jul 1;81(13):5517–23.

76. Di Carlo D, Aghdam N, Lee LP. Single-Cell Enzyme Concentrations, Kinetics, and Inhibition Analysis Using High-Density Hydrodynamic Cell Isolation Arrays. Anal Chem. 2006 Jul 1;78(14):4925–30.

77. Prakadan SM, Shalek AK, Weitz DA. Scaling by shrinking: empowering single-cell 'omics' with microfluidic devices. Nat Rev Genet. 2017 Jun 10;18(6):345–61.

78. Revzin A, Sekine K, Sin A, Tompkins RG, Toner M. Development of a microfabricated cytometry platform for characterization and sorting of individual leukocytes. Lab Chip. 2005;5(1):30.

79. Han X, Wang R, Zhou Y, Fei L, Sun H, Lai S, et al. Mapping the Mouse Cell Atlas by Microwell-Seq. Cell. 2018 Feb;172(5):1091-1107.e17.

80. Unger MA, Chou HP, Thorsen T, Scherer A, Quake SR. Monolithic Microfabricated Valves and Pumps by Multilayer Soft Lithography. Science (1979). 2000 Apr 7;288(5463):113–6.

81. Lecault V, VanInsberghe M, Sekulovic S, Knapp DJHF, Wohrer S, Bowden W, et al. High-throughput analysis of single hematopoietic stem cell proliferation in microfluidic cell culture arrays. Nat Methods. 2011 Jul 22;8(7):581–6.

82. Sun Y, Cai B, Wei X, Wang Z, Rao L, Meng Q, et al. A valve-based microfluidic device for on-chip single cell treatments. Electrophoresis. 2019 Mar 9;40(6):961–8.

83. Johnson-Chavarria EM, Agrawal U, Tanyeri M, Kuhlman TE, Schroeder CM. Automated single cell microbioreactor for monitoring intracellular dynamics and cell growth in free solution. Lab Chip. 2014;14(15):2688–97.

84. Shenoy A, Rao C V., Schroeder CM. Stokes trap for multiplexed particle manipulation and assembly using fluidics. Proceedings of the National Academy of Sciences. 2016 Apr 12;113(15):3976–81.

85. Tanyeri M, Ranka M, Sittipolkul N, Schroeder CM. A microfluidic-based hydrodynamic trap: design and implementation. Lab Chip. 2011;11(10):1786.

86. Kirschbaum M, Guernth-Marschner CR, Cherré S, de Pablo Peña A, Jaeger MS, Kroczek RA, et al. Highly controlled electrofusion of individually selected cells in dielectrophoretic field cages. Lab Chip. 2012;12(3):443–50.

87. PETHIG R, MARKX G. Applications of dielectrophoresis in biotechnology. Trends Biotechnol. 1997 Oct;15(10):426–32.

88. Sivagnanam V, Song B, Vandevyver C, Bünzli JCG, Gijs MAM. Selective Breast Cancer Cell Capture, Culture, and Immunocytochemical Analysis Using Self-Assembled Magnetic Bead Patterns in a Microfluidic Chip. Langmuir. 2010 May 4;26(9):6091–6.

89. Luo T, Fan L, Zeng Y, Liu Y, Chen S, Tan Q, et al. A simplified sheathless cell separation approach using combined gravitational-sedimentation-based prefocusing and dielectrophoretic separation. Lab Chip. 2018;18(11):1521–32.

90. Meng L, Cai F, Chen J, Niu L, Li Y, Wu J, et al. Precise and programmable manipulation of microbubbles by two-dimensional standing surface acoustic waves. Appl Phys Lett. 2012 Apr 23;100(17).

91. Shields IV CW, Wang JL, Ohiri KA, Essoyan ED, Yellen BB, Armstrong AJ, et al. Magnetic separation of acoustically focused cancer cells from blood for magnetographic templating and analysis. Lab Chip. 2016;16(19):3833–44.

92. Collins DJ, Morahan B, Garcia-Bustos J, Doerig C, Plebanski M, Neild A. Two-dimensional single-cell patterning with one cell per well driven by surface acoustic waves. Nat Commun. 2015 Nov 2;6(1):8686.

93. Decombe JB, Huant S, Fick J. Single and dual fiber nano-tip optical tweezers: trapping and analysis. Opt Express. 2013 Dec 16;21(25):30521.

94. Guck J, Ananthakrishnan R, Mahmood H, Moon TJ, Cunningham CC, Käs J. The Optical Stretcher: A Novel Laser Tool to Micromanipulate Cells. Biophys J. 2001 Aug;81(2):767–84.

95. Jess PRT, Garcés-Chávez V, Smith D, Mazilu M, Paterson L, Riches A, et al. Dual beam fibre trap for Raman micro-spectroscopy of single cells. Opt Express. 2006;14(12):5779.

96. Rancourt-Grenier S, Wei MT, Bai JJ, Chiou A, Bareil PP, Duval PL, et al. Dynamic deformation of red blood cells in Dual-trap Optical Tweezers. Opt Express. 2010 May 10;18(10):10462.

97. Black BJ, Mohanty SK. Fiber-optic spanner. Opt Lett. 2012 Dec 15;37(24):5030.

98. Sil S, Saha TK, Kumar A, Bera SK, Banerjee A. Dual-mode optical fiber-based tweezers for robust trapping and manipulation of absorbing particles in air. Journal of Optics. 2017 Dec 1;19(12):12LT02.

99. Asadollahbaik A, Kumar A, Heymann M, Giessen H, Fick J. Fresnel lens optical fiber tweezers to evaluate the vitality of single algae cells. Opt Lett. 2022 Jan 1;47(1):170.

100. Plidschun M, Ren H, Kim J, Förster R, Maier SA, Schmidt MA. Ultrahigh numerical aperture meta-fibre for flexible optical trapping. Light Sci Appl. 2021 Mar 15;10(1):57.

101. Lindström S, Andersson-Svahn H. Miniaturization of biological assays — Overview on microwell devices for single-cell analyses. Biochimica et Biophysica Acta (BBA) - General Subjects. 2011 Mar;1810(3):308–16.

102. Pang L, Ding J, Liu XX, Yuan H, Ge Y, Fan J, et al. Microstructure-based techniques for single-cell manipulation and analysis. TrAC Trends in Analytical Chemistry. 2020 Aug;129:115940.

103. Li J, Shen C, Huang TJ, Cummer SA. Acoustic tweezer with complex boundary-free trapping and transport channel controlled by shadow waveguides. Sci Adv. 2021 Aug 20;7(34).

104. Ashkin A, Dziedzic JM, Bjorkholm JE, Chu S. Observation of a single-beam gradient force optical trap for dielectric particles. Opt Lett. 1986 May 1;11(5):288.

105. Ashkin A. Forces of a single-beam gradient laser trap on a dielectric sphere in the ray optics regime. Biophys J. 1992 Feb;61(2):569–82.

106. Vasantham S, Garstecki P, Derzsi L, Kotnala A. Opto-hydrodynamic fiber tweezers for stimulated raman imaging cytometry of leukemic cells. In: Dholakia K, Spalding GC, editors. Optical Trapping and Optical Micromanipulation XX. SPIE; 2023. p. 90.

107. Vasantham SK, Garstecki P, Derzsi L, Kotnala A. On-chip Opto-hydrodynamic Tweezers for Single Cell Manipulation. In: Biophotonics Congress: Optics in the Life Sciences 2023 (OMA, NTM, BODA, OMP, BRAIN). Washington, D.C.: Optica Publishing Group; 2023. p. ATh1D.5.

108. Vasantham S, Kotnala A, Promovych Y, Garstecki P, Derzsi L. Opto-hydrodynamic tweezers. Lab Chip. 2024;

109. Nall JR, Lathrop JW. Photolithographic fabrication techniques for transistors which are an integral part of a printed circuit. In: 1957 International Electron Devices Meeting. IRE; 1957. p. 117–117.

110. Manz A, Graber N, Widmer HM. Miniaturized total chemical analysis systems: A novel concept for chemical sensing. Sens Actuators B Chem. 1990 Jan;1(1–6):244–8.

111. Whitesides GM. The origins and the future of microfluidics. Nature. 2006 Jul 26;442(7101):368–73.

112. Xia Y, Whitesides GM. Soft Lithography. Angewandte Chemie International Edition. 1998 Mar 16;37(5):550–75.

113. Shaegh SAM, Pourmand A, Nabavinia M, Avci H, Tamayol A, Mostafalu P, et al. Rapid prototyping of whole-thermoplastic microfluidics with built-in microvalves using laser ablation and thermal fusion bonding. Sens Actuators B Chem. 2018 Feb;255:100–9.

114. Morbioli GG, Speller NC, Stockton AM. A practical guide to rapid-prototyping of PDMS-based microfluidic devices: A tutorial. Anal Chim Acta. 2020 Oct;1135:150–74.

115. Halldorsson S, Lucumi E, Gómez-Sjöberg R, Fleming RMT. Advantages and challenges of microfluidic cell culture in polydimethylsiloxane devices. Biosens Bioelectron. 2015 Jan;63:218–31.

116. Reynolds O. An Experimental Investigation of the Circumstances Which Determine Whether the Motion of Water Shall Be Direct or Sinuous, and of the Law of Resistance in Parallel Channels. Vol. 174, Source: Philosophical Transactions of the Royal Society of London. 1883.

117. Raman C V. Part II.—The Raman effect. Investigation of molecular structure by light scattering. Trans Faraday Soc. 1929;25(0):781–92.

118. Butler HJ, Ashton L, Bird B, Cinque G, Curtis K, Dorney J, et al. Using Raman spectroscopy to characterize biological materials. Nat Protoc. 2016 Apr 10;11(4):664–87.

119. Kuhar N, Sil S, Verma T, Umapathy S. Challenges in application of Raman spectroscopy to biology and materials. RSC Adv. 2018;8(46):25888–908.

120. Harper MH. Optical Instrumentation for TIROS. Appl Opt. 1962 Mar 1;1(2):139.

121. Lee HJ, Cheng JX. Imaging chemistry inside living cells by stimulated Raman scattering microscopy. Methods. 2017 Sep;128:119–28.

122. Kong K, Zaabar F, Rakha E, Ellis I, Koloydenko A, Notingher I. Towards intra-operative diagnosis of tumours during breast conserving surgery by selective-sampling Raman micro-spectroscopy. Phys Med Biol. 2014 Oct 21;59(20):6141–52.

123. Roeffaers MBJ, Zhang X, Freudiger CW, Saar BG, Ruijven M van, Dalen G van, et al. Label-free imaging of biomolecules in food products using stimulated Raman microscopy. J Biomed Opt. 2011;16(2):021118.

124. Urbanczyk M. SOLAR SAILS-A REALISTIC PROPULSION FOR SPACECRAFT I 1. 1967.

125. Knight JB, Vishwanath A, Brody JP, Austin RH. Hydrodynamic Focusing on a Silicon Chip: Mixing Nanoliters in Microseconds. Phys Rev Lett. 1998 Apr 27;80(17):3863–6.

126. Kamentsky LA, Melamed MR, Derman H. Spectrophotometer: New Instrument for Ultrarapid Cell Analysis. Science (1979). 1965 Oct 29;150(3696):630–1.

127. Wang J, Tham D, Wei W, Shin YS, Ma C, Ahmad H, et al. Quantitating Cell–Cell Interaction Functions with Applications to Glioblastoma Multiforme Cancer Cells. Nano Lett. 2012 Dec 12;12(12):6101–6.

128. Wyatt Shields IV C, Reyes CD, López GP. Microfluidic cell sorting: a review of the advances in the separation of cells from debulking to rare cell isolation. Lab Chip. 2015;15(5):1230–49.

129. Piyasena ME, Graves SW. The intersection of flow cytometry with microfluidics and microfabrication. Lab Chip. 2014;14(6):1044–59.

130. Xuan X, Zhu J, Church C. Particle focusing in microfluidic devices. Microfluid Nanofluidics. 2010 Jul 30;9(1):1–16.

131. Zhao Y, Li Q, Hu X. Universally applicable three-dimensional hydrodynamic focusing in a single-layer channel for single cell analysis. Analytical Methods. 2018;10(28):3489–97.

132. Gauthier RC, Wallace S. Optical levitation of spheres: analytical development and numerical computations of the force equations. Journal of the Optical Society of America B. 1995 Sep 1;12(9):1680.

133. Kim SB, Kim SS. Radiation forces on spheres in loosely focused Gaussian beam: ray-optics regime. Journal of the Optical Society of America B. 2006 May 1;23(5):897.

134. Di Carlo D. Inertial microfluidics. Lab Chip. 2009;9(21):3038.

135. Hsu CH, Di Carlo D, Chen C, Irimia D, Toner M. Microvortex for focusing, guiding and sorting of particles. Lab Chip. 2008;8(12):2128.

136. Di Carlo D, Edd JF, Humphry KJ, Stone HA, Toner M. Particle Segregation and Dynamics in Confined Flows. Phys Rev Lett. 2009 Mar 3;102(9):094503.

137. Kotnala A, Zheng Y, Fu J, Cheng W. Microfluidic-based high-throughput optical trapping of nanoparticles. Lab Chip. 2017;17(12):2125–34.

138. Lincoln B, Schinkinger S, Travis K, Wottawah F, Ebert S, Sauer F, et al. Reconfigurable microfluidic integration of a dual-beam laser trap with biomedical applications. Biomed Microdevices. 2007 Aug 23;9(5):703–10.

139. Xu X, Cheng C, Zhang Y, Lei H, Li B. Dual focused coherent beams for three-dimensional optical trapping and continuous rotation of metallic nanostructures. Sci Rep. 2016 Jul 8;6(1):29449.

140. Liu Z, Guo C, Yang J, Yuan L. Tapered fiber optical tweezers for microscopic particle trapping: fabrication and application. Opt Express. 2006 Dec 11;14(25):12510.

141. Mohanty SK, Mohanty K, Berns MW. Manipulation of mammalian cells using a single-fiber optical microbeam. J Biomed Opt. 2008 Sep 1;13(05):1.

142. Xin H, Xu R, Li B. Optical trapping, driving and arrangement of particles using a tapered fibre probe. Sci Rep. 2012 Nov 12;2(1):818.

143. Daly M, Truong VG, Chormaic SN. Evanescent field trapping of nanoparticles using nanostructured ultrathin optical fibers. Opt Express. 2016 Jun 27;24(13):14470.

144. Tkachenko G, Truong VG, Esporlas CL, Sanskriti I, Nic Chormaic S. Evanescent field trapping and propulsion of Janus particles along optical nanofibers. Nat Commun. 2023 Mar 27;14(1):1691.

145. Skelton SE, Sergides M, Patel R, Karczewska E, Maragó OM, Jones PH. Evanescent wave optical trapping and transport of micro- and nanoparticles on tapered optical fibers. J Quant Spectrosc Radiat Transf. 2012 Dec;113(18):2512–20.

146. Bui AAM, Kashchuk A V., Balanant MA, Nieminen TA, Rubinsztein-Dunlop H, Stilgoe AB. Calibration of force detection for arbitrarily shaped particles in optical tweezers. Sci Rep. 2018 Jul 17;8(1):10798.

147. Skylaki S, Hilsenbeck O, Schroeder T. Challenges in long-term imaging and quantification of single-cell dynamics. Nat Biotechnol. 2016 Nov 8;34(11):1137–44.

148. Spiller DG, Wood CD, Rand DA, White MRH. Measurement of single-cell dynamics. Nature. 2010 Jun 9;465(7299):736–45.

149. Tang X, Liu X, Li P, Liu F, Kojima M, Huang Q, et al. On-Chip Cell–Cell Interaction Monitoring at Single-Cell Level by Efficient Immobilization of Multiple Cells in Adjustable Quantities. Anal Chem. 2020 Sep 1;92(17):11607–16.

150. Tang T, Hosokawa Y, Hayakawa T, Tanaka Y, Li W, Li M, et al. Rotation of Biological Cells: Fundamentals and Applications. Engineering. 2022 Mar;10:110–26.

151. Liu X, Huang J, Li Y, Zhang Y, Li B. Rotation and deformation of human red blood cells with light from tapered fiber probes. Nanophotonics. 2017 Jan 6;6(1):309–16.

152. Habaza M, Gilboa B, Roichman Y, Shaked NT. Tomographic phase microscopy with 180° rotation of live cells in suspension by holographic optical tweezers. Opt Lett. 2015 Apr 15;40(8):1881.

153. Jünger F, Olshausen P v., Rohrbach A. Fast, label-free super-resolution live-cell imaging using rotating coherent scattering (ROCS) microscopy. Sci Rep. 2016 Jul 28;6(1):30393.

154. Koch MD, Rohrbach A. Label-free Imaging and Bending Analysis of Microtubules by ROCS Microscopy and Optical Trapping. Biophys J. 2018 Jan;114(1):168–77.

155. Jünger F, Ruh D, Strobel D, Michiels R, Huber D, Brandel A, et al. 100 Hz ROCS microscopy correlated with fluorescence reveals cellular dynamics on different spatiotemporal scales. Nat Commun. 2022 Apr 1;13(1):1758.

156. Bonner WA, Hulett HR, Sweet RG, Herzenberg LA. Fluorescence Activated Cell Sorting. Review of Scientific Instruments. 1972 Mar 1;43(3):404–9.

157. Miltenyi S, Müller W, Weichel W, Radbruch A. High gradient magnetic cell separation with MACS. Cytometry. 1990 Jan 21;11(2):231–8.

158. Maheu B, Gréhan G, Gouesbet G. Generalized Lorenz-Mie theory: first exact values and comparisons with the localized approximation. Appl Opt. 1987 Jan 1;26(1):23.

159. Gouesbet G, Maheu B, Gréhan G. Light scattering from a sphere arbitrarily located in a Gaussian beam, using a Bromwich formulation. Journal of the Optical Society of America A. 1988 Sep 1;5(9):1427.

160. Whiteley AE, Price TT, Cantelli G, Sipkins DA. Leukaemia: a model metastatic disease. Nat Rev Cancer. 2021 Jul 5;21(7):461–75.

161. Alpert N, Rapp JL, Mascarenhas J, Scigliano E, Tremblay D, Marcellino BK, et al. Prevalence of Cytopenia in the General Population—A National Health and Nutrition Examination Survey Analysis. Front Oncol. 2020 Nov 20;10.

162. Vardiman JW, Thiele J, Arber DA, Brunning RD, Borowitz MJ, Porwit A, et al. The 2008 revision of the World Health Organization (WHO) classification of

myeloid neoplasms and acute leukemia: rationale and important changes. Blood. 2009 Jul 30;114(5):937–51.

163. Harvey RC, Tasian SK. Clinical diagnostics and treatment strategies for Philadelphia chromosome–like acute lymphoblastic leukemia. Blood Adv. 2020 Jan 14;4(1):218–28.

164. Alexander TB, Orgel E. Mixed Phenotype Acute Leukemia: Current Approaches to Diagnosis and Treatment. Curr Oncol Rep. 2021 Feb 5;23(2):22.

165. Narayanan D, Weinberg OK. How I investigate acute myeloid leukemia. Int J Lab Hematol. 2020 Feb 10;42(1):3–15.

166. Coustan-Smith E, Behm FG, Sanchez J, Boyett JM, Hancock ML, Raimondi SC, et al. Immunological detection of minimal residual disease in children with acute lymphoblastic leukaemia. The Lancet. 1998 Feb;351(9102):550–4.

167. Béné MC, Nebe T, Bettelheim P, Buldini B, Bumbea H, Kern W, et al. Immunophenotyping of acute leukemia and lymphoproliferative disorders: a consensus proposal of the European LeukemiaNet Work Package 10. Leukemia. 2011 Apr 21;25(4):567–74.

168. Sallman DA, Chaudhury A, Nguyen J, Zhang L. Handbook of Hematologic Malignancies. Sallman DA, Chaudhury A, Nguyen J, Zhang L, editors. New York, NY: Springer Publishing Company; 2020.

169. Dorosz A, Grosicki M, Dybas J, Matuszyk E, Rodewald M, Meyer T, et al. Eosinophils and Neutrophils—Molecular Differences Revealed by Spontaneous Raman, CARS and Fluorescence Microscopy. Cells. 2020 Sep 7;9(9):2041.

170. Li Y, Shen B, Li S, Zhao Y, Qu J, Liu L. Review of Stimulated Raman Scattering Microscopy Techniques and Applications in the Biosciences. Adv Biol. 2021 Jan 30;5(1).

171. Brzozowski K, Matuszyk E, Pieczara A, Firlej J, Nowakowska AM, Baranska M. Stimulated Raman scattering microscopy in chemistry and life science – Development, innovation, perspectives. Biotechnol Adv. 2022 Nov;60:108003.

172. Suzuki Y, Kobayashi K, Wakisaka Y, Deng D, Tanaka S, Huang CJ, et al. Label-free chemical imaging flow cytometry by high-speed multicolor stimulated Raman scattering. Proceedings of the National Academy of Sciences. 2019 Aug 6;116(32):15842–8.

173. Nitta N, Iino T, Isozaki A, Yamagishi M, Kitahama Y, Sakuma S, et al. Raman image-activated cell sorting. Nat Commun. 2020 Jul 10;11(1):3452.

174. Jackson JM, Taylor JB, Witek MA, Hunsucker SA, Waugh JP, Fedoriw Y, et al. Microfluidics for the detection of minimal residual disease in acute myeloid leukemia patients using circulating leukemic cells selected from blood. Analyst. 2016;141(2):640–51.

175. Petrov D V. Raman spectroscopy of optically trapped particles. Journal of Optics A: Pure and Applied Optics. 2007 Aug 1;9(8):S139–56.

176. Volpe G, Singh GP, Petrov D. Dynamics of a growing cell in an optical trap. Appl Phys Lett. 2006 Jun 5;88(23).

177. Ajito K, Torimitsu K. Laser trapping and Raman spectroscopy of single cellular organelles in the nanometer range. Lab Chip. 2002;2(1):11–4.

178. Zhang Q, Zhang P, Gou H, Mou C, Huang WE, Yang M, et al. Towards high-throughput microfluidic Raman-activated cell sorting. Analyst. 2015;140(18):6163–74.

179. McIlvenna D, Huang WE, Davison P, Glidle A, Cooper J, Yin H. Continuous cell sorting in a flow based on single cell resonance Raman spectra. Lab Chip. 2016;16(8):1420–9.

180. Lyu Y, Yuan X, Glidle A, Fu Y, Furusho H, Yang T, et al. Automated Raman based cell sorting with 3D microfluidics. Lab Chip. 2020;20(22):4235–45.

181. Goda K, Filby A, Nitta N. In Flow Cytometry, Image Is Everything. Cytometry Part A. 2019 May 3;95(5):475–7.

182. Suzuki Y, Kobayashi K, Wakisaka Y, Deng D, Tanaka S, Huang CJ, et al. Label-free chemical imaging flow cytometry by high-speed multicolor stimulated Raman scattering. Proceedings of the National Academy of Sciences. 2019 Aug 6;116(32):15842–8.

183. Isozaki A, Mikami H, Tezuka H, Matsumura H, Huang K, Akamine M, et al. Intelligent image-activated cell sorting 2.0. Lab Chip. 2020;20(13):2263–73.

184. Lau AY, Lee LP, Chan JW. An integrated optofluidic platform for Raman-activated cell sorting. Lab Chip. 2008;8(7):1116.

185. Dochow S, Krafft C, Neugebauer U, Bocklitz T, Henkel T, Mayer G, et al. Tumour cell identification by means of Raman spectroscopy in combination with optical traps and microfluidic environments. Lab Chip. 2011;11(8):1484.

186. Kuhajda FP, Jenner K, Wood FD, Hennigar RA, Jacobs LB, Dick JD, et al. Fatty acid synthesis: a potential selective target for antineoplastic therapy. Proceedings of the National Academy of Sciences. 1994 Jul 5;91(14):6379–83.

187. Mills GB, Moolenaar WH. The emerging role of lysophosphatidic acid in cancer. Nat Rev Cancer. 2003 Aug;3(8):582–91.

188. Pastorczak A, Domka K, Fidyt K, Poprzeczko M, Firczuk M. Mechanisms of Immune Evasion in Acute Lymphoblastic Leukemia. Cancers (Basel). 2021 Mar 26;13(7):1536.

189. Tsagarakis NJ, Papadhimitriou SI, Pavlidis D, Marinakis T, Kostopoulos I V., Stiakaki E, et al. Flow cytometric predictive scoring systems for common fusions ETV6/RUNX1, BCR/ABL1, TCF3/PBX1 and rearrangements of the KMT2A gene, proposed for the initial cytogenetic approach in cases of B-acute lymphoblastic leukemia. Int J Lab Hematol. 2019 Jun 7;41(3):364–72.

190. Vasantham S, Garstecki P, Derzsi L, Kotnala A. Opto-hydrodynamic fiber tweezers for stimulated raman imaging cytometry of leukemic cells. In: Dholakia K, Spalding GC, editors. Optical Trapping and Optical Micromanipulation XX. SPIE; 2023. p. 90.

191. Patra KC, Hay N. The pentose phosphate pathway and cancer. Trends Biochem Sci. 2014 Aug;39(8):347–54.

192. Baenke F, Peck B, Miess H, Schulze A. Hooked on fat: the role of lipid synthesis in cancer metabolism and tumour development. Dis Model Mech. 2013 Nov 1;6(6):1353–63.

193. Nisticò C, Chiarella E. An Overview on Lipid Droplets Accumulation as Novel Target for Acute Myeloid Leukemia Therapy. Biomedicines. 2023 Nov 30;11(12):3186.

194. Ghaeidamini Harouni M, Rahgozar S, Rahimi Babasheikhali S, Safavi A, Ghodousi ES. Fatty acid synthase, a novel poor prognostic factor for acute lymphoblastic leukemia which can be targeted by ginger extract. Sci Rep. 2020 Aug 21;10(1):14072.

195. Li J, Condello S, Thomes-Pepin J, Ma X, Xia Y, Hurley TD, et al. Lipid Desaturation Is a Metabolic Marker and Therapeutic Target of Ovarian Cancer Stem Cells. Cell Stem Cell. 2017 Mar;20(3):303-314.e5.

196. Sarri B, Canonge R, Audier X, Simon E, Wojak J, Caillol F, et al. Fast stimulated Raman and second harmonic generation imaging for intraoperative gastro-intestinal cancer detection. Sci Rep. 2019 Jul 11;9(1):10052.

197. Du J, Su Y, Qian C, Yuan D, Miao K, Lee D, et al. Raman-guided subcellular pharmaco-metabolomics for metastatic melanoma cells. Nat Commun. 2020 Sep 24;11(1):4830.

198. Zhang C, Li J, Lan L, Cheng JX. Quantification of Lipid Metabolism in Living Cells through the Dynamics of Lipid Droplets Measured by Stimulated Raman Scattering Imaging. Anal Chem. 2017 Apr 18;89(8):4502–7.

199. Huang KC, Li J, Zhang C, Tan Y, Cheng JX. Multiplex Stimulated Raman Scattering Imaging Cytometry Reveals Lipid-Rich Protrusions in Cancer Cells under Stress Condition. iScience. 2020 Mar;23(3):100953.

200. Hislop EW, Tipping WJ, Faulds K, Graham D. Label-Free Imaging of Lipid Droplets in Prostate Cells Using Stimulated Raman Scattering Microscopy and Multivariate Analysis. Anal Chem. 2022 Jun 28;94(25):8899–908.

201. Shi L, Fung AA, Zhou A. Advances in stimulated Raman scattering imaging for tissues and animals. Quant Imaging Med Surg. 2020 Mar;11(3):1078–101.

202. De la Cadena A, Valensise CM, Marangoni M, Cerullo G, Polli D. Broadband stimulated Raman scattering microscopy with wavelength-scanning detection. Journal of Raman Spectroscopy. 2020 Oct 3;51(10):1951–9.

203. De la Cadena A, Vernuccio F, Ragni A, Sciortino G, Vanna R, Ferrante C, et al. Broadband stimulated Raman imaging based on multi-channel lock-in detection for spectral histopathology. APL Photonics. 2022 Jul 1;7(7).

204. Li X, Jiang M, Lam JWY, Tang BZ, Qu JY. Mitochondrial Imaging with Combined Fluorescence and Stimulated Raman Scattering Microscopy Using a Probe of the Aggregation-Induced Emission Characteristic. J Am Chem Soc. 2017 Nov 29;139(47):17022–30.

205. Elemento O, Leslie C, Lundin J, Tourassi G. Artificial intelligence in cancer research, diagnosis and therapy. Nat Rev Cancer. 2021 Dec 17;21(12):747–52.

206. Koh DM, Papanikolaou N, Bick U, Illing R, Kahn CE, Kalpathi-Cramer J, et al. Artificial intelligence and machine learning in cancer imaging. Communications Medicine. 2022 Oct 27;2(1):133.

207. Bera K, Schalper KA, Rimm DL, Velcheti V, Madabhushi A. Artificial intelligence in digital pathology — new tools for diagnosis and precision oncology. Nat Rev Clin Oncol. 2019 Nov 9;16(11):703–15.

208. Alfonso-García A, Paugh J, Farid M, Garg S, Jester J, Potma E. A machine learning framework to analyze hyperspectral stimulated Raman scattering microscopy images of expressed human meibum. Journal of Raman Spectroscopy. 2017 Jun 11;48(6):803–12.

209. Leszczenko P, Borek-Dorosz A, Nowakowska AM, Adamczyk A, Kashyrskaya S, Jakubowska J, et al. Towards Raman-Based Screening of Acute Lymphoblastic Leukemia-Type B (B-ALL) Subtypes. Cancers (Basel). 2021 Oct 31;13(21):5483.

210. Neugebauer U, Bocklitz T, Clement JH, Krafft C, Popp J. Towards detection and identification of circulating tumour cells using Raman spectroscopy. Analyst. 2010;135(12):3178.

211. Weng W, Zhu X. INet: Convolutional Networks for Biomedical Image Segmentation. IEEE Access. 2021;9:16591–603.

212. Manifold B, Thomas E, Francis AT, Hill AH, Fu D. Denoising of stimulated Raman scattering microscopy images via deep learning. Biomed Opt Express. 2019 Aug 1;10(8):3860.

213. Otsuka Y, Makara K, Satoh S, Hashimoto H, Ozeki Y. On-line visualization of multicolor chemical images with stimulated Raman scattering spectral microscopy. Analyst. 2015;140(9):2984–7.

214. Houhou R, Bocklitz T. Trends in artificial intelligence, machine learning, and chemometrics applied to chemical data. Analytical Science Advances. 2021 Apr 2;2(3–4):128–41.

Appendix

A1. Fabrication and Chip Assembly

The steps involved in the fabrication and assembly of microfluidic devices are described below.

SU8 Photolithography on a Silicon Wafer

Standard UV lithography is employed to fabricate the microfluidic devices. The process involves the following steps:

1. *Cleaning the substrate*
   The silicon wafer is cleaned thoroughly to remove any contaminants or dust. This helps with the adhesion of the photoresist.
2. *Spin coating*
   A suitable resist is spin-coated onto the substrate at the required speed to obtain a uniform layer of the photoresist. About 3 ml–4 ml of the photoresist is spread onto the wafer and initially spun at 500 RPM to spread the resist layer evenly throughout the wafer. The speed is ramped up to 2,750 RPM for 30 seconds and then decelerated gradually.
3. *Soft baking*
   Undissolved solvents are removed by heating the substrate at 65°C. This also helps stabilise the resist layer. The wafer was prebaked on a hotplate for 1–2 minutes at 65°C and then transferred to a hotplate at 95°C for 5 minutes.
4. *Exposure*
   The photomask is aligned with the resist-coated substrate and exposed to UV light for a suitable duration. Some parts of the resist are cross-linked. The wafer was exposed after alignment (MJB4, Switzerland) at a constant intensity of 10 mW/cm^2 for 30 seconds.
5. *Post-exposure baking*
   To stabilise the crosslinked resist, and further enhance the contrast of the pattern, the exposed substrate is heated at 95°C for a suitable duration depending on the thickness of the resist layer.

6. *Development*
   Depending on the qualities of the resist, parts of the resist will be more soluble or less soluble. The wafer is washed gently multiple times with isopropanol, and the developer mr-Dev 600 (micro resist technology, Germany) is used to develop the wafer post-exposure.
7. *Hard bake*
   A final hard baking is performed at 200°C to cure the substrate. This improves the durability of the master for subsequent processing.

For my experiments, I used SU8 2100 photoresist and spin-coated it onto a 3-inch silicon wafer. To achieve a channel thickness of 125 μm, which is similar to the cladding diameter of the optical fiber, the resist was spin-coated at approximately 2,700 RPM.

Soft Lithography

1. PDMS (Sylgard 184 Silicone elastomer kit, Dow Corning, USA) was thoroughly mixed with the cross-linking agent to a ratio of 10:1.
2. The mixture is degassed in a vacuum desiccator for 15–30 minutes.
3. The PDMS mixture is then poured onto the patterned silicon wafer and baked for 4 hours at 75°C.
4. After curing, the inlets are punched with the help of a biopsy puncher (1 mm diameter).
5. The PDMS is cleaned thoroughly with scotch tape (3M) before plasma treatment.
6. A suitable glass slide (Brain Research Lab, 48 x 60 mm, no.1 thickness) is cleaned and placed inside the plasma cleaner (Harrick plasma, PDC-002-CE) along with the punched PDMS mould.
7. These are plasma treated in an O_2 atmosphere for 45–60 seconds.
8. The glass is then bonded to PDMS mould irreversibly.

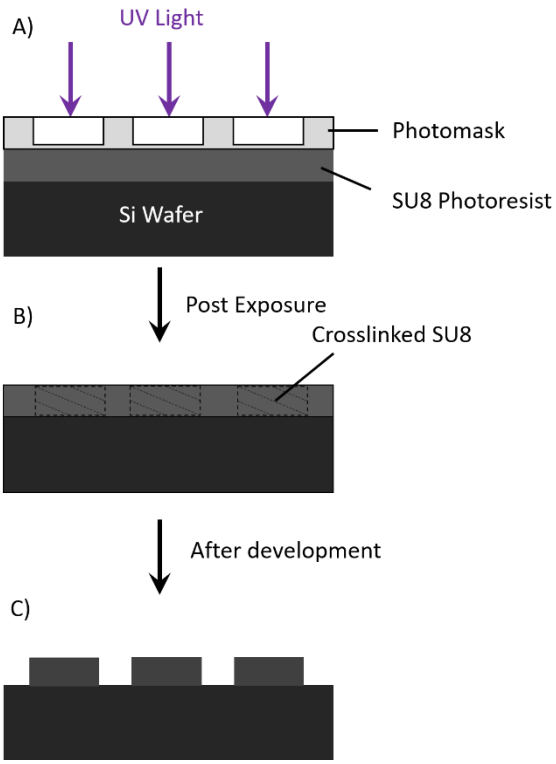

Figure A1.1: Shows the steps involved in UV lithography using SU8 photoresist.

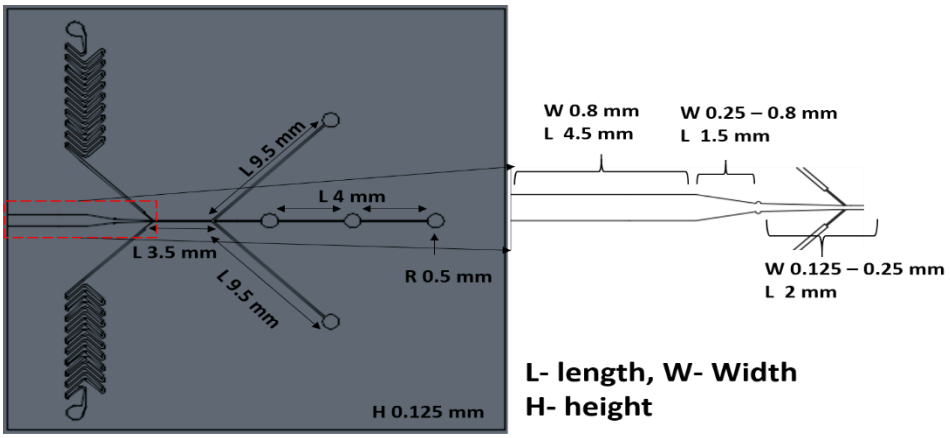

Figure A1.2: The dimensions and AutoCAD drawing of the chip are shown along with the dimensions of the waveguide for fiber integration.

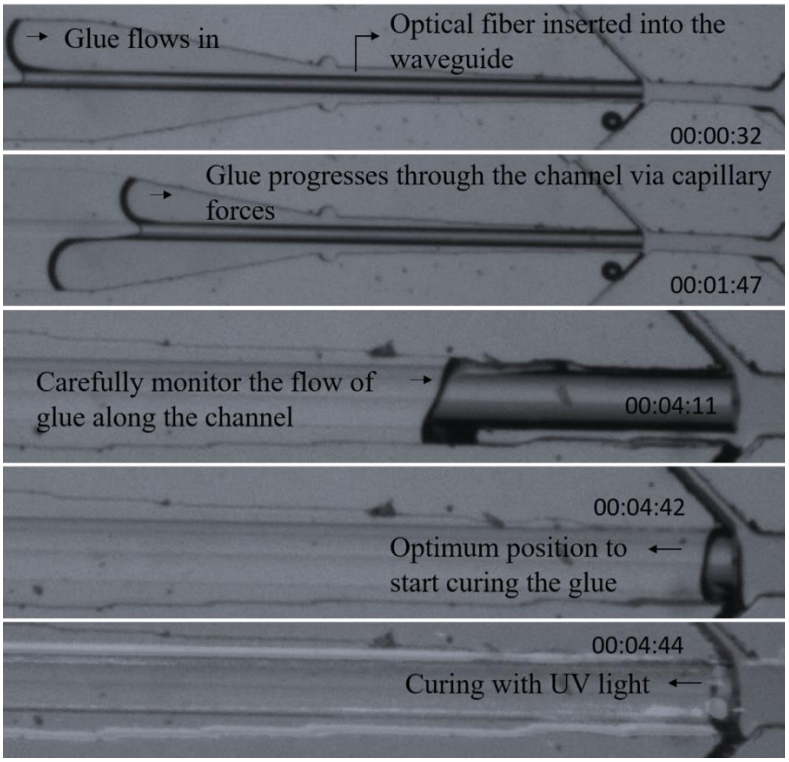

Figure A1.3: The process of glueing the fiber into the waveguide in the microchannel. Reproduced from (108) with permission from the Royal Society of Chemistry.

Integration of the Optical Fiber with the Microfluidic Device

The insertion of the fiber itself imposes no stringent requirements. Since the fiber is cylindrical and is inserted into a square channel, this results in gaps and results in leakage. This is solved by glueing and filling out the fiber-guiding channel with an optical adhesive. Before the glueing process begins, it is essential to ensure that the fiber is placed on a flat surface at the same level as the microfluidic chip and remains level during the insertion process. Additionally, precautions must be taken to prevent the adhesive from entering the main channel, as this could obstruct the chip and render it unusable. However, this issue can be easily mitigated by choosing a UV adhesive with an appropriate viscosity. I opted for a highly viscous glue (2,200 cP), which allows for a gradual filling of the fiber-guide channel over a few minutes. This enables the precise cessation of glue flow at a specific position without the need for exceptionally precise timing. Conversely, a UV adhesive

with a viscosity of around 500 cP would expedite the filling process, taking approximately 10–20 seconds and thereby streamlining the fabrication procedure.

Glass Capillary Device Fabrication

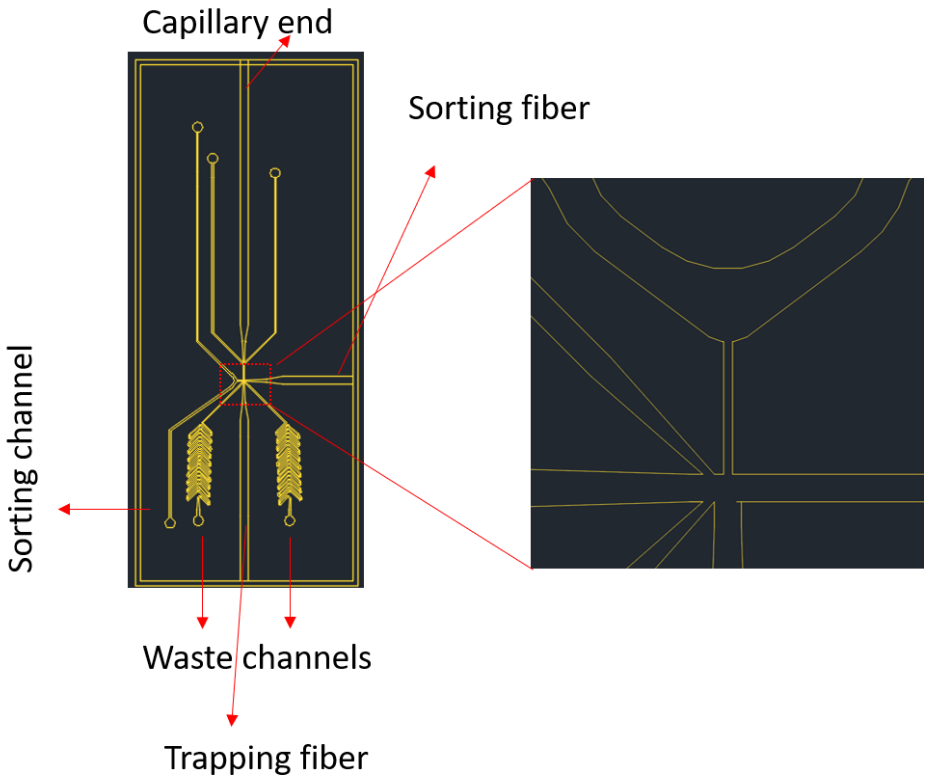

Figure A1.4: CAD design of a hybrid device integrating glass capillary with PDMS to improve delivery of the cells.

To further reduce the form factor of the OHT platform and improve operational stability, the device can be modified to incorporate a glass capillary for the delivery of cells. This eliminates the use of additional syringe pumps and further minimises fluctuations due to flow. A suitable glass capillary, with an inner diameter of 40 µm and an outer diameter of 130 µm (Postnova, UK), was chosen due to its size compatibility with the optical fiber (diameter 125 µm). The capillary was cleaved and carefully inserted through an open end of the channel from the side as shown in Figure A1.5.

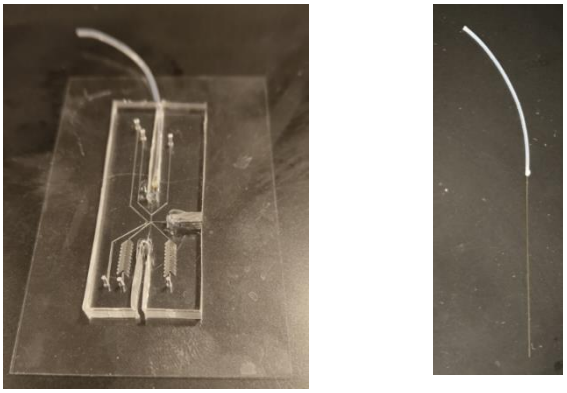

Figure A1.5: Shows the final device with the glass capillary inserted and fixed. On the right, the glass capillary (inner diameter: 40 μm) is glued to the tubing.

A2. Optical Setup

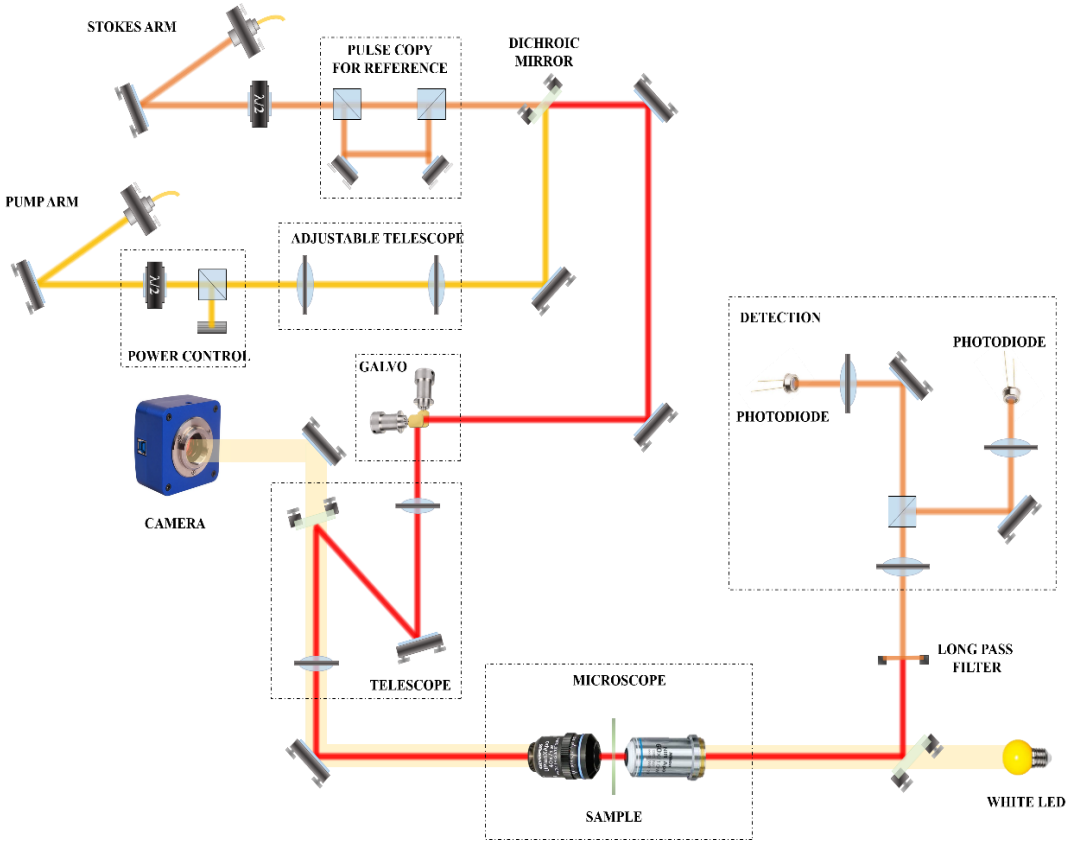

Figure A2.1: Stimulated Raman microscope optical scheme as developed by Zinkiewicz et al., as part of the TeamNET project.

The optical setup, with its various elements utilised for the Raman imaging of leukaemic cells, is shown in Figure A2.1. The setup was built as part of a consortium project within the TeamNET programme (POIR.04.04.00-00-16ED/18-00).

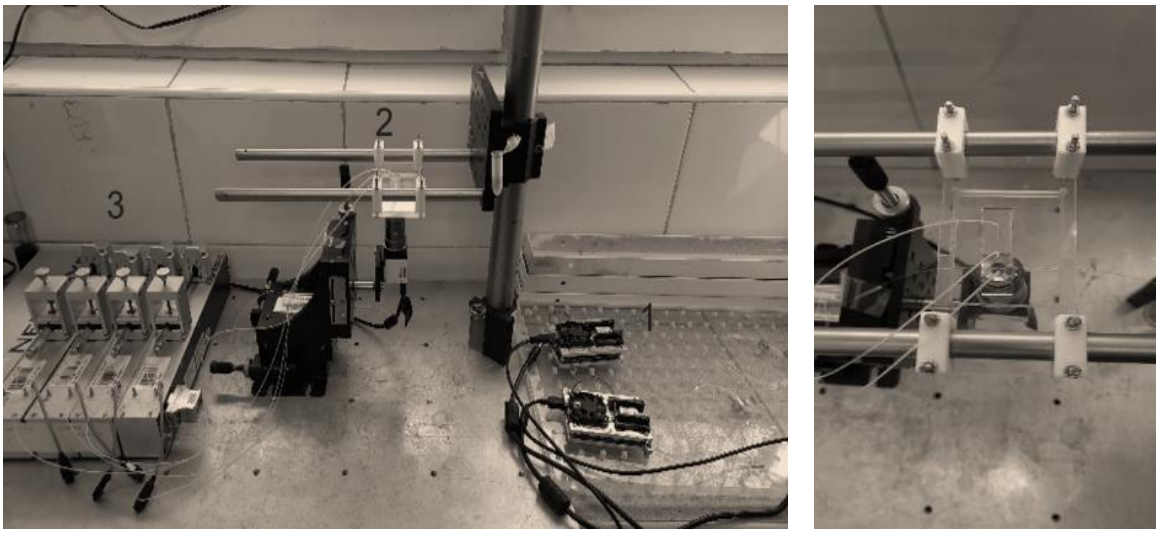

Figure A2.2: Components of the setup for the tweezing experiments 1. Fiberized laser diodes 2. Chip assembly (also shown on the right). 3. Cetoni syringe pumps for flow actuation.

The various components of the OHT platform are shown in Figure A2.2. The fiberized laser diodes (marked 1 in Figure A2.2) are integrated into the microfluidic chip (marked 2 in Figure A2.2) via dedicated guiding structures fabricated using photolithography. The syringe pumps (marked 3 in Figure A2.2) drive the fluid through tubing attached to the microfluidic chip.

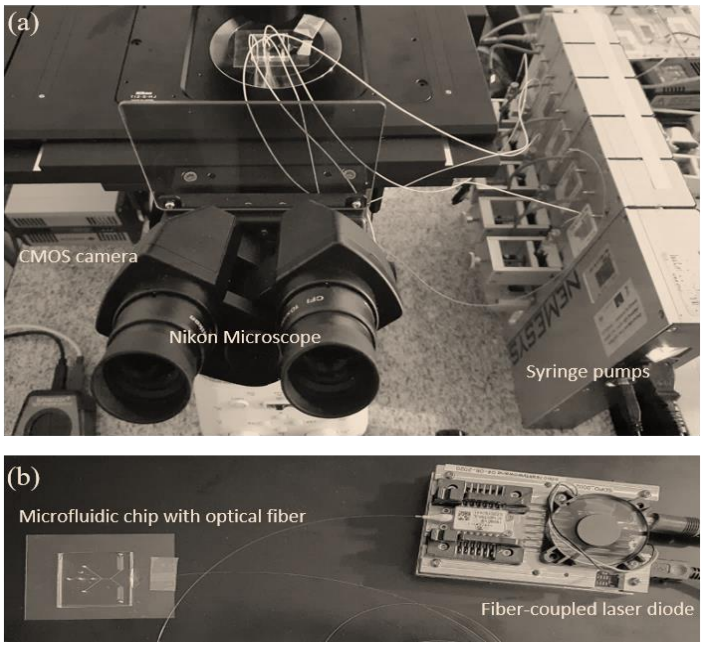

Figure A2.3: (a) Components of the OHT platform integrated with a microscope for single-cell analysis. (b) Photograph showing the optical fiber from the laser diode integrated with the microfluidic chip.

A3. Numerical Analysis

The analysis of the data and videos obtained through the experiments was conducted with the help of MATLAB. The positions of the particles and cells flowing at high speeds were extracted via custom-written codes. The code performed a frame-by-frame analysis of the large video files to accurately track the position of the particles and cells. This information was useful to plot velocity curves, compare theoretically estimated forces with experimentally obtained values, and quantify parameters necessary to characterise the OHT system.

MATLAB

1. *Calculation of scattering and gradient forces on PS particles:*

```
% Define parameters

n = 1.333; % Refractive index of the medium

alpha = 1; % Dimensionless scattering coefficient

P = 55e-3; % Incident optical power on the particle (in watts)

r = 7.5e-6; % Radius of the particle (in meters)

lambda = 980e-9; % Wavelength of the laser light (in meters)

x = linspace(-10e-6, 10e-6, 100); % Range of x-values (in meters)

w = (0.61*lambda)/ 0.12; %beam waist radius (in meters)

% Calculate the optical scattering force

Fs = [(8 * pi / 3) * n.^3 * alpha * P / (lambda^2) * (1 + (x / r).^2)];

% Calculate the optical gradient force

Fg = [(2 * pi * n.^2 * r.^3 * P) / (lambda * w.^2) * (x / (x.^2 + r.^2).^1.5)];

% Calculate the total optical force
```

```
Ftotal = Fs + Fg;
% Plot the forces
plot(x, Fs, 'r');
hold on;
plot(x, Fg, 'g');
plot(x, Ftotal, 'b');
    xlabel('x (meters)');
    ylabel('Force (Newtons)');
    legend('Scattering Force', 'Gradient Force', 'Total Force');
title('Optical Forces on a Particle');
```

2. Estimating centroid positions of particles and cells from video sequence:

```
clc;
clear all;
filename='Supplementary Trapping efficiency_OHT.mp4';
v = VideoReader(filename);
vidWidth = v.Width;
vidHeight = v.Height;
s = struct('cdata',zeros(vidHeight,vidWidth,3,'uint8'),...
   'colormap',[]);
%
v.CurrentTime= 1.0;    %specify start of the time
```

```
endtime= 2.0;          %specify end of time
k = 1;
while v.CurrentTime <= endtime
    s(k).cdata = readFrame(v);
    k = k+1;
end
% for k=20:1:40
%     s(k).cdata = readFrame(v);
% end
% roi_x_start= 820;
% roi_x_end= 930;
%
% roi_y_start= 220;
% roi_y_end= 280;
 numoffframes= length(s);
for k=numoffframes:-1:1
   thisFrame = s(k).cdata;
%thisFrame = s(k).cdata-s(2).cdata;
int_img=im2double(thisFrame);
% h=int_img(roi_x_start:roi_x_end,roi_y_start:roi_y_end,1:3);
%   inten(k)=sum(sum(h));
```

```
thisfig = figure();
thisax = axes('Parent', thisfig);
% image(h, 'Parent', thisax);
image(thisFrame, 'Parent', thisax);
set(gca,'fontsize',16)
title(thisax, sprintf('Frame #%d', k));
% colormap('gray');
end
%
% for u=2:1:15
%    thisFrame = s(u).cdata;
% thisfig = figure();
% thisax = axes('Parent', thisfig);
% image(thisFrame, 'Parent', thisax);
% set(gca,'fontsize',16)
% title(thisax, sprintf('Frame #%d',u));
% % colormap('gray');
% end
% Calc frames as time in seconds
% for i= 1:1:7
% time (i)= (Frame(i)- Frame(1))* 0.030
```

```
% end;
% Calc. position into distance in microns
% for j= 1:1:7
%     dist (j)= (PosY(j)- PosY(1))*0.33
% end
% thisFrame = s(61).cdata-s(5).cdata;
% thisfig = figure();
% thisax = axes('Parent', thisfig);
% image(thisFrame, 'Parent', thisax);
% set(gca,'fontsize',16)
% title(thisax, sprintf('Frame #%d', k));
% colormap('gray');
% set(gca,'Ydir','reverse'); (reverse axis order)
%
% NumberOfFrames=4;
% for frame = 1 : NumberOfFrames  %fill in the appropriate number
%   %this_frame = read(obj, k);
%   thisFrame = mov(frame).cdata;
%   thisfig = figure();
%   thisax = axes('Parent', thisfig);
%   image(thisframe, 'Parent', thisax);
```

```
%   title(thisax, sprintf('Frame #%d', k));

% end
```

COMSOL

This part of the study was carried out with assistance from Dr Konrad Giżyński. The idea was to model flow parameters based on the geometrical requirements and flow velocities required. The calculations provided insight into the flow rates necessary to regulate and focus single cells via 3D hydrodynamic focusing.

2D model parameter for the simulations

1. *Viscosity:*

   Water: 0.89 mPas at 25°C; density: 997.8 kg/m^3

   Media: 1.46 ± 0.15 mPas at 25°C; density: 997.8 kg/m^3

   Density of cells: 1.08 g/mL (1,080 kg/m^3)

2. *Flow rates:*

   Sample flow rates: 2µL/hr

   Side flow: 25µL/hr

   Top/bottom flow: 10µL/hr

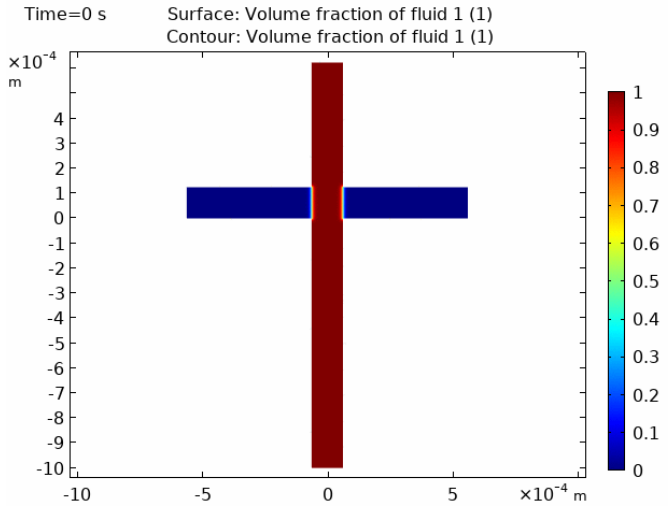

Figure A3.1: COMSOL simulation of the volume fraction within the microchannel with time, based on the 2D Model.

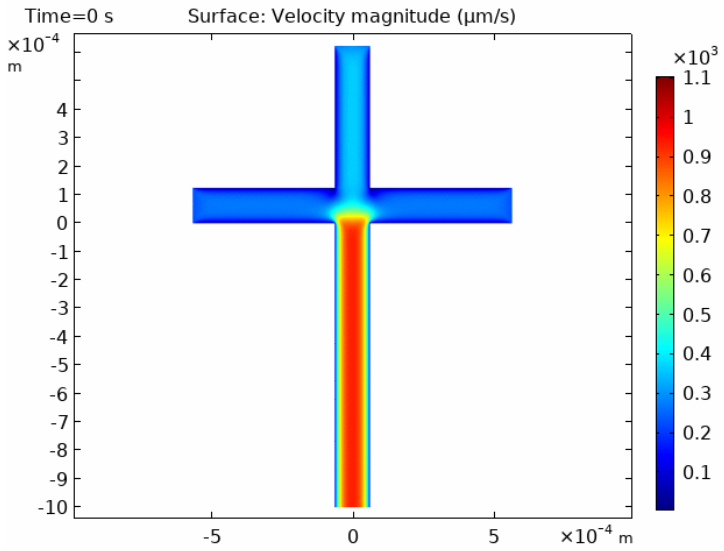

Figure A3.2: Simulation of the surface velocity parameters due to flow based on the parameters of the 2D model.

3D Model and New Mesh

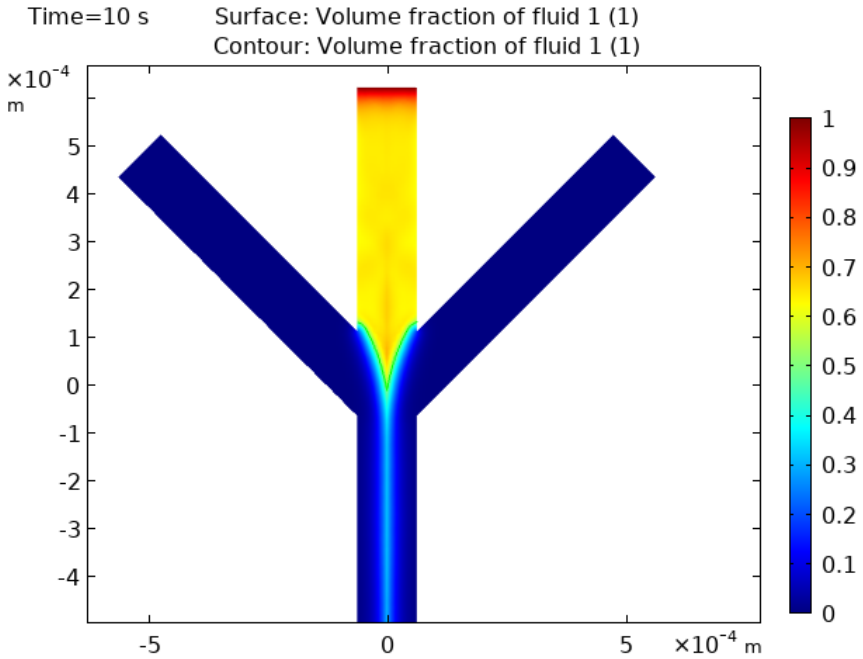

Figure A3.3: The competence of the sample fluid versus sheath fluid for various flow rates simulated via COMSOL.

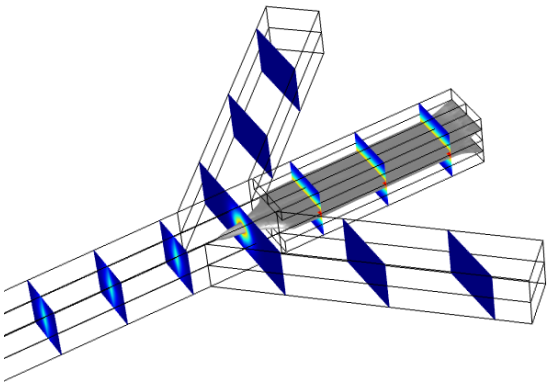

Figure A3.4: Updated 3D mesh model using which the flow rate ratios for the sheath and sample fluid were determined.

A4. Data Analysis

Velocity Curves

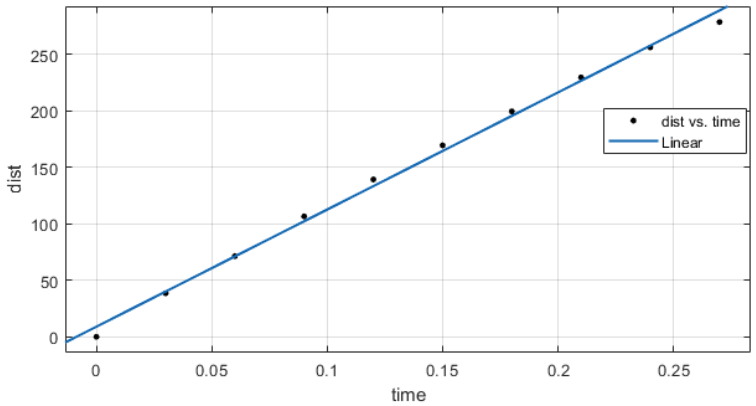

Figure A4.1: Distance versus time curve of a single PS bead flowing in the microchannel to determine flow velocities in the channel.

The velocity of particles after focusing was determined by measuring the centroid position of the particle with time as it flows through the microchannel. In the figures below, you will see that the velocity was determined by accurately tracing the position of the particle via a custom-written MATLAB code. The positions were then plotted against time and the slope was calculated. A linear model was used to determine the confidence of the experimentally determined positions represented by black dots on the curve and the derivative velocity values were extracted based on best fit.

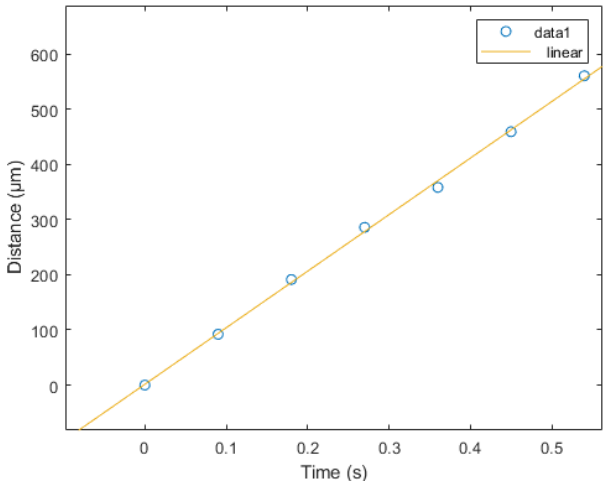

Figure A4.2: Distance versus time graph for various centroid positions of the bead flowing in the microchannel. The slope determines the average velocity of the bead for the given flow rates.

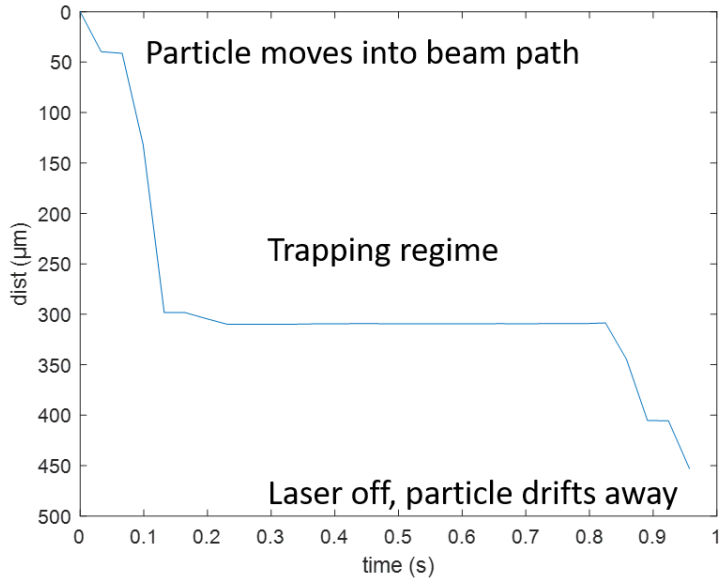

Figure A4.3: Centroid positions of the bead as it moves into the beam path, is trapped for some time, and is released.

A5. Optical Fiber Parameters

PS-PM980

The geometrical and mechanical specifications of the single-mode fiber used in this thesis as described by the manufacturer.

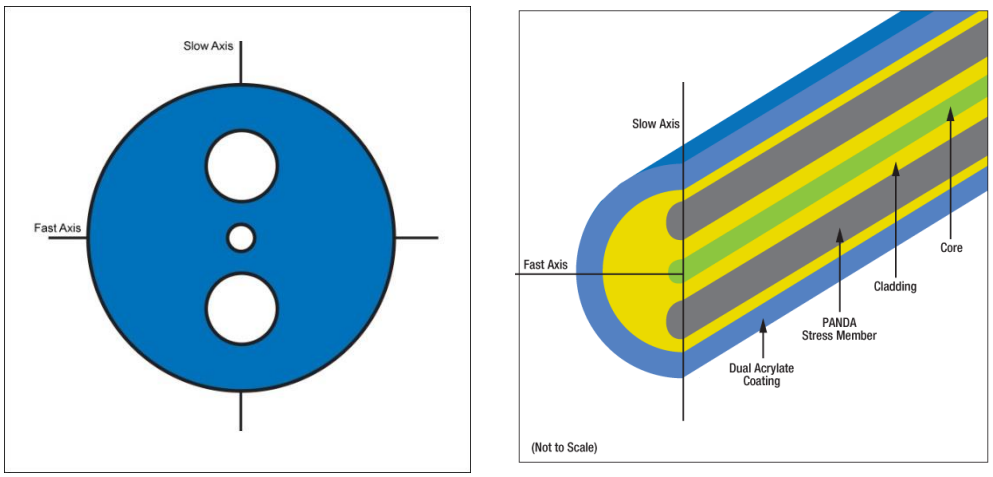

Figure A5.1: Geometrical and mechanical clad diameter: 125±1.0 μm; coating diameter: 245±15 μm; core diameter: 6.0 μm; core-clad concentricity: as obtained from Thorlabs.

Table 3. Description of the Thorlabs' photosensitive 980 nm PM maintain fiber from the manufacturer.

Geometrical & Mechanical	
Clad Diameter	125 ± 1.0 μm
Coating Diameter	245 ± 15 μm
Core Diameter	6.0 μm
Core-Clad Concentricity	<0.5 μm
Coating/Clad Offset	≤5 μm
Coating Material	UV Cured, Dual Acrylate
Operating Temperature	-40 to 85 °C
Proof Test Level	≥100 kpsi (0.7 GN/m^2)

Optical	
Attenuation	≤3.0 dB/km @ 980 nm
Numerical Aperture	0.12
Operating Wavelength (nominal)	970 nm - 1550 nm
Cut-off Wavelength	900 ± 70 nm
Mode Field Diameter	6.6 ± 1.0 μm @ 980 nm
Beat Length	≤3.5 mm @ 980 nm
Normalized Cross Talk	≤-40 dB @ 4 meters
Normalized Cross Talk (nominal)	≤-25 dB @ 100 meters